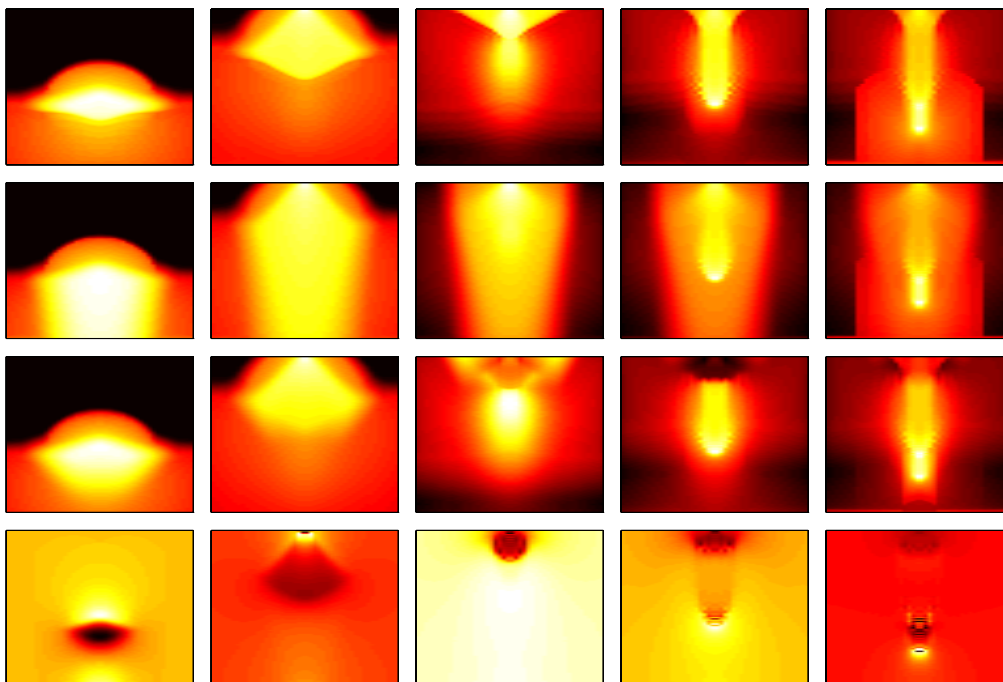


## Dielectric Breakdown in Insulating Gases

### Space Charge Effects and Non-Uniform Fields



Enrique Humberto Radames Gaxiola

Stellingen

behorende bij het proefschrift

**Dielectric Breakdown in Insulating Gases**

**Space Charge Effects and Non-Uniform Fields**

door

Enrique Humberto Radames Gaxiola

Eindhoven, 15 maart 1999

1. De vaak waargenomen afname van de lawinegroei in een gasontlading is het gevolg van het ruimteladingsveld. Ter plaatse van de hoogste ladingsdichtheid vermindert de ionisatiegroei aanzienlijk.  
*Wagner, K.H., Zeitschrift für Physik, Vol.204, pp.177-197, 1967*  
*Dit proefschrift, hoofdstuk 4*
2. Zodra zich in een gasontlading een anode gerichte "streamer" gevormd heeft wordt de stroomtoename sterker dan exponentieel.  
*Dit proefschrift, hoofdstuk 4*
3. De modificatie van het elektrische veld ten gevolge van een "spacer" is bepalend voor het ontladingsgedrag en heeft grote invloed op de doorslagspanning en de tijd tot doorslag.  
*Dit proefschrift, hoofdstuk 4*
4. Het "strippen" van een complex computermodel, zoals het twee-dimensionale hydrodynamische model beschreven in dit proefschrift, komt een brede toepasbaarheid ten goede.  
*Dit proefschrift, hoofdstuk 6*
5. Combinatie van experimenten en modellering vormt een krachtiger instrument dan indien men slechts over één van beide beschikt.  
*Dit proefschrift, hoofdstuk 7*
6. Pas bij het dimensioneren van een sensor ontstaat een goed begrip voor de beperkingen en grenzen van het werkgebied van die sensor.  
*H.F.A. Verhaart, Ph.D. thesis, Eindhoven University of Technology, 1982*  
*Dit proefschrift, hoofdstuk 3*
7. De in Nederland wenselijk geachte omvang van tweede en derde geldstroom onderzoek ondermijnt het onafhankelijk wetenschappelijke onderzoek.
8. De werkring van haar alumni kenmerkt de kwaliteit van een universitaire studie.
9. Hoge propaedeuse rendementen zijn in strijd met de selecterende functie van de propaedeuse.
10. Studeren is investeren in een in meerdere opzichten verrijkte toekomst. Bijbeunende studenten verwaarlozen hun kansen om het maximale uit hun studie te halen.
11. Nederland heeft een slecht maatschappelijk klimaat voor promovendi. Promoveren in Nederland is verworden tot iets als werken in een Turks-naai-atelier: zolang men produceert wordt men gedoogd.
12. Surfen is niet alleen een sport maar met name een lifestyle.

# **Dielectric Breakdown in Insulating Gases**

## **Space Charge Effects and Non-Uniform Fields**

Front cover:

Prebreakdown along a solid insulator in air and space charge modified electrical field in a streamer initiated breakdown.

Back cover:

- 1) Discharge measurement setup in the shielded high voltage lab of Eindhoven University of Technology
- 2) control and EMC measuring cabinet
- 3) discharge vessel

(photos by Eindhoven University Press).

1	
2	3

# **Dielectric Breakdown in Insulating Gases**

## **Space Charge Effects and Non-Uniform Fields**

### PROEFSCHRIFT

ter verkrijging van de graad van doctor aan de Technische  
Universiteit Eindhoven, op gezag van de Rector  
Magnificus, prof.dr. M. Rem, voor een commissie  
aangewezen door het College voor Promoties in het openbaar  
te verdedigen op maandag 15 maart 1999 om 16.00 uur

door

Enrique Humberto Radames Gaxiola

geboren te Villa Obregón (Mexico)

Dit proefschrift is goedgekeurd  
door de promotoren:

prof.dr.ir. P.C.T. van der Laan

en

prof.dr. F.J. de Hoog

Copromotor:

dr.ir. J.M. Wetzer

CIP-DATA LIBRARY TECHNISCHE UNIVERSITEIT EINDHOVEN

Gaxiola, Enrique H.R.

Dielectric breakdown in insulating gases : space charge effects and non-uniform fields / by  
Enrique H.R. Gaxiola. - Eindhoven : Technische Universiteit Eindhoven, 1999

Proefschrift. - ISBN 90-386-1550-7

NUGI 832

Trefwoorden: elektrische isolatiematerialen; doorslag / hoogspanningstechniek /  
elektrische gasontladingen / elektrische gasisolatie.

Subject headings: electric breakdown / gaseous insulation / electron avalanches /  
space charge / partial discharges.

Copyright ©1999 by E.H.R. Gaxiola, Department of Electrical Engineering, Eindhoven  
University of Technology, Eindhoven, The Netherlands.

voor mijn moeder Margriet en broer Ben



## Summary

This work deals with dielectric breakdown in insulating gases, under uniform and non-uniform fields and in the presence of space charge effects. Avalanche and streamer formation in insulating gases are studied, in particular in nitrogen ( $N_2$ ), dry air and sulfurhexafluoride ( $SF_6$ ). The goal of this work is to develop and verify discharge models for practical insulating geometries on the basis of physical discharge processes.

The modelling of dielectric breakdown, the physics behind it, the mathematical description and the numerical techniques, as well as the translation of physical phenomena into measurable quantities are discussed. Results of two-dimensional 2-D model simulations will be presented for electrical discharges in nitrogen and dry air. In addition the limitations of the methods used are indicated.

Design aspects of prebreakdown measurements are discussed and the resulting experimental setup with the measurement procedures used is presented. The work involves an experimental study of the electrical and optical discharge activity as well as 2-D model simulations. Time-resolved optical and electrical measurements are presented; a high bandwidth experimental setup is used to measure the discharge current and the optical discharge activity. These measurements, combined with the above mentioned 2-D model simulations are used to obtain a better insight in the relevant mechanisms and processes. This approach leads to a better understanding of the processes fundamental to gas-breakdown. Results will be presented for a uniform applied field without and with space charge field distortion, for a non-uniform applied field and for geometries with an insulating spacer.

Experiments on avalanches in a "simple" non-attaching inert gas ( $N_2$ ), together with the modelling results, are shown, followed by avalanche experiments and simulations for electronegative gases (dry air and  $SF_6$ ). The avalanche-to-streamer transition and the initiation of dielectric breakdown in  $N_2$ , dry air and  $SF_6$  are presented. It is shown what processes are responsible for the formation of a streamer. The trends of externally measured quantities correspond with those predicted by our model. Simulated particle density distributions give insight in the streamer formation phases leading to breakdown. From this the relevant processes and parameters can be determined, and thereby the complex physical 2-D hydrodynamic model developed initially, is stripped to a "simplified" model only incorporating the dominant processes and species. The time-to-breakdown  $t_{bd}$  and the electron transit time  $T_e$  in a uniform field are evaluated as a function of the applied (Laplacian) field, the initial electron number, the pressure and the pressure reduced field  $E/p$ . The time-to-breakdown curves simulated are compared to, and agree with experimental observations.

An experimental study of prebreakdown phenomena in dry air along insulator surfaces is presented.

The results of the work done on prebreakdown phenomena in gases has also been applied to partial discharges (PD) in voids in solid insulating materials. A time-dependent model of partial discharges in voids and a time-resolved study of the physical processes governing void discharges are presented. The influence of dielectric material on partial discharges in voids and PD detection in insulators, are shown, together with scaling relations and practical implications. Results from partial discharge modelling and measurements on micrometer voids in solid dielectrics are presented. Void sizes down to  $10 \mu m$  were studied. The results do not suggest the existence of a smallest detectable void size. For micrometer voids the discharge phenomena change from a gas discharge-like avalanche-and-streamer breakdown towards a spark-like plasma.

The work is concluded with an analysis and discussion on the relevant parts of our 2-D hydrodynamic model for different gases and various situations. Through parameter variation techniques conclusions can be reached on which mechanisms can be excluded under specific conditions.

Both space charge and field non-uniformities significantly influence the development of an initial avalanche into a final dielectric breakdown.

The present work, based on a combination of time-resolved electrical and optical measurements, and simulation studies with a 2-D hydrodynamic model, has yielded a physical description of the responsible mechanisms and development stages for:

- \*  $N_2$ , dry air and  $SF_6$
- \* uniform and non-uniform fields
- \* gaps bridged by insulators
- \* voids in solid dielectrics.

## Samenvatting

Dit werk betreft de studie van diëlektrische doorslag in isolerende gassen, in homogene en inhomogene elektrische velden en in de aanwezigheid van ruimteladingseffecten. Lawines en "streamers" in elektrisch isolerende gassen zijn het onderwerp van studie; meer in het bijzonder in stikstof, droge lucht en sulfurhexafluoride. Het doel van dit werk is het ontwikkelen van ontladingsmodellen voor in de praktijk voorkomende isolatiegeometrieën op basis van een fysische beschrijving van doorslagprocessen.

De modellering van diëlektrische doorslag, de fysica erachter, de mathematische beschrijving en de numerieke technieken, alsook de vertaling van fysische fenomenen in meetbare grootheden worden toegelicht. Hierbij worden ook de beperkingen van de gebruikte methoden gepresenteerd.

Ontwerpaspecten van voordoorslagmetingen en de daaruit gerealiseerde experimentele opstelling met meetprocedures worden beschreven. Tijdopgeloste optische en elektrische metingen alsook twee-dimensionale (2-D) modelcomputersimulaties worden gepresenteerd. Resultaten van 2-D computer simulaties van elektrische ontladingen in stikstof en in droge lucht worden besproken. Het gepresenteerde model wordt gebruikt voor het verkrijgen van meer inzicht in processen die voorafgaan aan de doorslag, door vergelijking van gemeten en gesimuleerde data. Resultaten voor doorslag in homogene velden met en zonder ruimteladingseffecten, doorslag in inhomogene velden en voor doorslag langs vastestof isolatoren worden gepresenteerd.

Lawine-experimenten in een niet-elektronennegatief gas ( $N_2$ ), tezamen met de model uitkomsten, worden gepresenteerd, gevolgd door experimenten en simulaties voor elektronennegatieve gassen (lucht en  $SF_6$ ).

De stadia van lawine-"streamer" overgang en de initiatie van diëlektrische doorslag in  $N_2$ , lucht en  $SF_6$  worden gepresenteerd. De processen verantwoordelijk voor "streamer" vorming worden besproken. De trends van meetbare externe grootheden corresponderen met de uitkomsten van ons model.

Deeltjesdichtheidsverdelingen geven meer inzicht in het gedrag voorafgaand aan de doorslag. Hieruit kunnen de relevante processen en parameters bepaald worden om daarmee het complexe hydrodynamische model te kunnen "strippen" en zo te komen tot vereenvoudigde modellen.

De tijd tot doorslag en de elektronen oversteektijd in een homogeen veld worden berekend als functie van het aangelegde elektrische veld, het aantal startelektronen, de druk en het gereduceerde veld  $E/p$ . De uit het model volgende gesimuleerde tijd-tot-doorslagkrommen zijn vergeleken met, en corresponderen met experimentele waarnemingen.

Een experimentele studie van het gedrag voorafgaand aan doorslag in droge lucht langs isolatoren van verschillende vorm wordt gepresenteerd.

Een toepassing van de gevonden inzichten van het werk aan voordoorslag processen in gassen is partiële ontladingen in holtes in vaste stof isolatiematerialen. Een tijdopgelost model voor partiële ontladingen in holtes en een tijdopgeloste studie van de fysische processen bij partiële ontladingen worden gepresenteerd. De invloed van het diëlektrische materiaal op de partiele ontladingen in holtes en de partiele ontladingsdetectie in isolatoren worden geïllustreerd; tezamen met schaalwetten en praktische implicaties. Resultaten van partiele ontladingsmetingen en modellering aan micrometer holtes in vaste stof diëlektrica worden gepresenteerd. Holtes met afmetingen tot  $10 \mu m$  zijn bestudeerd. De resultaten suggereren niet het bestaan van een minimaal detecteerbare holte afmeting. Voor micrometer holtes verandert het ontladingsgedrag van een gasontladingsachtige lawine en een "streamer" doorslag naar een "spark"-achtig plasma.

Tot slot wordt een analyse en discussie van de relevante delen van het hydrodynamische (vloeistof) model voor verschillende gassen en condities gepresenteerd. Door middel van parametervariaties is hierin meer inzicht verkregen.

Zowel ruimtelading en veldinhomogeniteiten beïnvloeden de ontwikkeling van de primaire lawine tot een diëlektrische doorslaggedrag.

Het werk in deze dissertatie, gebaseerd op een combinatie van tijdopgeloste elektrische en optische metingen, en simulatie studies met een 2-D hydrodynamisch model, hebben geleid tot een fysische beschrijving van de verantwoordelijke mechanismen en ontwikkelingsfasen voor:

- \*  $N_2$ , droge lucht en  $SF_6$
- \* homogene en inhomogene velden
- \* doorslag langs isolatoren in droge lucht
- \* holtes in vaste stof diëlektrica.

## CONTENTS

<b>Chapter 1</b>	<b>Introduction</b>	<b>1</b>
	1.1 General introduction	1
	1.2 Avalanches and streamers	3
	1.3 Partial discharges in voids	4
	1.4 Outline of thesis	4
<b>Chapter 2</b>	<b>Modelling of Prebreakdown Phenomena</b>	<b>5</b>
	2.1 Introduction	5
	2.2 Fundamental processes in the electrical breakdown of gases	5
	2.3 Two-dimensional model	10
	2.3.1 Considered species and processes	
	2.3.2 Mathematical model	
	2.3.3 Numerical model and implementation	
<b>Chapter 3</b>	<b>Experiments</b>	<b>17</b>
	3.1 Coupling between the charge movement in the gas and the current in the external circuit	17
	3.2 Design aspects of diagnostics for prebreakdown measurements	19
	3.3 Experimental setup	23
	3.3.1 Discharge initiation	
	3.3.2 Discharge vessel	
	3.3.3 Optical diagnostics	
	3.3.4 Measuring electrode geometry	
	3.3.5 Spacer geometries	
	3.4 Measurement procedure	30
	3.5 Partial discharges	31
<b>Chapter 4</b>	<b>Experimental and Modelling Results</b>	<b>33</b>
	4.1 Introduction	33
	4.2 Avalanches in uniform applied fields	36
	4.2.1 Avalanches in nitrogen	
	4.2.2 Avalanches in dry air	
	4.2.3 Avalanches in $SF_6$	
	4.3 Streamers and transition to breakdown	51
	4.3.1 Streamers in nitrogen in uniform applied fields	
	4.3.2 Streamers in dry air in uniform applied fields	

	4.3.2.1	Prebreakdown phenomena	
	4.3.3.2	Time-to-breakdown	
	4.3.3	Streamers in $SF_6$ in uniform and non-uniform fields	
4.4		Prebreakdown phenomena along insulator surfaces in dry air	85
<b>Chapter 5</b>		<b>Application to Partial Discharges in Voids</b>	<b>97</b>
	5.1	A time-dependent model of partial discharges in voids <sup>1</sup>	98
	5.2	A time-resolved study of the physical processes governing void discharges <sup>2</sup>	106
	5.3	The influence of dielectric material on partial discharges in voids <sup>3</sup>	112
	5.4	Partial discharge detection in insulators; scaling relationships and practical implications <sup>4</sup>	116
	5.5	Partial discharges in micrometer voids in PTFE <sup>5</sup>	120
	5.6	Partial discharge modelling and measurements on micrometer voids in solid dielectrics <sup>8</sup>	124
	5.7	Other applications	128
<b>Chapter 6</b>		<b>Evaluation of the Model</b>	<b>129</b>
	6.1	Introduction	129
	6.2	Limitations of numerical techniques for describing prebreakdown	129
	6.3	Different discharge regimes	132
	6.4	Parameter variations to identify relevant mechanisms	137
	6.4.1	Nitrogen	
	6.4.2	Dry air	
	6.5	Discussion on other modelling aspects	142
<b>Chapter 7</b>		<b>Conclusions</b>	<b>147</b>
<b>A</b>		<b>Data used in the 2-D model simulations</b>	<b>151</b>
		Bibliography	155
		List of symbols	165
		<i>Acknowledgement</i>	167
		<i>Curriculum Vitae</i>	169





## Chapter 1

### Introduction

*In this thesis avalanches, streamers and partial discharges are treated, including non-uniform field electrode geometries and insulating spacers.*

#### 1.1 General Introduction

In electrical power systems the insulation is a decisive element for the voltage withstand capability and for the (small) probability of power failures. On the path from generation of electricity to its use by costumers many components in between take care of the transmission and distribution of the electrical energy. All of these have insulation design aspects. System voltages and currents, as well as overvoltages and short-circuit currents expected, are important parameters in designing power system networks. These also influence what possible insulation to use. For example most transmission lines all across the world are overhead lines, whereas for the distribution level many urban areas can be served by cable networks for distribution of electrical energy. In other regions cost aspects still make it more economical to use overhead lines, in many places even at lower distribution voltages. Voltages are transformed up or down in substations, mostly near the generating plants or near the industrial or household consumer centers. These substations are either "open" (the insulation is formed by the surrounding air), or "closed" (the insulation is formed by a compressed insulating gas). This gas needs to have superior electrical insulating properties, along with other properties, like being not too expensive, environmentally harmless and non-flammable. All these aspects together are important for the design of the system.

The insulation is effective up to the breakdown threshold. Basically, the breakdown process involves three stages: 1) primary electron generation to initiate the process, 2) exponential growth of the number of charge carriers, and 3) secondary electron generation to sustain the discharge until breakdown.

In preventing dielectric breakdown in gases we look for ways of restricting or diverting the initial supply of electrons on which the breakdown mechanism relies. Inert gases can be considered as they have a high ionization threshold. More effective however, are gas molecules or atoms that "attach" electrons, creating negative ions. The negative ions are relatively large and immobile and do not directly contribute to the breakdown initiation. Molecules containing fluorine and chlorine are often strongly electronegative gas molecules. Most widely used is sulphurhexafluoride ( $SF_6$ ), because of its unmatched properties in the

whole range of applications; ranging from dielectric insulating capabilities to the use as circuit-breaker arc quenching gas. For some special applications or older installations also compressed air, nitrogen ( $N_2$ ) or gas-mixtures like  $SF_6 / CF_4$  are used. In the past decades much research has been focused on finding replacement gases and gas-mixtures. At present the understanding is that there is no real alternative to  $SF_6$ <sup>16</sup>. All strongly electronegative gases are also CFC ("greenhouse") gases and possible other gases by far do not meet the required electrical insulating or arc quenching gas properties. The dielectric breakdown under various conditions is being studied to enable a better understanding of the phenomena for various insulation systems under various conditions. The relevance lies in the implications to insulation system design and to discharge applications (e.g. barrier discharges to deNO<sub>x</sub> motor exhaust gases<sup>17</sup> and flue gas treatment and chemical reactors using electrical corona discharges<sup>18</sup>).

For the design of electrical gas insulated systems, experimental (empirical) data on breakdown fieldstrengths are extensively used. Breakdown voltages for gases are usually given by Paschen curves which serve as an engineering tool in high voltage engineering, in describing the breakdown voltage of gases as a function of the product of electrode gap distance and pressure. Paschen curves are reliable for uniform or weakly non-uniform situations. In many practical situations non-uniform fields require a more sophisticated approach (compact equipment, corona, void discharges, electrostatic discharges (ESD)).

In this work recent research on processes preceding breakdown will be described; the so-called prebreakdown phenomena. It is a continuation of earlier work by Kennedy<sup>19</sup>, Wen<sup>20</sup> and Verhaart<sup>21</sup>, and deals with a time-resolved optical and electrical study of the avalanche and streamer formation in atmospheric nitrogen and dry air. Where the investigations previously focused on uniform electrical fields without space charge effects in a "simple" gas like  $N_2$ , these days we are able to describe processes in complex gases and inhomogeneous (space charge) fields. Earlier models described the processes with analytical expressions and were verified by means of time-resolved discharge current measurements. From these experiments so called "swarm-parameters" were deduced, like the electron drift velocity  $v_e$  and the ionization coefficient  $\alpha$ <sup>20</sup>. The hereby collected data together with the already available data forms important input for advanced discharge models. In the past decades the upcoming of available computing power has also led to ever more advanced models being developed for the description of prebreakdown phenomena<sup>19,22-55</sup>.

In contrast to work presented earlier for  $N_2$  and dry air<sup>19</sup>, this work also includes time-resolved optical and electrical measurements of the avalanche prebreakdown phase and streamer formation phases leading to breakdown in atmospheric  $SF_6$ . In addition this study is also a continuation of earlier work by Verhaart<sup>21</sup> and deals with a study of avalanche and streamer formation along insulator surfaces in dry air.

The goal of this work is to develop and verify discharge models for practical insulating geometries on the basis of physical discharge processes. With the results from experiments

and two-dimensional (2-D) model simulations the formation of avalanches and streamers, and the dominant processes involved will be illustrated and discussed. Time-resolved optical and electrical measurements on the avalanche and streamer formation phases leading to breakdown will be presented. Through these diagnostics a better understanding of the processes fundamental to gas-breakdown can be obtained. The information obtained will be used to extend the existing hydrodynamic models for  $N_2$  and air<sup>19,22-34,37-50,53-55</sup> to  $SF_6$ .

The simulations in this work are based on a 2-D hydrodynamic model involving a 3-D electrical field calculation. At the electron energies occurring at our conditions it has been shown (for  $N_2$  and dry air) that such a model correctly describes the phenomena until the moment at which the cathode directed streamer (or the anode-directed streamer) reaches the cathode (anode), i.e. hundreds of picoseconds before actual breakdown occurs<sup>19</sup>, see further in Chapter 4. The calculations of prebreakdown phenomena in gases for homogeneous laplacian fields with superimposed space charge field necessitates a 2-D discharge model with a 3-D electrical field calculation routine.

For (strongly) inhomogeneous laplacian fields a completely 3-D model is necessary.

A sophisticated simulation program describes the physical discharge processes in the gap (without a spacer present). This model is used to obtain a better insight in the relevant mechanisms and processes by a comparison of measurements and simulation data. The basis of the 2-D hydrodynamic model (for  $N_2$  and dry air) will be briefly discussed.

A fast experimental setup is used to measure the discharge current and the optical discharge activity with and without a spacer present. An image intensified charge coupled device (ICCD) camera with a minimum shutter time of 5 ns is used. The avalanche to streamer formation phases for a pulsed laser-induced discharge are here described for different values of the direct current (dc) voltage. Results obtained for  $N_2$  and dry air will be discussed, from experiments and 2-D model simulations. Also results obtained for  $SF_6$ , from experiments in a uniform and non-uniform field will be discussed.

## 1.2 Avalanches and streamers

Several breakdown criteria for insulating gases have been reported<sup>56-58</sup>. Two well accepted breakdown criteria in gases are: the "Townsend breakdown mechanism"<sup>59</sup> and the "streamer breakdown mechanism"<sup>60-63</sup>. The first one is based on a sequence of avalanches and depends on "remote" electron generation processes at the cathode ("far" away from the growth region). The second criterion depends on an avalanche to streamer transition, due to instantaneous local electron generation giving rise to a critical avalanche that causes instability in the gap and induces gap-breakdown. In between there is a transition region in which we observe some of both mechanisms.

As a consequence, in this thesis we distinguish between avalanches and streamers and do

not focus on the herefore mentioned breakdown criteria.

The avalanche is the ionizing growth process in which each electron generates more than one subsequent ionizing electron thereby enabling exponential growth.

In case the space charge field created by the charged species is of the same order of magnitude as the applied external field, the space charge influences the local ionizing processes considerably. Usually this can also be recognized from the current growth which starts to deviate from exponential growth. We call this type of discharge a streamer discharge. An avalanche may grow directly into a streamer discharge, or it may initiate a sequence of avalanches finally leading to a streamer discharge.

### 1.3 Partial discharges in voids

An important application of discharge studies is the area of partial discharges (PD) in voids. Discharges in voids shorten the lifetime of solid insulation in power apparatus. In order to prevent discharge induced damage, the causes of discharge activity and the interaction with the solid dielectric need to be understood. A high bandwidth experimental setup ( $1.4\text{ GHz}$ ) has been developed, which enables measurement of the PD inception voltage, the PD current waveform and the charge involved in PD in artificial voids in solid insulating materials. The work on void discharges presented is a continuation of earlier work<sup>1,2</sup>. Results of experimental and theoretical investigations are presented for cylindrical and spherical voids of various dimensions in different dielectric materials. In particular microvoids (voids with characteristic dimensions below  $100\ \mu\text{m}$ ) in PTFE (teflon) and PC (polycarbonate) are studied.

### 1.4 Outline of thesis

The outline of this thesis is given below.

Chapter 2 gives a short description of the fundamental processes in the electrical breakdown of gases and the modelling of avalanches and streamer discharges.

Chapter 3 describes the design aspects of diagnostics for prebreakdown measurements and the measuring procedures used.

Chapter 4 covers the results of measurements and modelling for various gases under different conditions.

Chapter 5 shows the application of the insights gained by prebreakdown research on partial discharges in voids.

Chapter 6 describes a further evaluation of the relevant processes and further simplification of the hydrodynamic model into an "engineering model".

Chapter 7 presents and discusses the conclusions that can be drawn from the work described in this dissertation and gives recommendations for future work.

## Chapter 2

### Modelling of Prebreakdown Phenomena

*In this chapter the modelling of dielectric breakdown will be discussed: the physics behind it, the mathematical description and the numerical modelling techniques, the limitations of the methods used, and the translation into the electrically measurable quantities.*

#### 2.1 Introduction

To obtain a better understanding of the processes fundamental to dielectric gas-breakdown 1-D and 2-D models have been developed to describe the prebreakdown phenomena. These "tools" will be used to predict the externally measurable quantities and to obtain a better understanding of gas breakdown. Two basically different approaches are possible: a description by means of a Monte-Carlo simulation<sup>35,36,40</sup> or a description by means of a model based on continuity equations (hydrodynamic model)<sup>19,22-34,37-50,53-55</sup>. The last one loses its validity under non-equilibrium conditions, which may exist within a streamer head. At the electron energies occurring in our conditions it has been shown that a 2-D hydrodynamic model correctly describes the phenomena until the moment at which the cathode directed streamer (or the anode-directed streamer) reaches the cathode (anode), i.e. hundreds of picoseconds before actual breakdown occurs<sup>19</sup>. The description of prebreakdown phenomena in gases for homogeneous Laplacian fields (e.g. a parallel plate electrode geometry) with superimposed space charge field necessitates a 2-D discharge model with a 2-D electrical field calculation routine, since closed form analytical solutions only exist for the case without space charge effects<sup>20</sup>. Strongly inhomogeneous Laplacian fields (e.g. point to plane or wire to cylinder electrode geometries) require a full 3-D model. In some cases a 1-D or 2-D model in a non-cartesian coordinate system is used (e.g. in a concentric spheres geometry or in a wire cylinder geometry).

#### 2.2 Fundamental processes in the electrical breakdown of gases

A physical description of gas breakdown is given below. The various fundamental processes in the electrical breakdown of gases are summarized, and the reaction equations are given. For an extensive treatment of this subject see e.g. Meek and Craggs<sup>56</sup>.

Under the influence of an applied field electrons (released from a cathode, or from gas molecules, atoms or ions, by (photo)ionization or detachment) drift in the direction opposite to the applied field. They gain energy from the electrical field and on the other hand lose

energy by collisions with the gas molecules or atoms in the inter-electrode gap. In elastic collisions with the background gas molecules or atoms, electrons do not lose much of their kinetic energy but they are scattered yielding a randomized velocity distribution. Ionization and excitation result from inelastic collisions between electrons and the background gas molecules or atoms.

**Collisional ionization:**

If the kinetic energy gained by an accelerated electron is larger than the ionization energy threshold of the gas molecule or atom, collisional ionization may take place in which an electron and a positive ion are formed. The mean number of ionizing collisions per electron travelling a unit length in the direction of the field is termed "Townsend's first ionization coefficient"  $\alpha$ . Two types of collisional ionization processes are:

Direct ionization



Dissociative ionization



$X, Y, Z$ : gas molecules or atoms

$X^+$ : positive ion

$e^-$ : electron

**Gas phase photoionization:**

When a photon with sufficiently high energy collides with a gas molecule or atom it can ionize the gas molecule or atom, thereby creating an electron and positive ion.



$h\nu$ : photon energy

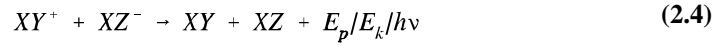
**Recombination:**

In general a positive ion and an electron or negative ion can form neutral atoms or molecules by recombination: \* in the gas, or \* at the electrode (recombination with image charges).

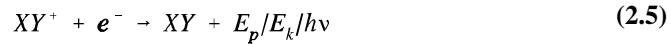
The second option is the most important mechanism in this work, because at the relatively low electron densities in electron avalanches ( $<10^{16} \text{ cm}^{-3}$ ) recombination in the gas can usually be neglected on the considered timescales.

When a positive ion strikes the cathode, or a negative ion strikes the anode, it is neutralized. The electrons leave the gap at the anode.

Ion-ion recombination



Electron-ion recombination



$X$ : negative ion  
 $E_p$ : potential energy of the gas molecules or atoms  
 $E_k$ : kinetic energy of the gas molecules or atoms

Excess energy may show up as photon energy  $h\nu$  or as potential  $E_p$  or kinetic energy  $E_k$ . The ion-ion recombination coefficient  $\epsilon_{pm}$  is defined as the net number of positive ion - negative ion recombinations per unit time per unit density of positive and negative ions. The electron-ion recombination coefficient  $\epsilon_{pe}$  is defined as the net number of electron - positive ion recombinations per unit time per unit density of electrons and positive ions.

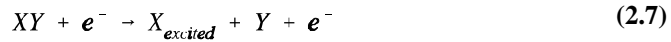
**Excitation:**

At lower energy levels interactions between electrons or photons and heavy particles (gas molecules and atoms) that can bring the heavy particles in excited states are more likely.

Electronic excitation



Dissociative excitation



Photoexcitation



By successive collision with an electron, a photon or another excited gas species the excited gas species gains energy leading to a higher level of electronic excitation or ionization.

If the excited state is unstable the particle falls back to a lower (ground) state. The decrease in energy occurs by "spontaneous relaxation" emitting a photon, or through "quenching" in which vibrational or electronic deactivation by collision with another gas molecule or atom transfers all or part of its energy to the other gas molecule or atom.

The quenching pressure  $p_q$ , which is inversely proportional with the deexcitation time constant for the excited species  $\tau_m$ , relates the relative importance of the relaxation types; spontaneous relaxation dominates below  $p_q$  and collisional relaxation dominates above  $p_q$ .

**Attachment:**

An electron can be attached to a neutral gas molecule or atom thereby forming a negative ion. The attachment coefficient  $\eta$  is defined as the mean number of negative ions produced by an electron travelling one centimeter in the direction of the field.

Direct attachment



Dissociative attachment



Three-body attachment (stabilization and charge transfer)

**Detachment:**

A stable negative ion drifts towards the anode where it is neutralized. An unstable negative ion can release the attached electron after a certain mean characteristic time  $\tau$ . The electron detachment frequency  $k_{ud}$  is defined as the mean number of detached electrons occurring per second per unstable negative ion.

Autodetachment



Photodetachment



Collisional detachment processes:

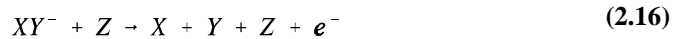
Direct detachment



Associative detachment



Dissociative detachment



**Charge exchange (conversion):**

Upon collision with a neutral gas molecule or atom an unstable negative ion may be transformed into a stable negative ion. This process is relevant for avalanche formation because it immobilizes electrons which may then no longer cause ionizing collisions. The conversion frequency  $k_c$  is defined as the mean number of negative ion conversions occurring per second per unstable negative ion.



**Secondary electron emission from surfaces:**

An electron can be released if the energy of an incident photon on the cathode is higher than the cathode material's workfunction. The secondary photoelectron yield  $\gamma_{\text{photon}}$  is the mean number of secondary electrons emitted from the cathode surface per ionizing collision. In general for incident energetic particles or photons we distinguish between three cases:

- \* Secondary photoelectron emission from surfaces.
- \* Secondary electron emission by positive ion impact from surfaces.
- \* Secondary electron emission by metastables from surfaces (not incorporated in the 2-D model).

**Drift:**

Under the influence of an applied field each electron experiences a net force  $-qE$  from the field. This force does not alter appreciably the random path of an individual electron; the effect when averaged over several mean free path lengths and over all electrons, however, is a net motion of the group in the direction opposite to the electrical field. Drift is defined as this net displacement of the population of particles. (The movement of the negative charged particle cloud in equilibrium conditions and of the positive charged particle cloud are in opposite direction.) The mobility  $\mu$  relates the drift velocity  $v_{\text{drift}}$  to the electrical field  $E$ , for the electrons respectively the ions.

**Diffusion:**

Diffusion is the statistical random motion of a specific type of particle which causes a net velocity from regions of high concentration to regions with a lower concentration. The diffusion coefficient  $D$  is defined as the net number of particles passing per unit time through a surface area unit perpendicular to a concentration gradient of magnitude one. In the presence of an electric field the electron and ion diffusion become anisotropic and a longitudinal diffusion coefficient  $D_L$  and a transverse diffusion coefficient  $D_T$  are distinguished, describing the diffusion in the direction parallel respectively perpendicular to the electric field. Under equilibrium conditions at atmospheric pressure the electron and ion distributions are nearly isotropic and  $D_L=D_T$ , so we then only need to consider one diffusion coefficient  $D$ .

For a broader introduction the reader is referred to the references Meek and Craggs<sup>56</sup> and Kuffel and Zaengl<sup>57</sup>. In Rees<sup>64</sup> an overview is given of the original work on electrical breakdown in gases under various conditions, for the complete texts see <sup>59-63,65-67</sup>.

## 2.3 Two-dimensional model

### 2.3.1 Species and considered processes

A 2-D, rotationally symmetric, discharge model with a 2-D field calculation routine which incorporates space charge is discussed here. The modelling techniques are presented in detail by Kennedy<sup>19</sup>. The 2-D hydrodynamic model is based on the continuity equations. This leads to five coupled non-linear partial differential equations (PDE's) which are numerically solved together with Poisson's equation. The 2-D model describes the spatiotemporal development of the charged species densities (see **Table 2.1**), for a configuration as shown in **Fig.2.1**.

The gases considered are nitrogen and dry air.

The processes incorporated are shown in **Table 2.2**. The gas parameter data used<sup>68,69,70</sup> in the 2-D model simulations is described in **Appendix A**.

For nitrogen, attachment and detachment as well as conversion (charge exchange) processes do not play a role. For the incorporation of secondary processes different procedures are being used by various authors<sup>19,26,28,30,31,38,39,41,43,47,50</sup>.

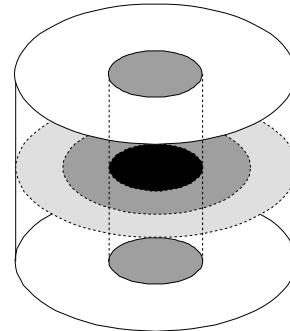


**Figure 2.1** 2-D model

**Table 2.1** Considered species in the 2-D model.

Particle species	N <sub>2</sub>	Dry Air	SF <sub>6</sub> <sup>*</sup>
electrons	x	x	x
positive ions	x	x	x
stable negative ions		x	x
unstable negative ions		x	x
excited species	x	x	x

**Table 2.2** Incorporated processes in the 2-D model.

Process	N <sub>2</sub>	Dry air	SF <sub>6</sub>
drift	x	x	x
diffusion	x	x	x
ionization	x	x	x
recombination	x	x	x
attachment		x	x
detachment		x	x
charge exchange		x	x
gas phase photoionization	x	x	x
secondary electron emission from surfaces by positive ion impact	x	x	x
secondary photoelectron emission from surfaces	x	x	x

---

\* For SF<sub>6</sub> we present measurements but no 2-D model simulations in this work.

### 2.3.2 Mathematical model

In the modelling the 0<sup>th</sup> moment mass conservation is used. To use the hydrodynamic model for the description of prebreakdown events we must have a collisionally dominated discharge. This is equivalent to maintaining dynamic equilibrium, i.e. the mean free path time between collisions needs to be much smaller than the timescale on which macroscopic changes take place. Under that condition the macroscopic gas discharge parameters defined in Section 2.2 to be meaningful. The 2<sup>nd</sup> moment energy conservation is not implemented.

The set of coupled non-linear PDE's describing the spatiotemporal species densities are: for the electron density

$$\frac{\partial N_e}{\partial t} + \nabla \cdot (v_e N_e) - \nabla \cdot (D_e \nabla N_e) = (\alpha - \eta_u - \eta_s) |v_e| N_e + N_{un} k_{ud} + N_{sn} k_{sd} - \epsilon_{pe} N_e N_p + S_{ph} \quad (2.18)$$

for the positive ion density

$$\frac{\partial N_p}{\partial t} - \nabla \cdot (v_p N_p) = \alpha |v_e| N_e - N_p (\epsilon_{pe} N_e + \epsilon_{pn} (N_{un} + N_{sn})) + S_{ph} \quad (2.19)$$

for the stable negative ion density

$$\frac{\partial N_{sn}}{\partial t} + \nabla \cdot (v_{sn} N_{sn}) = \eta_s |v_e| N_e - N_{sn} k_{sd} + N_{un} k_c - \epsilon_{pn} N_{sn} N_p \quad (2.20)$$

for the unstable negative ion density

$$\frac{\partial N_{un}}{\partial t} + \nabla \cdot (v_{un} N_{un}) = \eta_u |v_e| N_e - N_{un} (k_{ud} + k_c) - \epsilon_{pn} N_{un} N_p \quad (2.21)$$

From the solution of (2.18) we determine the excited species density

$$\frac{\partial N_m^*}{\partial t} = \delta_m |v_e| N_e - \frac{N_m^*}{\tau_m} \quad (2.22)$$

$N_{e,p,sn,un}$ : electron, positive ion, stable negative ion, unstable negative ion densities [ $cm^{-3}$ ]

$N_m^*$ : excited species ( $m^{\text{th}}$  electronic level) density [ $cm^{-3}$ ]

$v_{e,p,sn,un}$ : electron, positive ion, stable negative ion, unstable negative ion drift velocities

$D_e$	: electron diffusion tensor
$\alpha$	: ionization coefficient
$\eta_{s,u}$	: stable and unstable negative ion electron attachment coefficients
$k_{sd,ud}$	: stable and unstable negative ion electron detachment frequency
$k_c$	: ion conversion charge exchange frequency
$\epsilon_{pe,pn}$	: electron - positive ion and positive ion - negative ion recombination coefficients
$S_{ph}$	: gas phase photoionization process source term
$\delta_m$	: excitation coefficient for excitation to the m <sup>th</sup> electronic level
$\tau_m$	: deexcitation time constant for the excited species
$p$	: gas pressure
$p_q$	: quenching pressure
$d$	: electrode gap spacing, gap width [cm]

The species density flux, drift and diffusion terms are on the left hand side and the local and non-local gain and loss source terms are on the right hand side in the equations (2.18) to (2.22). The equations are coupled since species density terms that appear in one equation as a gain mechanism appear in the other as a loss mechanism.

When the local electrical field is modified by space charge, the coefficients in the above equations become space and time dependent.

Gauss's law gives the space charge field  $E_{space\ charge}$

$$\nabla \cdot E_{space\ charge} = \frac{\rho}{\epsilon_0} = \frac{e^-}{\epsilon_0} (N_p - N_e - N_{un} - N_{sn}) \quad (2.23)$$

For the total resultant electrical field  $E(\underline{r}, t)$  we then find

$$E(\vec{r}, t) = E_{Laplacian}(\vec{r}, t) + E_{space\ charge}(\vec{r}, t) \quad (2.24)$$

The above relations therefore become non-linear. Numerical techniques are required to come to a solution of the continuity equations coupled with Poisson's equation. The numerical techniques used, the flux corrected transport (FCT) algorithm<sup>33,37,42</sup> with Zalesac's peak preserver routine modifications<sup>29</sup>, are described in detail by Kennedy<sup>19</sup>.

The simulated discharge current  $i(t)$  is given by

$$i(t) = \frac{2\pi e}{d} \int_0^d \int_0^R \left[ \left( \sum_k^{charged\ species} \frac{+}{-} N_k v_{z_k} \right) - D_{z_e} \frac{dN_e}{dz} \right] \rho d\rho dz \quad (2.25)$$

in which  $R$ : simulation radius (0.6 cm)  
 $v_{z(e,p,sn,un)}$ : electron, positive ion, stable negative ion, unstable negative ion  
 drift velocities in axial direction  
 $D_{z,e}$ : electron diffusion in axial direction

The relaxation of the excited species density  $N_m^*$  serves as input to the calculation of the secondary photoelectron emission from surfaces<sup>28</sup> and the gas phase photoionization process source term  $S_{ph}$  to be used in (2.18) and (2.19).

The solution of (2.22) for  $N_m^*$  is given by

$$N_m^*(\rho', z', t) = \frac{P_{q_m}}{P^+ P_{q_m}} \int_0^t e^{\frac{-(t-t')}{\tau_m}} N_e(\rho', z', t') \delta_m(\rho', z', t') |v_e(\rho', z', t')| dt' \quad (2.26)$$

The secondary photoelectron emission photon flux density  $\Phi$  [number of photons/cm<sup>3</sup>] at location and time  $(\rho, z, t)$  due to a photon source at  $(\rho', z', t')$  is given by

$$\Phi(r)_{\text{photon}} = \int_0^d \int_0^{2\pi} \int_0^0 \frac{f(|r-r'|) N_m^*(\rho', z', t) (r-r')}{\tau_m |r-r'|^3} \rho' d\rho' d\varphi' dz' \quad (2.27)$$

in which

$$f(|r-r'|) = \frac{1}{4\pi} e^{-\mu_m |r-r'|} \quad (2.28)$$

and

$$|r-r'| = [(z - z')^2 + \rho^2 + \rho'^2 - 2\rho\rho'\cos(\varphi')]^{\frac{1}{2}} = [z'^2 + \rho^2 + \rho'^2 - 2\rho\rho'\cos(\varphi')]^{\frac{1}{2}} \quad (2.29)$$

$f(|r-r'|)$  is a function of photon absorption and subsequent photoelectron emission efficiency, and  $\mu_m$  is the photon absorption coefficient from the  $m^{\text{th}}$  electronic level in the neutral background gas.

The material quantum efficiency  $Q$  (number of electrons per number of photons) relates the electron flux  $\Gamma_e$  leaving the cathode to the photon flux  $\Phi(r)$

$$\Gamma_e(r, t) = N_e(r, t) v_e(r, t) = Q \Gamma_{\text{photon}}(r, t) = Q \Phi(r, t) \quad (2.30)$$

The secondary photoelectron emission density from surfaces  $N_{e, \text{secondary}}$  [number of electrons/cm<sup>2</sup>] at location and time  $(\rho, z=0, t)$  due to a photon source at  $(\rho', z', t)$  is

given by

$$N_e(\rho, z=0, t)|_{secondary} = \frac{Q}{|v_e(\rho, z=0, t)|} |\phi(\rho, z=0, t)| \quad (2.31)$$

The gas phase photoelectron-ion density  $N_{photon}$  [electrons/cm<sup>3</sup>] at location and time  $(\rho, z, t)$  due to a photon source at  $(\rho', z', t)$  is given by

$$N_{photon}(\rho, z, t) = \frac{p_{qm}}{p + p_{qm}} \int_0^{\rho} \int_0^{2\pi} \int_0^z \frac{g(|r-r'|) N_e(\rho', z', t) (r-r')}{|r-r'|^3} \rho' d\rho' d\varphi' dz' \quad (2.32)$$

in which

$$g(|r-r'|) = p \alpha(\rho', z', t) \Psi(|r-r'|p) \mu_l(\rho - \rho', |z'-z|, \varphi') \quad (2.33)$$

and

$$|r-r'| = [(z-z')^2 + \rho^2 + \rho'^2 - 2\rho\rho'\cos(\varphi')]^{\frac{1}{2}} \quad (2.29)$$

$g(|r-r'|)$  is a function of photon absorption and subsequent photoionization efficiency,  $\Psi$  is the photoionization coefficient and  $\mu_l$  is the photon absorption distance of the considered cylindrical volume element.

### 2.3.3 Numerical model and implementation

The calculation mesh consists of 120 linearly spaced axial and 22 linearly spaced radial elements. The simulation is started by an initial gaussian electron distribution at the cathode (emitting area  $0.008 / 0.03 / 0.07 / 0.13 / 0.2 / 0.28 / 0.39 / 0.5 \text{ cm}^2$ ), which represents the initial electrons induced in the experimental setup by cathode photoemission from a pulsed  $N_2$ -laser (pulse duration  $0.6 \text{ ns}$  (full width at half maximum)\*\*).

The 2-D hydrodynamic model has been implemented in FORTRAN 77 program code and runs both on personal computer (PC) or mainframe based systems. The typical simulation time is in the order of six hours on a  $133 \text{ MHz } 32 \text{ Mb}$  Pentium based PC system and around three hours cpu-time on a mainframe system (Silicon Graphics Power Challenge XL, IRIX

---

\*\* For the modelling we assume that the cathode and anode electrodes are perfectly transparent grids, so (apart from the mentioned processes) there is no interaction between the charged particles and the electrodes.

operating system (a variant of UNIX)<sup>\*\*\*</sup>. For critical calculations which may take longer cpu-times the simulations are in the order of twentyfour hours to a week on a mainframe.

Particle density distributions give insight in the formation phases leading to breakdown. These are compared with data from optical measurements of discharge activity. From this relevant processes and parameters can be determined. This will enable us to strip the complex physical 2-D hydrodynamic model developed initially to a "simplified" model only incorporating the dominant species. The model does not (yet) involve the influence of an insulating spacer.

In Sections 4.2 and 4.3 the following resulting quantities for  $N_2$  and dry air will be shown (**Table 2.3**): the resulting external current  $i(t)$ , the particle densities of electrons  $e^-$ , positive ions  $p^+$ , stable negative ions  $sn^-$  and unstable negative ions  $un^-$ , excited species  $N_m^*$ , and the electrical field  $E$ .

**Table 2.3** Resulting output of the 2-D model.

Results for nitrogen	Results for dry air
$i(t)$	$i(t)$
$e^- \quad p^+$	$e^- \quad p^+ \quad sn^- \quad un^-$
excited species $N_m^*$	excited species $N_m^*$
$E(r,z,t)$	$E(r,z,t)$

<sup>\*\*\*</sup> Configuration: 14 R8000 processors with 4 Mb cache each (utilizing only one designated processor at a time here), 1.5 Gb central memory, six 4.3 Gb discs + ten 2 Gb discs.

## Chapter 3

### Experiments

In this chapter the design aspects of diagnostics for prebreakdown phenomena are discussed. The resulting experimental setup together with the measurement procedures to measure the electrical discharge current with a 500 ps time-resolution and the optical discharge activity with a 60  $\mu\text{m}$  spatial- and 5 ns time-resolution are presented.

#### 3.1 Coupling between the charge movement in the gas and the current in the external circuit

In this section the coupling between the spatial charge movement in the gas and the external current induced is presented. A small charge  $q$  crossing a gap under the influence of a field  $E(x)$  induces a current  $i$  in the external circuit until it reaches the other side (see **Fig.3.1**). The electrical energy input  $iVdt$  supplied by the source in a time interval  $dt$  equals the work  $W=qEdx$  done by the electric field to move the charge over a distance  $dx$ . For the current we can write

$$i = \frac{qE(x)}{V} \frac{dx}{dt} = \frac{qv(x)E(x)}{V} \quad (3.2)$$

where  $v(x)=dx/dt$  is the velocity of the charge in the direction of  $E$ .

The duration of the current pulse is equal to the charge's transit time. When the charge  $q$  reaches the anode it is neutralized by the image charge, which has grown to  $-q$  during the transit time, and all activity ceases.

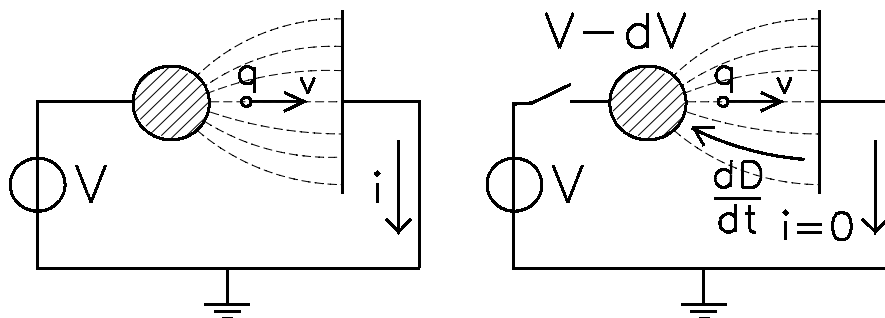


**Fig.3.1** Left: Current induced in a closed circuit by a charge crossing a gap.  
Right: Voltage drop induced in an open circuit by a charge crossing a gap.



**Fig.3.2** Current in external circuit for a constant charge crossing a gap in a homogeneous field (left) and inhomogeneous field (right).

For a homogeneous field and constant charge  $q$  the current pulse is rectangular as shown in **Fig.3.2**, and (3.1) becomes

$$i = \frac{qv}{d} \quad (3.1a)$$

$d$ : gap spacing [cm]

In a homogeneous field configuration we can observe the growth of the charge  $q(t)$ , when  $q$  is not constant and from this for example determine the ionization coefficient  $\alpha$ . The drift velocity  $v$  is determined from the transit time.

In an inhomogeneous field as in Fig.3.1 the current pulse drops considerably with time even for a constant charge  $q$  as shown in Fig.3.2. Not only the field  $E(x)$  drops during the crossing, but also the velocity  $v$  in the region of low field. In inhomogeneous fields the charge often crosses only part of the gap. This occurs in the case of corona, partial discharges and for a.c. voltages where the charge transit times are larger than the half cycle period.

When the charge crosses the gap completely, an amount of charge also equal to  $q$  flows through the external circuit. If the charge crosses only a part of the gap, say  $dx$  and thereby traverses a voltage difference  $\Delta V$ , a charge equal to the apparent charge  $q_{app}$  flows through the external circuit. Integration of equation (3.1) yields

$$q_{app} = \int_0^{\infty} i dt = \frac{q}{V} \int_0^{\infty} E(x) v dt = \frac{q}{V} \int E(x) dx = q \frac{\Delta V}{V}$$

It is clear that the  $q_{app}$  to  $q$  ratio can be much smaller than one. The current in the external circuit can be considered to result from the change in electric flux towards the electrodes

and the corresponding varying charge on the electrodes. This current is, of course, also influenced by the external circuit. In the extreme case that the circuit is interrupted as shown in Fig.3.1, no current flows at all. In this case the moving charge still causes a change of electric flux towards the electrodes, which is however compensated by a displacement current  $\partial D/\partial t$ . The work done by the field is now provided by the capacitive energy

$$W_c = \frac{1}{2} C V^2$$

$$\Delta W_e = \Delta\left(\frac{1}{2} C V^2\right) = \frac{1}{2} C \Delta(V^2) = C V \Delta V$$

and therefore the voltage across the gap drops.

### 3.2 Design aspects of diagnostics for prebreakdown measurements

If we consider the equivalent circuit of **Fig.3.3** we can derive (see Kuffel and Zaengl<sup>57</sup>):

$$q_m = \frac{C_c}{C_t + C_c} q_{app} \quad (3.2)$$

$$C_t = \frac{\epsilon_0 A}{d} = \frac{\epsilon_0 \pi r_m^2}{d} \quad (3.3)$$

$q_m$ : measured charge (time integral of the measured current)

$C_c$ : coupling capacitance

$C_t$ : capacitance of the test object

$C_s$ : stray capacitance between measurement electrode and grounded ring

$R_d$ : large damping resistor, so no charge flows through this damping resistor during the prebreakdown phase

$R$ : 50  $\Omega$  resistance consisting of four 200  $\Omega$  parallel resistors in (low inductance) star configuration

$Z_0$ : characteristic impedance of the coaxial cable and terminating impedance of the oscilloscope

$r_m$ : radius of the measurement electrode [cm]

If we fulfil the condition  $C_c \gg C_t$ , the measured charge is equal to the apparent charge

$$q_m = \frac{C_c}{C_t + C_c} q_{app} \approx q_{app} \quad (\text{for } C_c \gg C_t) \quad (3.2a)$$

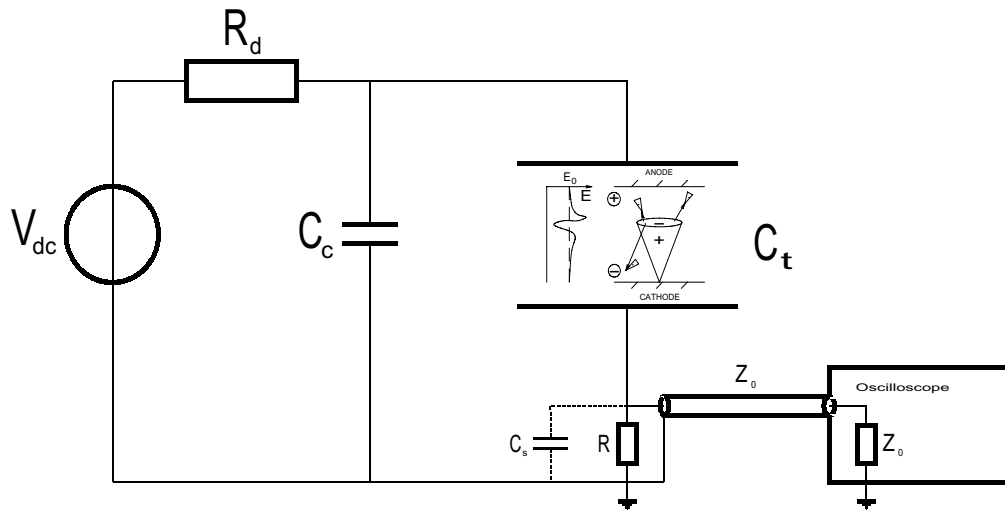


**Fig.3.3** Equivalent circuit of the discharge measurement setup.

This equation describes that if the coupling capacitance (which is essential to do high frequency quantitative measurements!) is much larger than the capacitance of the test object the voltage source can be considered to be decoupled. On the timescale considered the discharge current is fully supplied by the coupling capacitance. In theory the discharge measurement impedance could also be located in the branch of  $C_c$  in Fig.3.3, as in many of the used setups in practice. For fast time-resolved discharge measurements however it is more advantageous to directly measure in the branch of the test object  $C_t$  for a better sensitivity and better high-frequency response (see section 3.3).

In all experiments a subdivided electrode configuration is used to fulfil the condition in formula (3.2a) and to allow high bandwidth measurements. The subdivided electrode consists of a small disk (measurement electrode) surrounded by a grounded ring. The high voltage electrode together with the grounded ring forms the large coupling capacitance  $C_c$  close to the measurement electrode to keep the inductance low and avoid travelling waves. The damping resistor  $R_d$  serves as a means of limiting the current in case of breakdown between the high voltage electrode and the subdivided electrode. The resistor  $R_d$  is placed close to the high voltage electrode to avoid the influence of reflecting travelling waves on the high voltage lead. To prevent field enhancement at the edges of the high voltage electrode and to maintain a uniform field in the central region we use a Bruce-profile for the high voltage electrode<sup>71</sup>.

**Ramo-Shockley considerations**

When a charge moves in a multi-electrode configuration as the one considered here, the induced charge and corresponding current of one single electrode may be derived from Ramo-Shockley considerations<sup>72,73</sup>. In our setup, the radius of the measuring disk  $r_m$  should be small to keep the stray capacitance  $C_s$  small, but on the other hand large enough to ensure that the discharge does not induce a current in the ground connection of the surrounding ring. According to Ramo-Shockley considerations these conditions are met for<sup>72,73,74</sup>

$$d \leq \frac{1}{2} r_m \quad (3.4)$$

For  $r_m = 2.0 \text{ cm}$ , substitution in formula (3.4) yields  $d \leq \frac{1}{2} r_m = 1.0 \text{ cm}$ .

If we require  $q_m \approx q_{app}$  within 10% we can easily derive from equation (3.2) the condition

$$C_c = \frac{\epsilon_0 \pi (r^2 - r_m^2)}{d} \gg C_t = \frac{\epsilon_0 \pi r_m^2}{d} \quad (\text{for } r \gg r_m) \quad (3.5)$$

$$r^2 \gg 2 r_m^2 \Rightarrow r \gg \sqrt{2} r_m \quad (3.6)$$

numerically for the 10%

$$C_c \geq 9 C_t$$

$$r^2 \geq 18 r_m^2 \Rightarrow r \geq 3\sqrt{2} r_m \quad (3.7)$$

$r$ : radius of the high voltage electrode [cm]

Substitution of formula (3.7) gives

$$r \geq 3\sqrt{2} r_m = 3\sqrt{2} \cdot 2.0 \text{ cm} = 8.5 \text{ cm}.$$

**Response of the measuring system**

The measuring system is limited in bandwidth. Several factors play an important role:

1) The circuit has an  $RC$ -time determined by the measuring impedance, the capacitance  $C_t$  between high voltage electrode and measurement electrode (in case  $C_c \gg C_t$ ) and the stray capacitance  $C_s$ . This results in a maximum bandwidth, which corresponds to a minimum 10%-90% rise time

$$t_{10\% - 90\%} = \ln(9) \tau_1 = \ln(9) RC = \ln(9) R \left[ C_s + \frac{C_c C_t}{C_c + C_t} \right] \quad (3.8)$$

2) The measurement instrument, here a digital oscilloscope, has a maximum analog bandwidth of 500 MHz (2 Gsamples/second) and minimum time between sampling points of  $\tau_2=500 \text{ ps}$ \*\*\*\*.

The maximum bandwidth of the complete system, for independent rise times, yields<sup>20</sup>:

$$\tau = \sqrt{\tau_1^2 + \tau_2^2} \quad (3.9)$$

$$f_{\max} = \frac{1}{2\pi\tau} \quad (3.10)$$

3) Inductance effects: have been minimized by compact subdivided electrode design with low inductance resistor configuration.

4) Bandwidth limitation by coaxial cable limited by short cable length: and the use of a carefully selected cable<sup>75</sup>.

**Table 3.1** shows the values for the bandwidth of the considered configurations.

If necessary in the 2-D model computer simulations we can use a low-bandpass filter with  $f_c=f_{\max}$  ( $\tau=RC$ ) to include the experimental bandwidth limitations.

**Table 3.3** Response of the measuring system.

Field configuration	$C_c$ [pF]	$C_t$ [pF]	$C_s$ [pF]	$R$ [ $\Omega$ ]	$t_{10\%-90\%}$ [ps]	$\tau$ [ps]	$f_{\max}$ [MHz]
uniform	20.1	1.13	5.41	$\frac{1}{2}Z_0$	356	526	303
non-uniform half sphere	20.1	1.20	5.40	$0.2 \cdot Z_0$	144	504	316
non-uniform paraboloid	20.1	1.14	5.40	$0.2 \cdot Z_0$	143	504	316

\*\*\*\* We also have a HP 54720D digital oscilloscope (2 GHz bandwidth, 8 Gsamples/second) to our disposal for very fast time-resolved measurements.



focuses and diverges the light beam to an emitting cathode area  $A$ . The illuminated cathode area  $A$  can be varied through one or two lenses (SIGMA UV  $f=251\text{ mm}$ ,  $f=101\text{ mm}$ ) external to the chamber. To ensure the release of a significant number of electrons the cathode surface has to be polished. Different types of sandpaper were used for this and the resulting photoemission was compared. Cloth based non-waterproof sandpaper p180, p320, p400, pjh400 and waterproof p220, p380, p400, p800 and special plastic based sandpaper were tested. The advantage of cloth based sandpaper is that it collects sandpaper dust by adhesion which avoids electrostatically charged dust particles in the inter-electrode gap space. The use of cloth based non-waterproof sandpaper p320 turned out to be the most effective. The maximum quantum efficiency  $Q$  (number of released electrons per incident number of photons) is approximately  $10^{-7}$ . The initial electrons move towards the anode and undergo ionizing collisions thereby creating an avalanche. Upon arrival at the anode the electrons leave the gap. The slowly drifting ions move towards the cathode.

### 3.3.2 Discharge vessel

To obtain a uniform field, a Bruce-profile electrode with an overall radius of  $8.5\text{ cm}$  is used. A subdivided electrode configuration, with a  $2\text{ cm}$  measuring disc radius and a  $15.5\text{ cm}$  grounded ring (cathode) radius and an annular gap between the two parts of  $0.1\text{ mm}$  at the cathode surface, allows high bandwidth measurement of the charge induced on the measurement electrode<sup>21</sup>. The measured voltage drop over a  $50\ \Omega$  resistor (at the oscilloscope) is the representation of the true discharge current in the gap. Thereby in our setup design the induced apparent charge is equal to the real charge. To improve the bandwidth of the setup four  $200\ \Omega$  parallel resistors are built into the subdivided electrode configuration, yielding  $50\ \Omega$  in parallel to the  $50\ \Omega$  terminating impedance of the oscilloscope.

A Wallis Electronics Ltd. (type R605/05P (positive) or V.C.S. 300/1 + Opt. A (negative)), output voltage  $0$  to  $+60\text{ kV}$  or  $-30\text{ kV}$  and a maximum ripple of  $20\text{ ppm}$  peak to peak, was used as dc voltage source. For higher voltages up to  $115\text{ kV}$  an eight stage Greinacher-cascade circuit<sup>57,77</sup> (developed in-house) in combination with a (Wallis Electronics Ltd., type V.C.S. 303/1) a.c. voltage source was used. The applied voltage is measured by a resistive divider formed by  $R_1=2\text{ G}\Omega$  (134 resistors of  $15\text{ M}\Omega$  in series) and  $R_2=200\text{ k}\Omega$  and a (Digitech, model 2780) digital voltmeter. The accuracy of the voltage measurement is approximately 1%. The damping resistor  $R_d=1.05\text{ M}\Omega$  protects the electrodes and the voltage source in case of breakdown. Two anti-parallel diodes (type 1N4151) protect the oscilloscope's input unit in case of breakdown.

A rotary vane pump (ALCATEL, type PASCAL 2021SD) is used to reduce the chamber pressure to approximately  $10^{-2}\text{ Pa}$ . Below  $10^{-2}\text{ Pa}$  a turbo-molecular pump (Balzers, type TPH240 with a DUO 004B first-stage pump and a TCP380 Power Supply) is used to further reduce the pressure to  $2\cdot 10^{-3}\text{ Pa}$ . The vacuum pressure is measured by a Pirani cold cathode gauge system (Balzers, type PKG010). The gas under test pressure is measured by a Penwalt (type FA-160, range  $0 - 50\text{ torr}$ ) or a Balzers absolute pressure gauge

(type APG010, range 0 - 1200 mbar). The temperature in the vessel can be measured within 0.1 °C. The water vapor content of the gas filling is measured by an Endress+Hauser Hygrolg (type WMY 170, dew point range -80 to +20 °C).

The electrode distance is variable and can be measured outside the vessel with an accuracy of 0.02 mm. The vessel is equipped with a port with a long rubber glove which enables manipulation of objects inside the vessel (at ambient pressures) without opening it. For higher or lower pressures this port is covered, and the pressure at both sides is kept equal by means of a by-pass.

### 3.3.3 Optical diagnostics

An ICCD camera records the optical discharge activity. The ICCD camera used has a (minimum) shutter time of 5 ns. This camera (Princeton Instruments, type 576G/RB) has a 576x384 pixel array designed for operation from the UV to NIR range (180 nm to 800 nm). The image intensifier photocathode's quantum efficiency at  $\lambda=300$  nm is larger than 12%. A variable gain allows a sensitivity of 1 to 80 counts per photoelectron. The CCD chip is (water) cooled through a peltier element mounted on the backside, to thereby reduce the thermal noise resulting in dark current, as well as nitrogen flushed to prevent condensation of moisture. To increase the signal-to-noise ratio to a pixel intensity of 4 for a maximum intensity of  $2^{14}$ , the dark current ICCD image recording is subtracted from the corresponding ICCD images in the experiments. For the shutter gating a gate pulse generator (Princeton Instruments, type FG100) is used. The total ICCD camera system has a 25 ns minimum delay time with respect to the time at which the initial electrons are released from the cathode of the setup. A (general purpose) lens (SIGMA f/5.6, 180 mm) is used to focus the image onto the photocathode of the image intensifier. In practice test images were used to adjust the lens for maximum optical focus and minimum optical depth of field. The ICCD camera is triggered via an antenna near the  $N_2$ -laser which initiates the discharge through the release of a sufficient number of electrons from the cathode surface. A programmable delay enables the choice of any opening moment of the camera beyond 25 ns after the start of the avalanche.

For the measurement of the optical discharge activity of streamers and of discharge activity in the presence of spacers an ICCD camera and two photomultipliers (Thorn EMI, type 9817 S20 QB) with UV / IR filters were used. For the photomultipliers an applied voltage of  $V=1.2$  kV was used (linear amplification was obtained for  $0.7$  kV <  $V$  <  $1.2$  kV). The wavelength characteristics of the filters used are shown in **Fig.3.5**.

Equation (3.11) relates photon energy  $E$  in eV to the emitted wavelength  $\lambda$  in nm upon release of such a photon from an excited state atom

$$E = h\nu = h \frac{c}{\lambda}$$

$$\lambda = \frac{hc}{E} = \frac{hc}{E(\text{eV})q} = \frac{1.24 \times 10^3}{E(\text{eV})} \quad (3.11)$$

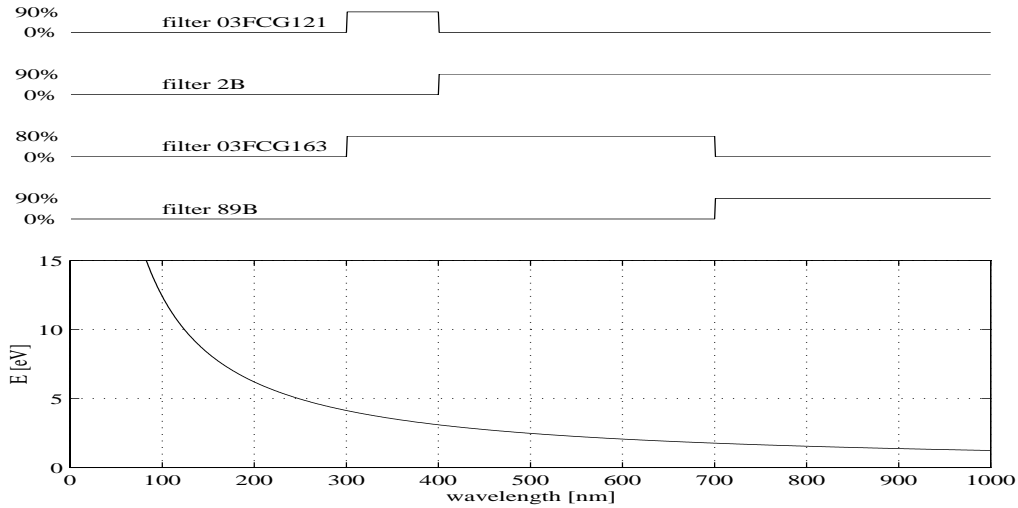


**Fig.3.5** UV / IR filter wavelengths schematically indicating optical transmission regions. Also indicated is the relation between photon energies and corresponding wavelengths.

### 3.3.4 Measurement electrode geometry

For the non-uniform field configuration the experimental setup's bandwidth was  $316 \text{ MHz}$ . Since sensitivity is not a critical requirement, eight  $100 \ \Omega$  resistors in star configuration in parallel to the  $50 \ \Omega$  measuring impedance of the oscilloscope were used resulting in  $R=10 \ \Omega$ .

With a Boundary Element Method (B.E.M.), i.e. ELECTRO (Integrated Engineering Software Ltd.), field calculations were made for the considered field configurations, to assess the field enhancement factors, to allow a Ramo-Shockley analysis and to obtain the capacitance-matrices of the electrode configurations.

For the considered electrode configurations **Fig.3.6** shows:

- \* equipotential lines during normal operation (on top)
- \* equipotential lines for the Ramo-Shockley configuration (note that for a Ramo-Shockley evaluation the measurement electrode is at unit potential while all other electrodes are at zero potential) (in the middle).
- \* Ramo-Shockley field from cathode to anode along the axis of rotational symmetry (bottom).

At the top the anode is shown and at the bottom the subdivided electrode with the measuring disc on the left. On the axis of rotational symmetry at the left the hole in the center of the anode for the  $N_2$ -laser beam is shown. From the equipotential line plot we can

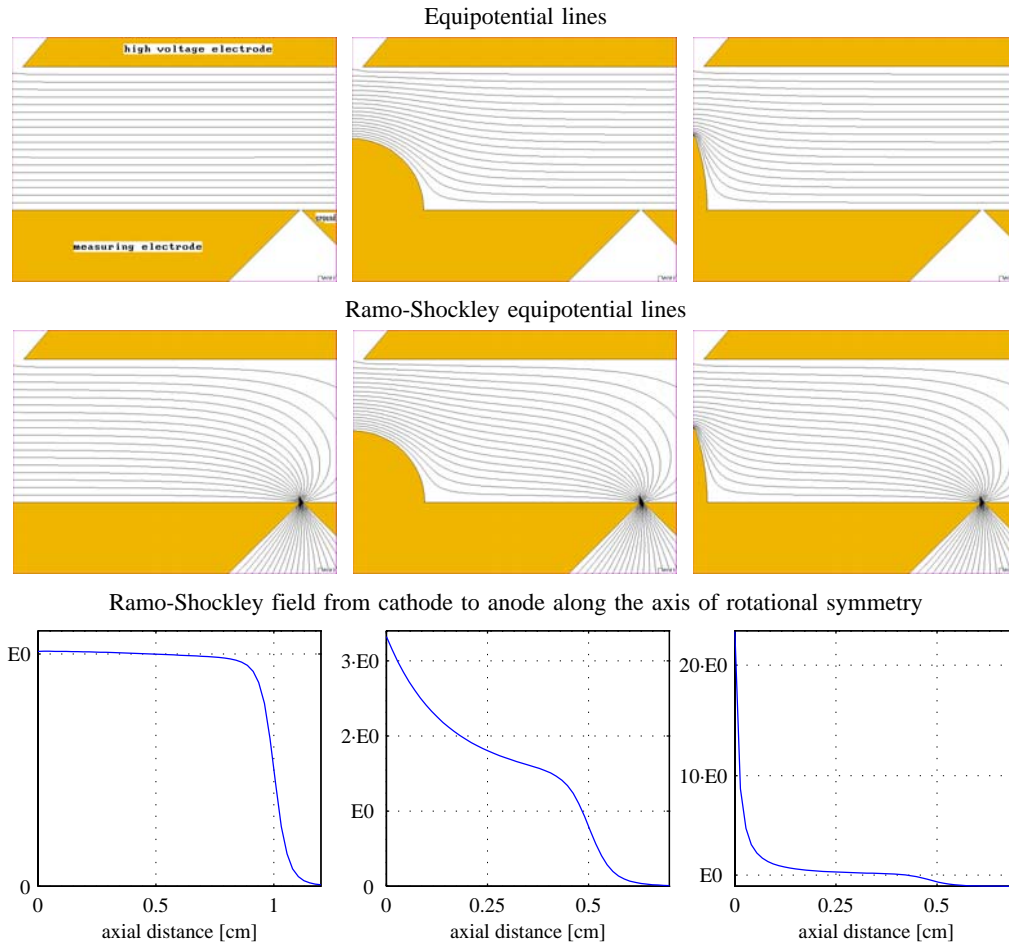


**Fig.3.6** Considered electrode configurations, equipotential lines (top), Ramo-Shockley equipotential lines (middle), Ramo-Shockley field value distributions from cathode to anode along the axis of rotational symmetry (bottom) in uniform and non-uniform fields.

see the nice uniform field for the first configuration (left) and field enhancement for the non-uniform field configurations. From the Ramo-Shockley equipotential line plot (in the middle on the left) it can be seen how the field is constant from cathode to anode in the central part of the measurement disc. For the non-uniform field configurations the equipotential line plots show the variation of the electrical field in the inter-electrode gap. The Ramo-Shockley field (bottom) is approximately constant from cathode to anode along the axis of rotational symmetry for the uniform field configuration. As a result the discharge

will only induce charge on the measurement electrode. For the non-uniform field configurations the field decreases quickly, from the value at the tip ( $3.3 \cdot E_0$  respectively  $23 \cdot E_0$ ,  $E_0$  is the uniform field value), to a very low value with increasing distance from cathode to anode. The capacitance-matrices' values relevant for the response of the measuring system's analysis are incorporated in Table 3.1.

### 3.3.5 Spacer geometries

For the measurements of discharges near spacers, the spacers were placed between the parallel electrodes as shown in **Fig.3.7**. The electrodes were slightly pressed together as to make sure the spacers were in good contact with the electrode surfaces. **Figure 3.8** shows B.E.M. equipotential lines for the considered spacer configurations. An overview of the field configurations used in this thesis is shown in Figs.3.6 and 3.7.

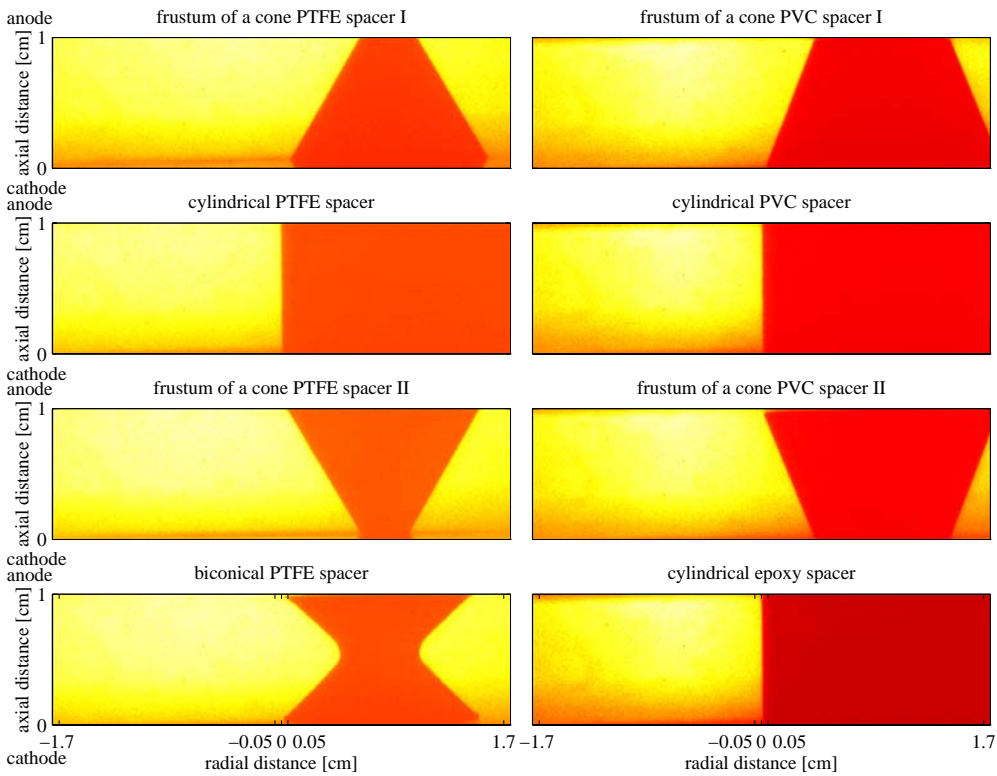


**Fig.3.7** Considered configurations in the experimental setup for measurements of discharges along spacers in air.

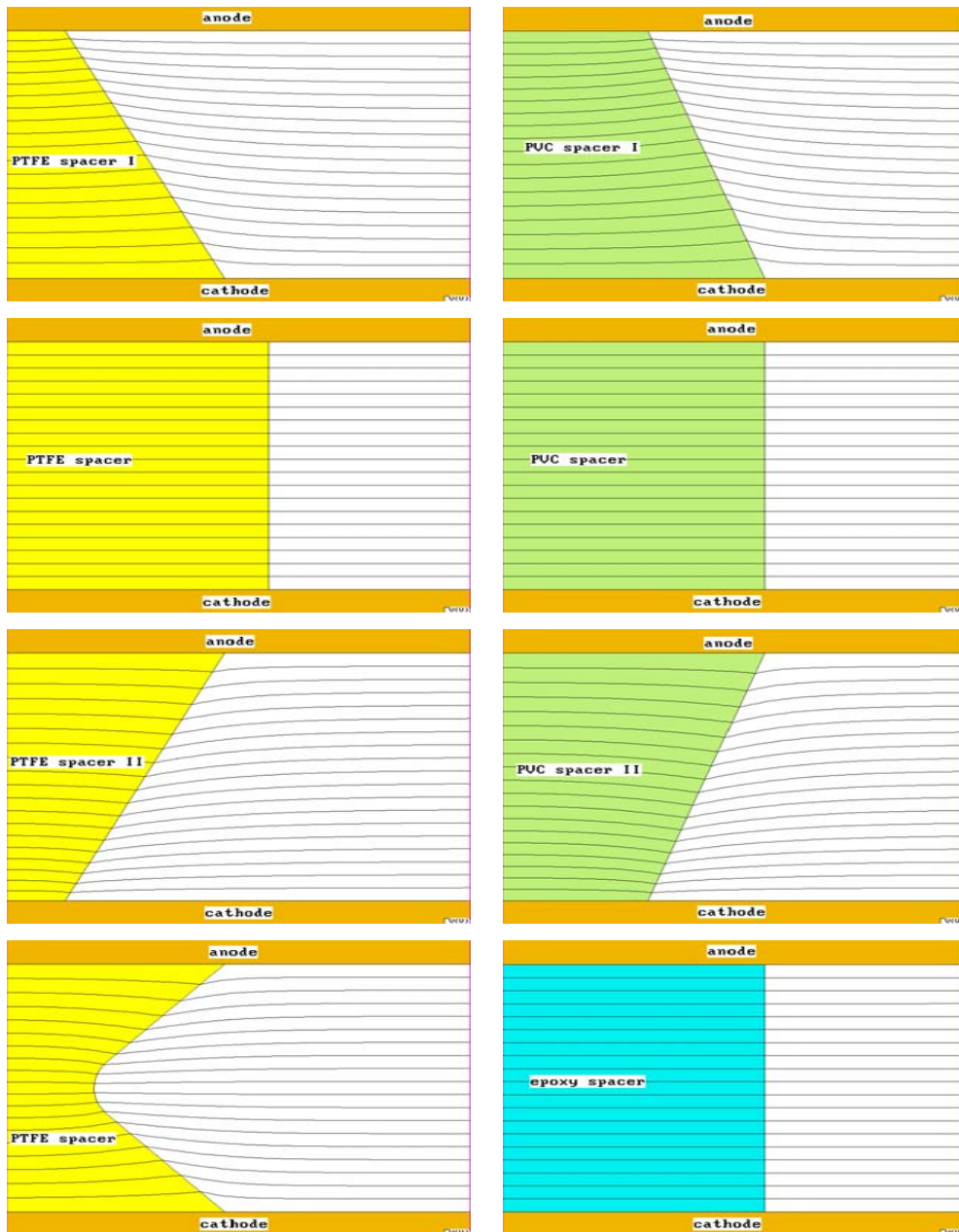


**Fig.3.8** Equipotential lines for the considered configurations in the experimental setup for measurements of discharges along spacers in air.

### 3.4 Measurement procedure

The optical and electrical discharge activity are measured:

- optical discharge activity:   \* ICCD camera images  
   \* two photomultipliers with UV / IR filters
- electrical discharge activity: \* measured discharge current.

First the vessel is evacuated to a pressure below  $2 \cdot 10^{-3}$  Pa. The vessel is filled to atmospheric pressure with (technically pure) nitrogen or dry air respectively. The cathode surface is treated with sandpaper to achieve the release of large electron numbers through photoemission. The 0.6% magnesium content in the aluminium electrode material<sup>\*\*\*\*</sup> is responsible for photoemission at photon-energies as low as  $3.68$  eV<sup>78</sup>.

For the measurements with  $SF_6$  the vessel is first evacuated to a pressure below  $2 \cdot 10^{-3}$  Pa. The vessel is filled to atmospheric pressure with (technically pure) nitrogen. The cathode surface is treated with sandpaper to ease the release of large electron numbers through photoemission. Then the vessel is evacuated again to a pressure below  $2 \cdot 10^{-3}$  Pa and thereafter filled to the desired pressure with (technically pure)  $SF_6$ .

The software controlled automated setup starts measurements by firing the  $N_2$ -laser, which triggers the pulsed ICCD camera and an HP 54542A digital oscilloscope, to record the spatiotemporal light activity and the discharge current waveform.

Optical discharge activity recordings are made with both 5 ns en 20 ns ICCD camera shutter times.

The gases under study are nitrogen, dry air and  $SF_6$ . Experiments were done in the parameter ranges shown in **Table 3.2**. The number of initial electrons  $N_0$  (as extrapolated from the measurements) ranged from  $N_0=1 \cdot 10^5$  to  $4 \cdot 10^8$  electrons.

---

\*\*\*\* Aluminium alloy type 6351 (1% Si, 0.6% Mg, 1% Mg).

**Table 3.2** Field configurations considered.

Field configuration	Gas	Pressure [Pa]	Voltage range [kV]	Electrode gap [cm]
uniform	N <sub>2</sub>	$1.02 \cdot 10^5$	26 - 30.5	1
	dry air	$1.02 \cdot 10^5$	26 - 30.5	1
	SF <sub>6</sub>	$1.3 \cdot 10^3 - 4 \cdot 10^4$	3 - 36	1
non-uniform half sphere paraboloid	SF <sub>6</sub>	$1.02 \cdot 10^5$	4 - 90	0.5 - 1
spacer PTFE PVC epoxy	dry air	$1.02 \cdot 10^5$	29 - 30.5	1

### 3.5 Partial discharges

In Chapter 5 the measuring techniques for the application to partial discharges in voids are presented, together with a discussion of other applications.



## Chapter 4

### Experimental and Modelling Results

*In this chapter the experimental results for various gases are presented. Discharges in uniform and non-uniform field conditions, with and without space charge, and with and without a spacer present, are considered. The results are compared with results from 2-D hydrodynamic model calculations. We also discuss studies in which a number of parameters are varied.*

#### 4.1 Introduction

The experimental setup described in Chapter 3 is used to measure the time-resolved discharge current and the optical discharge activity. Results of the 2-D hydrodynamic model described in Chapter 2 are presented, for electrical discharges in nitrogen and in dry air in uniform applied fields. Experimental results for a uniform applied field without and with space charge field distortion, a non-uniform field and a geometry without and with a spacer are presented.

The study of avalanches in a "simple" non-attaching inert gas, i.e.  $N_2$ , and the modelling of the "simple" case of gas-breakdown in  $N_2$  are tackled first. Secondly, avalanche experiments and simulations for electronegative gases, i.e. dry air and  $SF_6$  are presented. Breakdown in these gases involves more complex processes; and the modelling becomes more elaborate, since now a number of processes have to be correctly incorporated and since the computer simulations take a longer time.

The stages of avalanche-to-streamer transition and dielectric breakdown in  $N_2$ , dry air and  $SF_6$ , are presented in Section 4.3.

The time-to-breakdown  $t_{bd}$  and the electron transit time  $T_e$  in a uniform field in nitrogen and dry air are evaluated as a function of applied (Laplacian) field, the initial electron number, the pressure and the pressure reduced field  $E/p$ .

To complete the chapter experiments on prebreakdown phenomena in dry air along insulator surfaces are presented in Section 4.4.

Throughout this chapter the definitions of quantities and processes given below will be used.

The **electron transit time in a uniform field**  $T_e$  is the time required for the primary electron avalanche to travel from cathode to anode in a uniform field with no space charge.

$$T_e = \frac{d}{v_e} \quad (4.1)$$

(This is the time associated with the electron drift velocity)

In the presence of space charge the avalanche transit time differs from the electron transit time and we will here use for  $T_e$  the time at which the, initially negative, net charge  $N_{q,net}$  in the gap (due to the initial photoelectrons) becomes positive. In the experiments we assume that this approximately coincides with the first current maximum.

The **minimum field for gas-breakdown**  $E_{min}(N_0, d)$  is defined as the field value below which no breakdown occurs for a given number of initial electrons at an electrode gap width  $d$ .

The **minimum critical electron number for gas-breakdown**  $N_{0,min}(E, d)$  is defined as the number of initial electrons below which no breakdown occurs for a given applied field strength  $E$  at an electrode gap width  $d$ . The initial electron number  $N_0$  is derived from extrapolation of the exponential current curve to  $t=0$  in the experiments.

The **transition point electron number for gas-breakdown**  $N_{0,tr}(E, d)$  is defined as the number of initial electrons above which streamer formation is enabled before the initial electron avalanche reaches the anode for a given applied field strength  $E$  at an electrode gap width  $d$ .

#### **Cathode directed streamer (CDS)**

A streamer with an ionizing front moving towards the cathode, due to gas phase photoionization (as by definition from Raether<sup>60</sup> and Loeb and Meek<sup>61</sup>), or due to increased ionization in the space charge distorted enhanced field.

#### **Anode directed streamer (ADS)**

A streamer with an ionizing front moving towards the anode, due to gas phase photoionization (as by definition from Raether<sup>60</sup> and Loeb and Meek<sup>61</sup>), or due to increased ionization in the space charge distorted enhanced field.

#### **Undervolted breakdown**

Breakdown at voltages below the static breakdown voltage of a gas.

Description of the **Trichel-pulse**<sup>56,79,80</sup> discharge mechanism:

A Trichel pulse starts with one or more electrons generated at the negative high field electrode region in a non-uniform field electrode geometry in attaching gases at atmospheric pressures. The electrons are accelerated, rapidly moving away from the negative non-uniform field electrode, thereby ionizing the gas, leaving behind slowly drifting positive ions. The space charge field created between the electron and ion swarm is opposite to the applied Laplacian field, thereby reducing to total resultant field until no effective ionization takes place anymore; the avalanche is cut off (quenched). The electrons will attach to gas molecules or atoms and form a negative ion cloud (since they have too little energy to create new electron-ion pairs,  $\alpha \cdot \eta < 0$  so  $E/p < (E/p)_{crit}$ ). The negative ion cloud will slowly drift towards the anode and the positive ions will slowly drift towards the cathode in an electric field that increases when the positive ions approach the cathode. These positive ions impinge on the cathode surface releasing new electrons by secondary electron emission. As soon as the negative space charge cloud has drifted away far enough to roughly restore the initial applied field a new avalanche will start.

#### **Corona-stabilization**<sup>81</sup> **in non-uniform fields**

The initially unstable situation causes corona activity which builds up space charge. Space charge reduces the field and as a result the corona activity ceases. Instead of leading to a full breakdown, discharge activity remains restricted to a small volume around the high field electrode. This is called corona-stabilization. New corona discharges will be formed only after the charge clouds have sufficiently drifted away.

Throughout this chapter in the presentation of data, results of the current waveforms are plotted on a linear- and log-scale, and on the horizontal axes the time is normalized to the electron transit time in a uniform field  $T_e$ . The figures of simulation results for species densities are on a logarithmic intensity scale. (This enables a better analysis of the obtained results.)

## 4.2 Avalanches in uniform applied fields

### 4.2.1 Avalanches in Nitrogen

#### Experimental observations

##### Optical study of the avalanche formation in atmospheric nitrogen<sup>6</sup>

Results for a uniform applied field with space charge field distortion are presented.

**Figure 4.1** shows results of previous work<sup>6,19,82</sup>, in which  $20\text{ ns}$  ICCD camera gate-shutter times were used. Characteristic is the cloudy character of the optical activity. Images *a* through *d* show the primary avalanche's arrival at the anode and the formation of the subsequent "cathode directed streamer" (CDS) in the mid-gap enhanced field region, initiated by "delayed electrons" residing in this region.

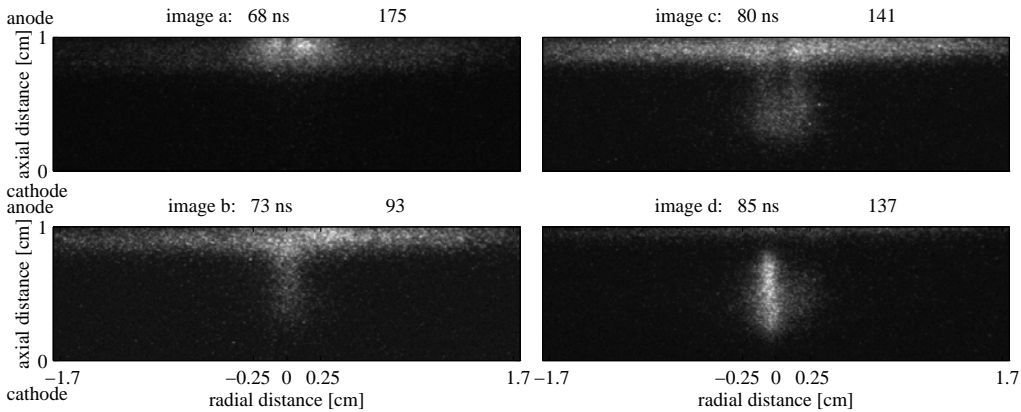


**Fig.4.1** Sequence of ICCD camera images showing a (laser-induced) avalanche and its transition to a streamer. In the figure the corresponding times with respect to the start of the avalanche are indicated. The cathode (bottom) and anode (top) surfaces are located at  $0$  and  $1\text{ cm}$  respectively on the vertical axis. The horizontal scaling in centimeters is also indicated. The initial electrons are released at  $t=0$  from the cathode (bottom) region around  $x=0$  ( $-0.25\text{ cm} < x < 0.25\text{ cm}$ ),  $N_0=3 \cdot 10^8$ ,  $T_e=68\text{ ns}$ . The maximum photon count per pixel is denoted in the upper right corner of each image.  $20\text{ ns}$  ICCD camera gate-shutter time. Linear intensity scale. (In these measurements by Kennedy<sup>19</sup> a variable ICCD gain was used.)

Conditions: atmospheric nitrogen  $E=30\text{ kV/cm}$ ,  $gap=1\text{ cm}$ .

**Figure 4.2** shows the measured current waveform (on a linear- and log-scale) and ICCD-images with  $5\text{ ns}$  gate-shutter times, recorded earlier in the avalanche development, prior to streamer onset for a 60 times smaller initial electron number. The illuminated area here is  $0.07\text{ cm}^2$ . The initial electron number is derived from extrapolation of the exponential

current curve to  $t=0$ . As was shown earlier<sup>19</sup> the current waveform strongly depends on the initial conditions.

Successive electron avalanches are clearly distinguishable. The reproducibility of the waveforms is quite good. Here only one (of 52 waveforms) is shown.

Two generations of optical activity crossing the gap from cathode to anode are observed, and in the same time span two electron avalanches show up in the measured current. From the value of the maximum photon count per pixel (denoted in the upper right corner of each image) it is seen that the optical activity is rather intense at first (image *a*) and decreases upon the radial expansion with progressing time (image *b*), despite the exponential charge growth and the increase in number of ionizing collisions.

From the ICCD images (with different exposure times in Figs.4.1 and 4.2) we see:

- 1) the "clouds" of optical activity observed at "long" ( $20\text{ ns}$ ) exposure times consist of a number of small active regions,
- 2) the discharge activity shows a considerable radial expansion\*.

The distribution is spreading out radially during the primary avalanche's transit. The reason for this will be discussed in Section 4.3.1.

It is not due to space charge, since a significant radial field cannot yet have formed under these discharge conditions nor does diffusion alone account for the observed distribution of optical discharge activity. The measurements performed earlier by Kennedy<sup>19</sup> with a  $20\text{ ns}$  shutter time at later times (see Fig.4.1) are in good agreement with our observations.

### Simulation results

**Figure 4.3** shows the corresponding simulated avalanche current waveform, the total net number of charge carriers  $N_{q,net}$  (positive ions  $N_p$  minus electrons  $N_e$ ) and the total number of electrons as a function of time (top), together with the density distributions of the electrons, positive ions and excited species and the resulting electrical field at various time instances for an illuminated area of  $A=0.07\text{ cm}^2$ . On the horizontal axes in Figs. 4.2 and 4.3 the time is normalized to the electron transit time in a uniform field  $T_e$ . According to experimental observation data by Wen<sup>20</sup>, without the presence of space charge,  $T_e$  is  $83\text{ ns}$ . This is in agreement with the result of the 2-D model simulation ( $T_e=83\text{ ns}$ ). From our experimental data a primary electron transit time of  $65\text{ ns}$  is found for the considered conditions (for a further discussion on this see page 44).

---

\* It is not due to an optical detection limit as was checked with a logarithmic intensity representation, from which we concluded we are well above an optical detection threshold.

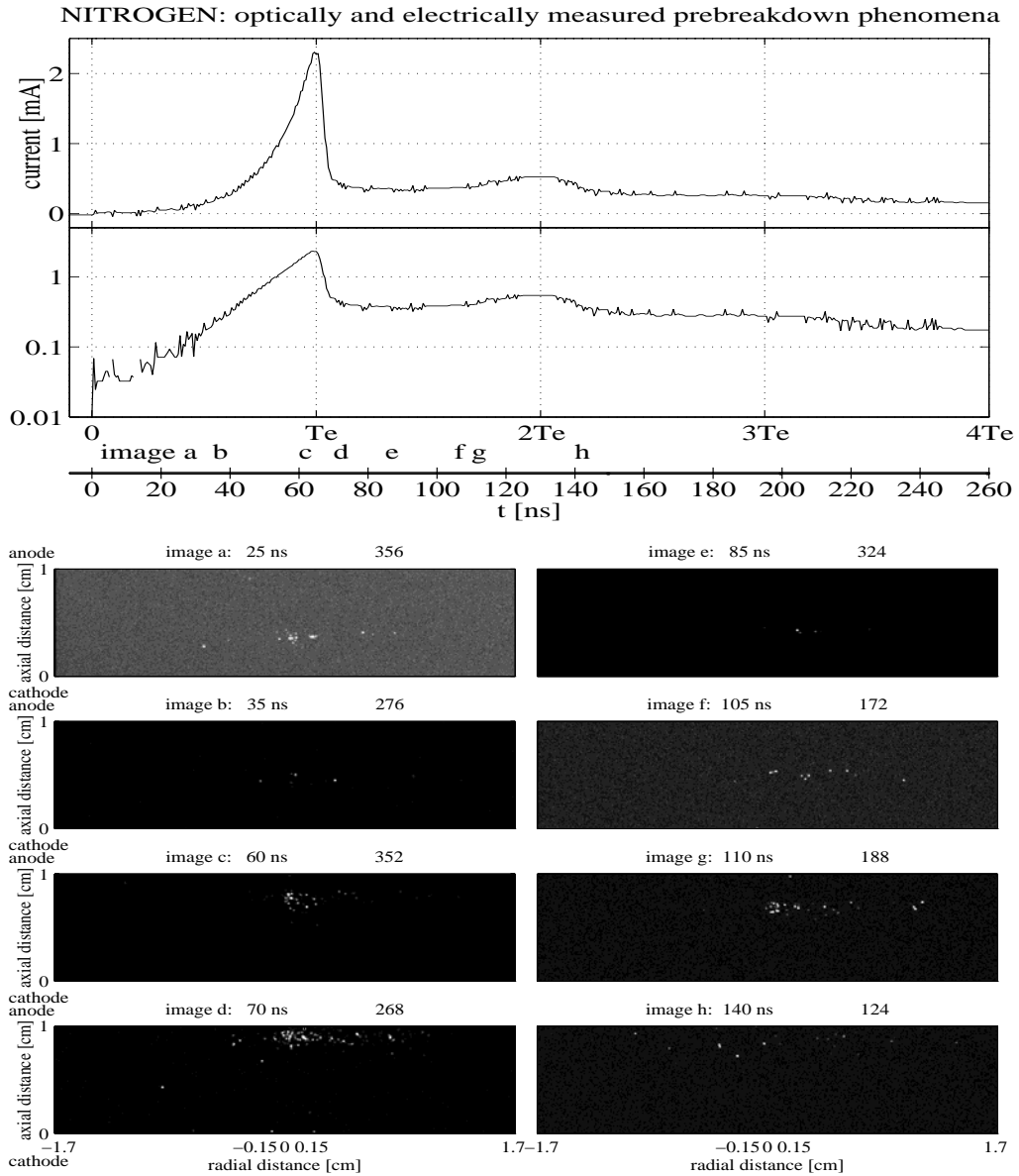


**Fig.4.2** Measured current waveform ( $N_0=5.3 \cdot 10^6$ ,  $T_e=65$  ns) and sequence of ICCD camera images of a laser-induced avalanche. The initial electrons are released at  $t=0$  from the cathode (bottom) region around  $x=0$  ( $-0.15$  cm  $< x < 0.15$  cm). Gate-shutter time of ICCD camera is 5 ns. Logarithmic intensity scale. (Legends as in Fig.4.1.)

Conditions: atmospheric nitrogen  $E=30$  kV/cm, gap=1 cm.

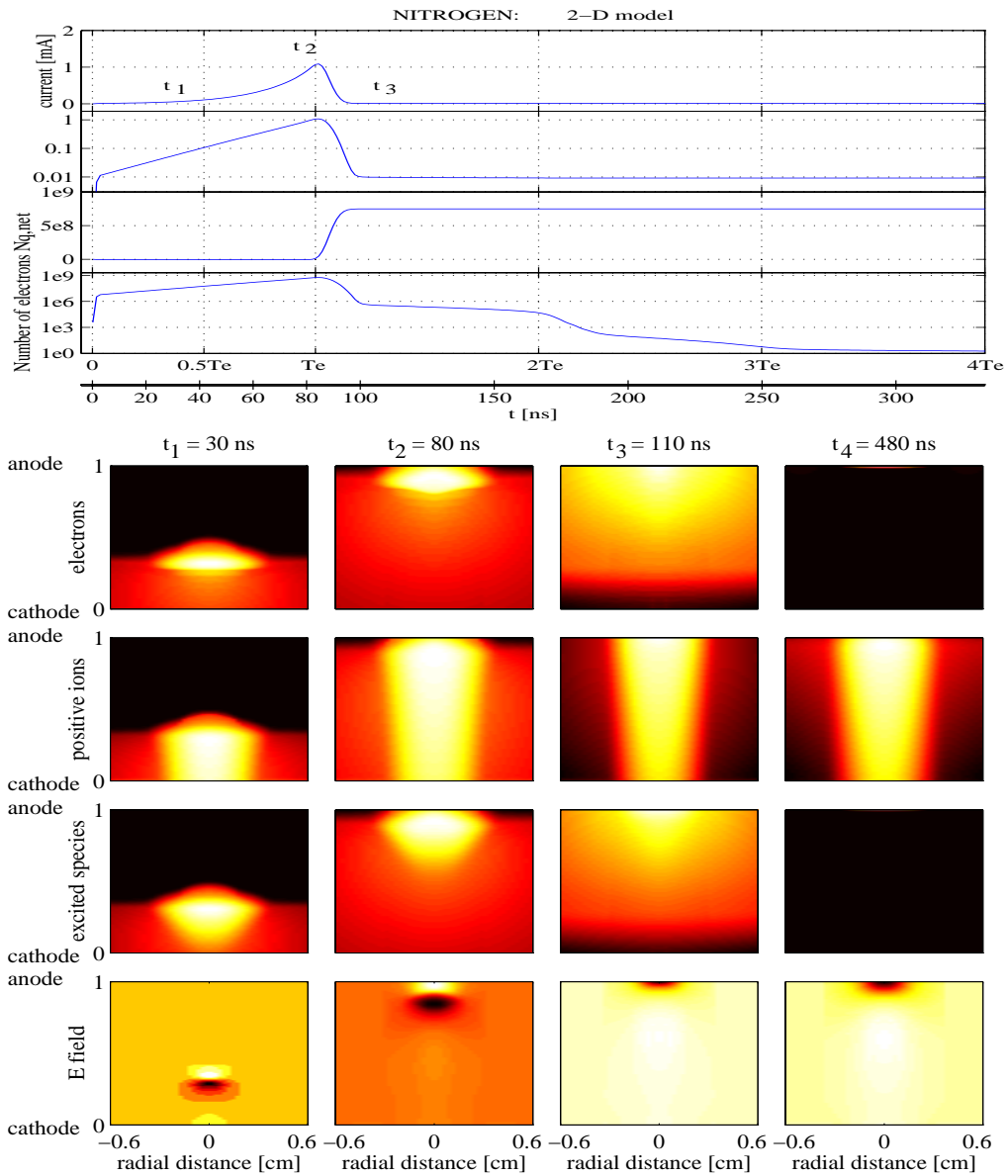


**Fig.4.3** Simulated current waveform ( $N_0=5.5 \cdot 10^6$ ,  $T_e=83$  ns,  $A=0.07$  cm<sup>2</sup>). Electron, positive ion and excited species density and resultant electrical field at various time instances. Conditions: atmospheric nitrogen  $E=30$  kV/cm, gap=1 cm.

### Influence of the applied voltage

**Figure 4.4** shows measured and simulated current waveforms for atmospheric nitrogen (and dry air) at different applied voltages. The waveforms are shown both on a linear- and log-scale. On the horizontal axes the time is normalized to the simulated electron transit time in a uniform field  $T_e$ . The illuminated area here is  $0.07 \text{ cm}^2$ . The reproducibility of the waveforms is quite good. In earlier work by Kennedy<sup>19</sup> the current peak was observed to broaden due to space charge effects. Such "peak broadening" is not observed here, the reason for this will be discussed in section 4.3.1.

Successive electron avalanches are clearly distinguishable.

- \* For voltages well below the breakdown voltage the laser-induced prebreakdown phenomena are of the avalanche type.
- \* For higher voltages the amplitude of the subsequent secondary electron generations increases.
- \* At  $29 \text{ kV}$  these start to lead to laser-induced breakdown with times-to-breakdown well over two times the electron transit time in a uniform field.
- \* For  $30 \text{ kV}$  breakdown times are varying and are found to be between  $T_e$  and  $6T_e$ . Over  $30.5 \text{ kV}$  (not shown) we subsequently observe breakdown in the first electron transit time, irrespective of the number of laser-induced first electrons.

- $30 \text{ kV}$ :
- 1) experimentally we observe a great variation in the time-to-breakdown (the gap broke down after several series of measurements since we are just slightly below the static dc breakdown voltage)
  - 2) in the simulations the time-to-breakdown is strongly dependent on the initial conditions (only a slight change in the chosen initial electron distribution at these conditions leads to a complete breakdown)
  - 3) this strong dependence on the initial number of electrons apparently explains the observed large spread in the time-to-breakdown.

The 2-D hydrodynamic model provides a good description of the external current for these conditions.

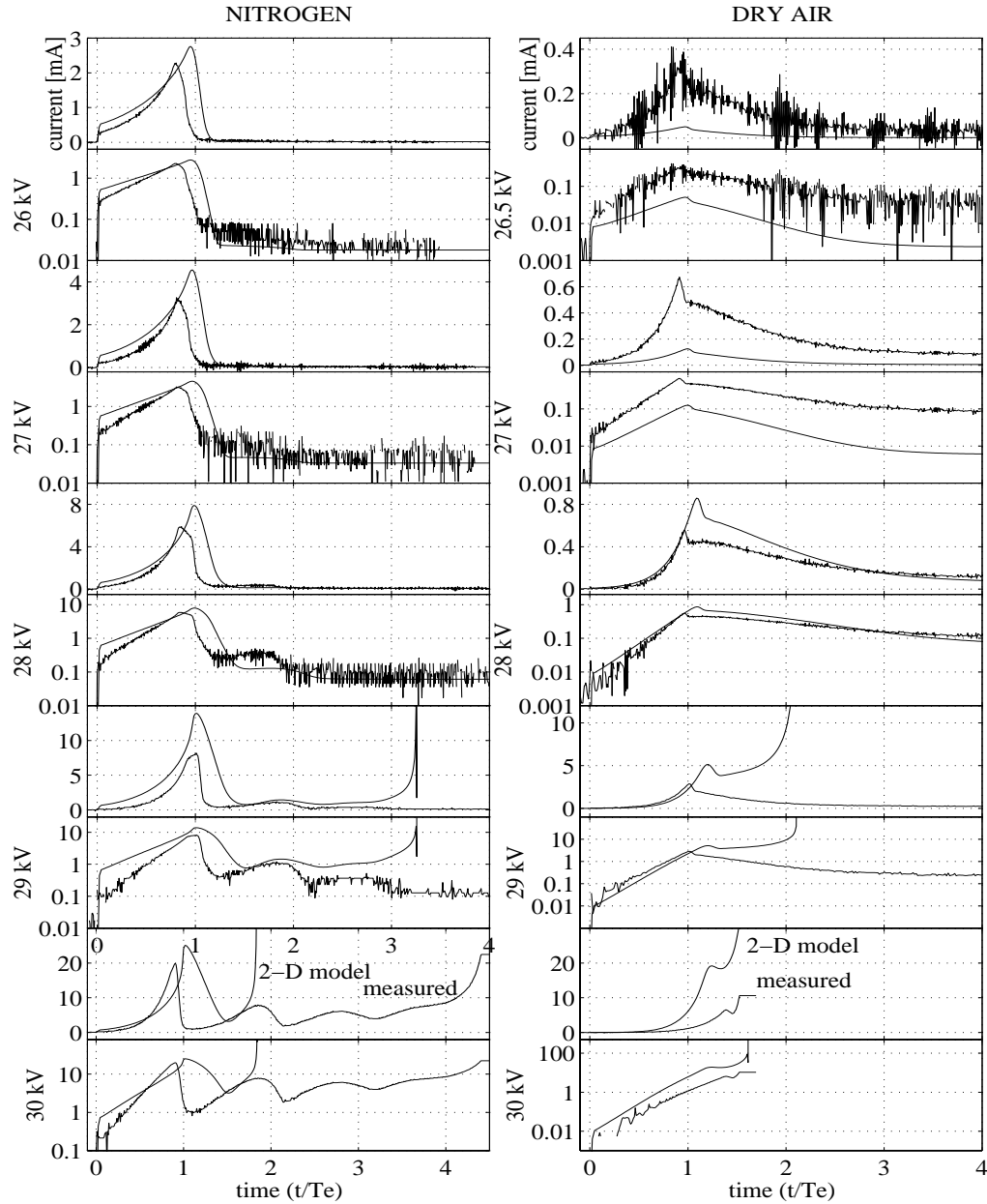


**Fig.4.4** Measured and simulated current waveforms for nitrogen and dry air at different applied voltages (on a linear- and log-scale).

Conditions: atmospheric nitrogen  $E=26\text{-}30\text{ kV/cm}$ , electrode gap= $1\text{ cm}$  ( $N_0=2\cdot 10^8$ )  
atmospheric dry air  $E=26.5\text{-}30\text{ kV/cm}$ , electrode gap= $1\text{ cm}$  ( $N_0=5\cdot 10^6$ ).

### 4.2.2 Avalanches in Dry Air

#### Experimental observations and simulation results

##### Avalanche formation in dry air<sup>7</sup>

**Figure 4.5** shows a simulated avalanche current waveform, the total net number of charge carriers  $N_{q,net}$  (positive ions  $N_p$  minus electrons  $N_e$  and stable  $N_{sn}$  and unstable negative ions  $N_{un}$ ) and the total number of electrons as a function of time (top), together with the density distributions of electrons, positive ions, stable negative ions, unstable negative ions and excited species and the resulting electrical field at various time instances. Dry air and nitrogen show a similar avalanche formation behaviour with increasing voltage (Fig.4.4). However, after the primary avalanche (for  $t > T_e$ ), differences are observed in the streamer initiated breakdown formation. This is ascribed to the different production mechanisms of secondary electrons: for  $N_2$ , gas phase photoionization is responsible for streamer formation and propagation, whereas for dry air detachment, in particular from unstable ( $O^-$ ) negative ions, is the dominant mechanism for supplying delayed electrons in regions with breakdown conditions ( $\alpha - \eta > 0$ , or  $E > E_{crit.}$ ). From Fig.4.4 we observed undervolted breakdown in both  $N_2$  and in dry air for laser-initiated discharges, as a result of space charge.

As for  $N_2$ , the avalanche growth at voltages close to breakdown depends critically on the initial conditions. This causes a possible mismatch between calculated and measured waveforms.

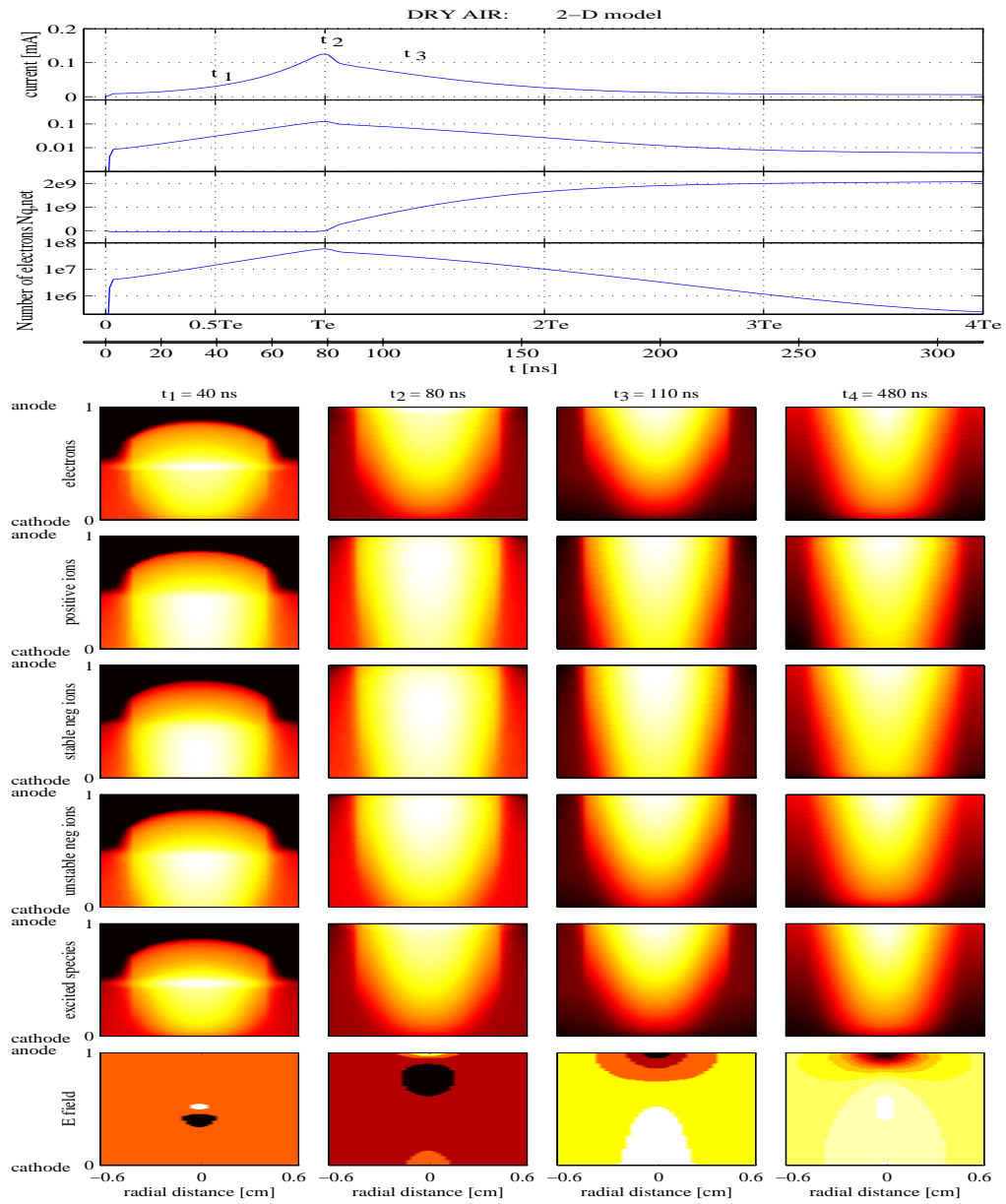


**Fig.4.5** Simulated current waveform ( $N_0=4.1 \cdot 10^6$ ,  $T_e=79$  ns,  $A=0.46$  cm<sup>2</sup>).  
 Electron, positive ion, stable negative ion, unstable negative ion and excited species density  
 and resulting electrical field at various time instances.  
 Conditions: atmospheric air  $E=27$  kV/cm, gap=1 cm.

**Table 4.1** Electron transit time  $T_e$  in a uniform field for a 1 cm gap in atmospheric nitrogen ( $N_0=3 \cdot 10^8$ ) and dry air ( $N_0=4 \cdot 10^6$ ).

V [kV]	N <sub>2</sub> :		T <sub>e</sub> [ns]		DRY Wen <sup>20</sup>	AIR:		T <sub>e</sub> [ns]
	Wen <sup>20</sup>	2-D model	experiments	experiments		2-D model	experiments	
26	100	97	78		81	85		
26.5	97	93	77		80	82	80	
27	94	90	75		79	79	76	
28	87	83	70		76	71	70	
29	84	74	70		74	61	61	
30	83	65	59		71	54	74	

### Electron transit time

**Table 4.1** shows the electron transit time in a uniform field  $T_e$ , derived from experimental data for the electron velocity  $v_e$  as a function of the pressure reduced field  $E/p$  without space charge by Wen<sup>20</sup>, and the values obtained from the 2-D model simulations and the experiments reported in this work for nitrogen and dry air at different applied voltages. For low voltages ( $<28$  kV) agreement is found with the results of the 2-D model simulations. The electron transit time from our experiments roughly agrees with the modelling data for the considered conditions (the differences in Table 4.1 are due to the used definition of  $T_e$  given in section 4.1, as can be seen for air from Fig.4.4 at 30 kV). The differences at higher voltages are due to the space charge enhanced electron motion.

In the absence of space charge the electron velocity is constant and not modified by the space charge field, as shown by the resulting electrical field in Fig.4.3 at  $t=80$  ns.

In the presence of space charge, the field in front of the avalanche at the avalanche head is modified to such an extent that the electrons gain a higher energy  $qV$  resulting in a higher electron velocity and smaller electron transit time, as shown for nitrogen in Fig.4.12 at  $t=65$  ns, and for dry air in Fig.4.17 at  $t=50$  ns. For air this occurs at much lower initial electron numbers since the presence of negative ions results in a larger space charge field.

In the absence of space charge:  $T_e$  is only dependent on  $E/p$ .

In the presence of space charge:  $T_e$  is also dependent on  $N_0$  (as will be discussed in the context of Fig.4.20).

### 4.2.3 Avalanches in $SF_6$

#### Experimental observations

##### Optical & electrical study of the avalanche formation in sulfurhexafluoride<sup>10</sup>

Results for prebreakdown in a **uniform applied field** without and with space charge field distortion are presented.

Processes responsible for the formation of a cathode directed streamer will be discussed.

**Figure 4.6** shows typical, measured prebreakdown currents in  $SF_6$  at a pressure of  $2 \cdot 10^4 Pa$  and different sizes of the area  $A$  from which the initial electrons are released. As was shown earlier<sup>7</sup> the current waveform strongly depends on the initial conditions. The reproducibility of the waveforms is quite good. On the horizontal axis the electron transit time in a uniform field  $T_e$  is indicated and on the vertical axis the current is normalized to its initial value  $i_0$ . From our experimental data a primary electron transit time of  $30 ns$  was found for the considered conditions, which is consistent with earlier work<sup>20,21,40</sup>.

Only the primary electron avalanche is clearly distinguishable, i.e. we observe a gradual growth to breakdown without clear secondary electron avalanches.

The waveform change in the first avalanche demonstrates the presence of significant space charge: with decreasing emitting area the initial electron density increases which results in a smaller transit time  $T_e$ . The optical activity prior to the avalanche's arrival at the anode (not shown here) is much weaker than in  $N_2$  or dry air<sup>\*\*</sup>. This indicates that attachment of electrons is significantly reducing avalanche growth. At the early stages the observed optical activity (not shown) was spread out in radial direction, similar to the observations for  $N_2$  and dry air, which is due to the in Section 4.3.1 discussed artifact of the experimental setup which leads to the release of initial electrons over a broader cathode region.

The large delay time between the first avalanche and (streamer) breakdown formation, and the very low optical activity during this time span suggests that cathode photoelectron emission and gas phase photoionization do not play a significant role in the streamer formation. On the other hand gas phase photoionization is vital for streamer propagation once the streamer has been formed<sup>19</sup>. The cathode directed streamer formed in the mid-gap enhanced field region, initiated by delayed electrons residing in this region, is shown in images *a* and *b* of Fig.4.6b.

**Figure 4.7** shows typical, measured prebreakdown currents in  $SF_6$  for two values of the applied field. At the higher field, in spite of the much lower initial electron number, the avalanche growth during the first electron transit results in a significant reduction of the time-to-breakdown.

---

\*\* See footnote in Section 4.3.3, pp.77.

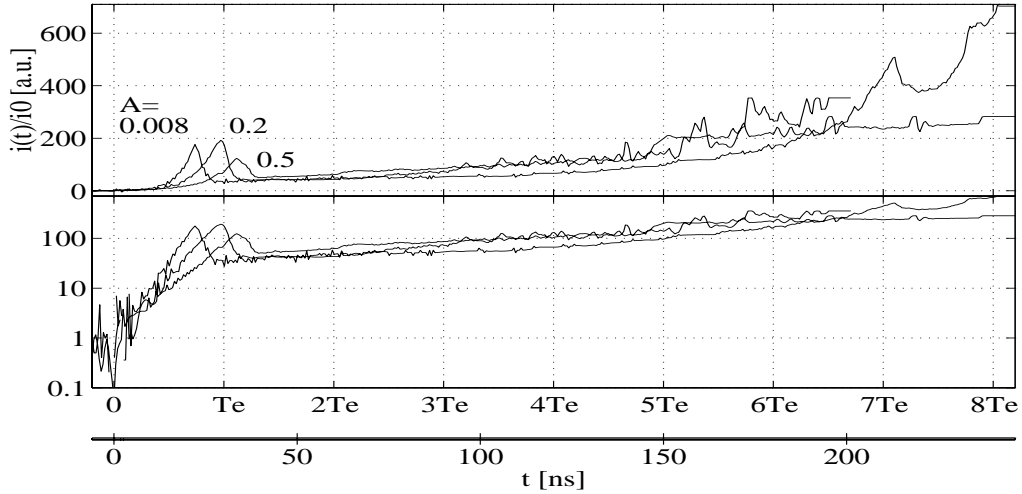


**Fig.4.6a** Measured current waveforms for different emitting areas ( $N_0=3.8 \cdot 10^6$ ,  $T_e=30$  ns for  $A=0.2$  cm<sup>2</sup>) (on a linear- and log-scale). Emitting cathode area  $A=0.008 / 0.2 / 0.5$  cm<sup>2</sup>.

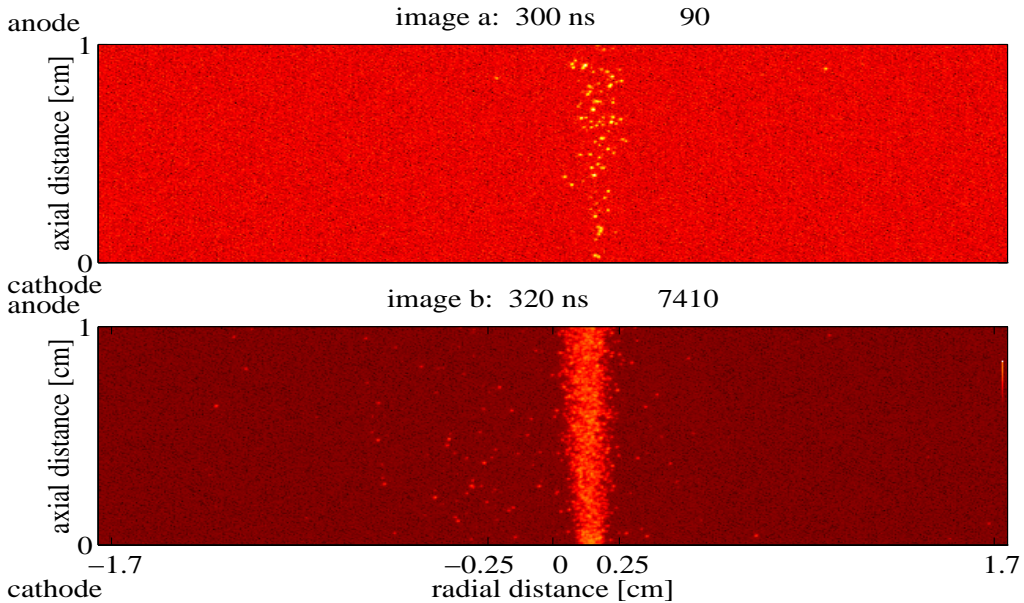


**Fig.4.6b** ICCD camera images showing a laser-induced avalanche and its transition to a streamer. The initial electrons are released at  $t=0$  from the cathode region around  $x=0$  ( $-0.25$  cm  $< x < 0.25$  cm). 5 ns ICCD camera gate-shutter time. Logarithmic intensity scale. Conditions:  $SF_6$  ( $p=2.0 \cdot 10^4$  Pa)  $E=18.3$  kV/cm electrode gap= $1$  cm.

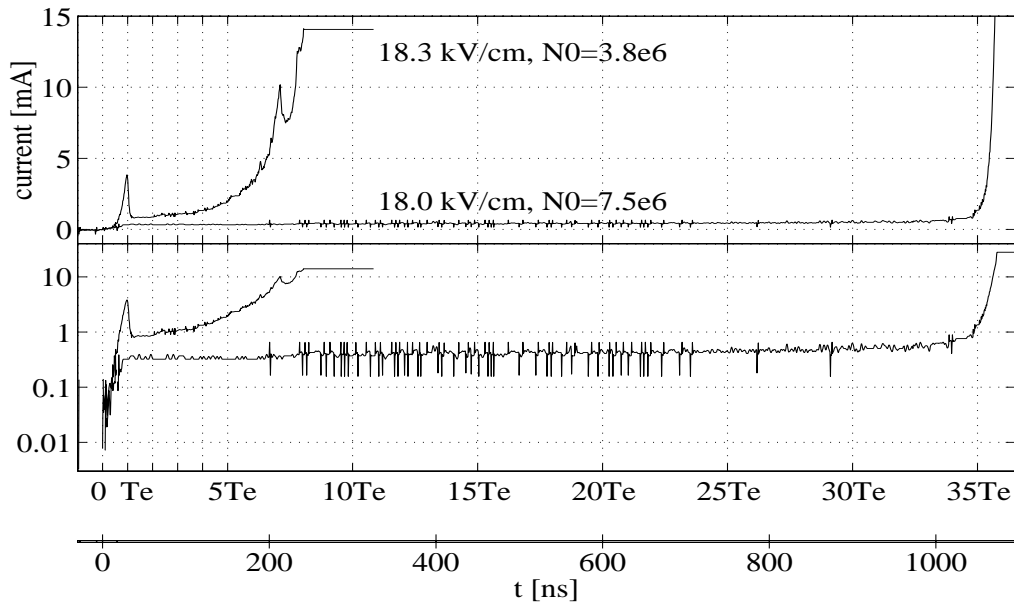


**Fig.4.7** Measured current waveforms for different applied fields

( $T_e=30$  ns) (on a linear- and log-scale).

Conditions:  $SF_6$  ( $p=2.0 \cdot 10^4$  Pa)  $E=18.0-18.3$  kV/cm, electrode gap=1 cm.

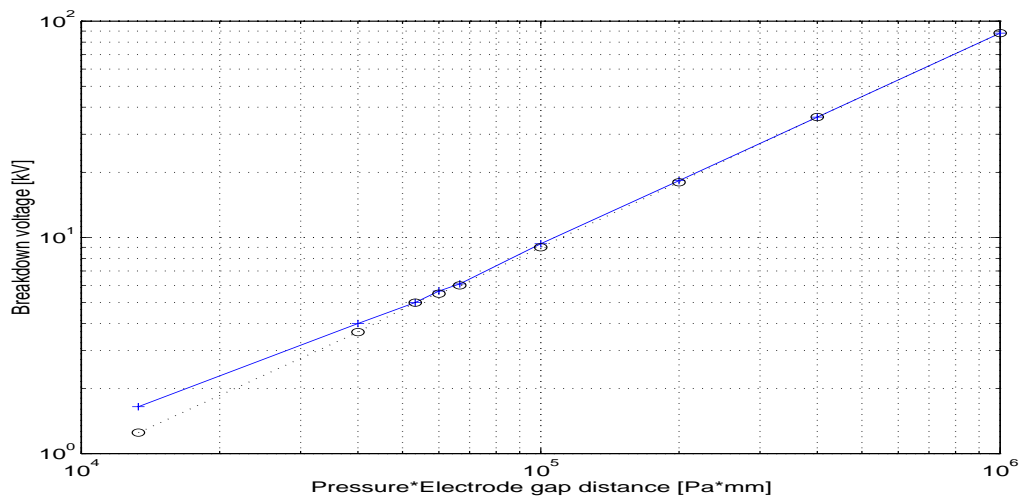


**Fig.4.8** Paschen-curve for  $SF_6$  ( $d=10$  mm).

Experimental + minimum spontaneous breakdown voltage

o minimum laser-induced breakdown voltage.

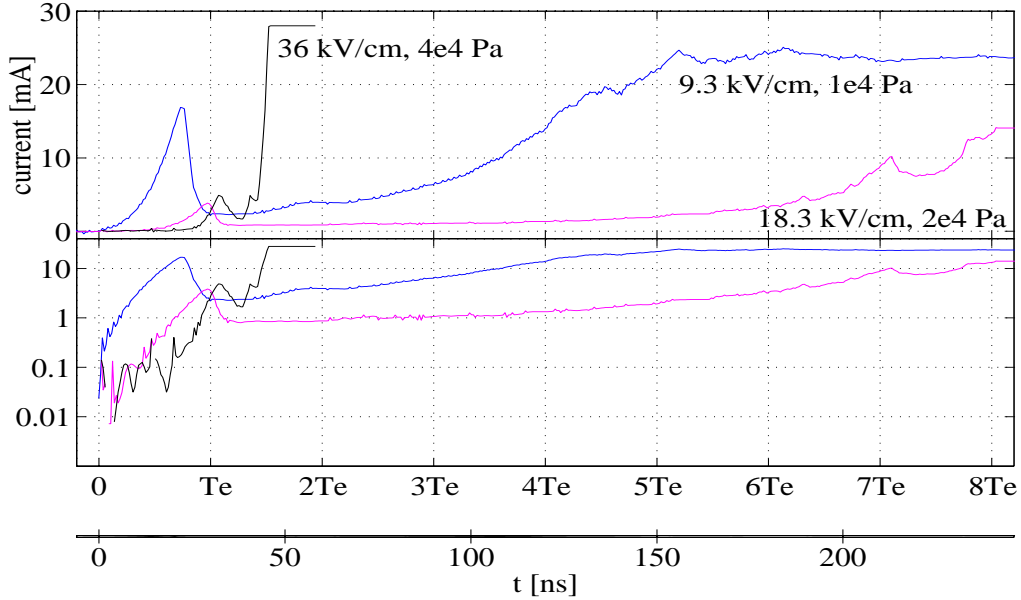


**Fig.4.9** Measured current waveforms for different pressures ( $p = 1 \cdot 10^4, 2 \cdot 10^4$  and  $4 \cdot 10^4$  Pa) ( $N_0 = 1.9 \cdot 10^6 - 3.8 \cdot 10^6$ ,  $T_e = 30$  ns) (on a linear- and log-scale).  
Conditions:  $SF_6$   $E = 9.3 - 36$  kV/cm, electrode gap = 1 cm.

In **Fig.4.8** the pressure dependence of the minimum voltage for spontaneous breakdown and for laser-induced breakdown in  $SF_6$  are shown. Only at lower  $pd$ -values a significant difference between spontaneous and laser-induced breakdown is obtained.

**Figure 4.9** shows the corresponding pressure dependence of the measured prebreakdown current waveforms in  $SF_6$  for an approximately constant number of initial electrons  $N_0$  and approximately constant  $E/p$  of  $9 \cdot 10^{-4}$  kV/cm Pa.

From the experimental data the primary electron transit time of  $30$  ns was found to be independent of the above parameters in the range  $1.3 \cdot 10^3$  Pa  $< p < 2 \cdot 10^4$  Pa (for the considered conditions), as was also found by Verhaart<sup>21</sup>, though in contrast to the data by Wen<sup>20</sup> and Satoh et al.<sup>40</sup>. Above  $4 \cdot 10^4$  Pa the electron transit time decreases to approximately  $T_e = 6$  ns for atmospheric  $SF_6$ .

From Fig.4.6a (current for different sizes of emitting cathode area  $A$  from which the initial electrons are released) we conclude that increasing the initial electron density results in a shorter time to first current maximum.

From Fig.4.7 (different values of the applied field  $E$ ) we conclude that a slight increase in applied field (just below the static breakdown field strength) results in a significant reduction of the time-to-breakdown for laser-induced breakdown in  $SF_6$ .

From Fig.4.9 (different values of pressure  $p$ , and approximately constant number of initial electrons  $N_0$  and  $E/p$ ) we conclude that the electron transit time is independent of pressure.

For Townsend discharges Koppitz<sup>83</sup> showed that in nitrogen at low overvoltages nearly one dimensional discharges without radial constriction were possible. This is in agreement with the 2-D model outcomes (not shown here) for nitrogen and dry air in which a homogeneous (instead of gaussian) electron distribution with cathode emitting area  $A > 0.03 \text{ cm}^2$  was assumed. No significant radial development was observed. Under these conditions a 1-D model sufficiently describes the discharge phenomena.

And in general we conclude:

For diffusion in case of avalanches we observe local growth centers for which there can be different explanations and a  $T_e$  effect is possible (see section 4.3.2.2).

For diffusion in case of streamers a fluid description is appropriate.

### 4.3 Streamers and transition to breakdown

#### 4.3.1 Streamers in nitrogen in uniform applied fields

##### Experimental observations

##### A study of streamer formation in nitrogen<sup>11</sup>

Results for a uniform applied field with space charge field distortion are presented. Processes responsible for streamer formation will be discussed.

**Figs.4.10** and **4.11** show

- typical, measured series of subsequent prebreakdown currents (on a linear- and log-scale)
  - sequence of ICCD images
- in atmospheric nitrogen for an illuminated cathode area  $A$  of  $0.2 \text{ cm}^2$  respectively  $0.5 \text{ cm}^2$ , from which the initial electrons are released.

After each breakdown the conditions are modified in which the total number of electrons  $N_0$  stays approximately constant but the distribution is modified by the preceding breakdown.

This results in a modified waveform and time-to-breakdown, as can be seen from series  $a$  through  $d$  respectively  $a$  through  $h$ .

The reproducibility of such a sequence of waveforms of subsequent avalanches at high  $N_0$  ( $N_0 > 10^8$ ) was quite good.

From these figures we observe successive electron avalanches are more clearly distinguishable for larger illuminated cathode areas. In earlier work<sup>19</sup> the first avalanche current peak was observed to broaden due to space charge effects. Such "peak broadening" is typical for the streamer initiated gas-breakdown. "Peak broadening" is not observed<sup>6</sup> for Townsend-like, avalanche induced, gas-breakdown!

On the horizontal axes the time is normalized to the electron transit time in a uniform field  $T_e$ . From the 2-D model simulation  $T_e = 68 \text{ ns}$  was found. From our experimental data a primary electron transit time of  $65 \text{ ns}$  to  $70 \text{ ns}$  was found for the considered conditions. The experimental variations are due to differences in the space charge enhanced electron motion which depends critically on the initial electron number.

ICCD image  $a$  for  $A = 0.2 \text{ cm}^2$  in Fig.4.10 shows: the primary avalanche's transit and arrival at the anode.

Images  $b$  through  $d$  show: the subsequent formation of a cathode directed streamer (CDS) in the mid-gap enhanced field region, initiated by "delayed electrons" residing in this region.

In nitrogen, gas phase photoionization is the predominant source for these delayed electrons. Fig.4.11 (images  $a$  through  $h$ ) shows a similar behavior, now for an illuminated cathode area



of  $0.5 \text{ cm}^2$ . The optical activity in the ICCD images in both figures is shown on a linear (left) and logarithmic (right) intensity scale presentation.

The optical activity and (in the same time span) electrical activity corresponding with the avalanche generations crossing the gap from cathode to anode can be observed. From the value of the maximum photon count per pixel the optical activity was observed to stay approximately constant during the avalanche transition from cathode to anode and during the formation of the cathode directed streamer (images *a* and *b* in Fig.4.11). The exponential charge growth observed electrically corresponds to an increase in the number of active regions. Upon the initiation of the cathode directed streamer the optical activity becomes rather intense (images *c* through *h* in Fig.4.11).

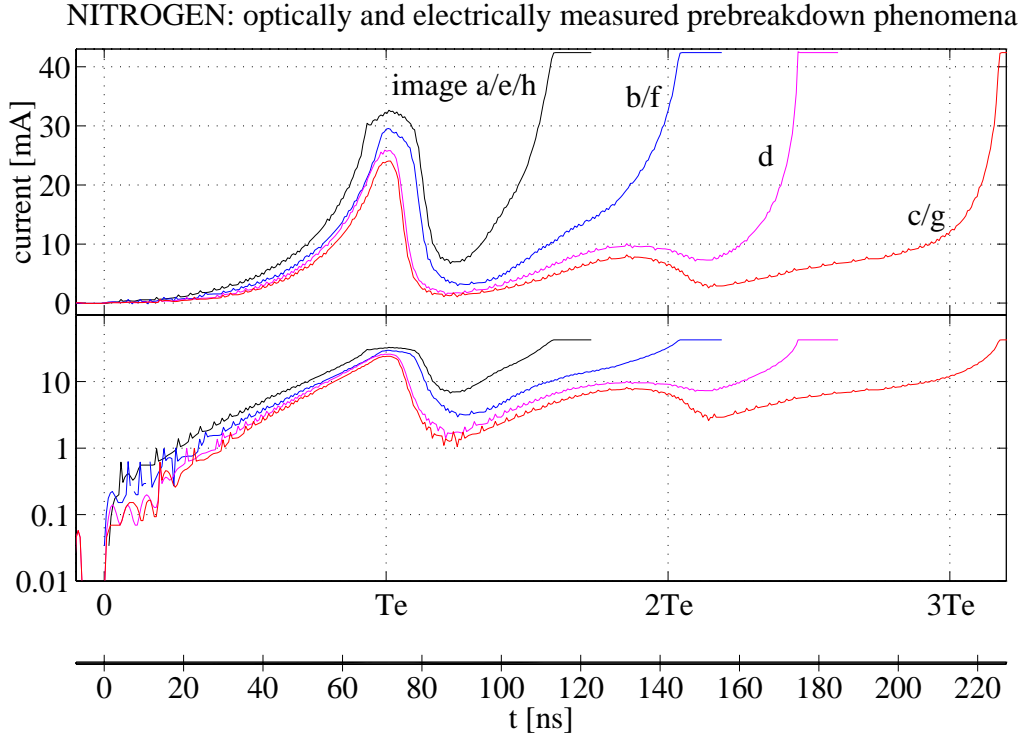
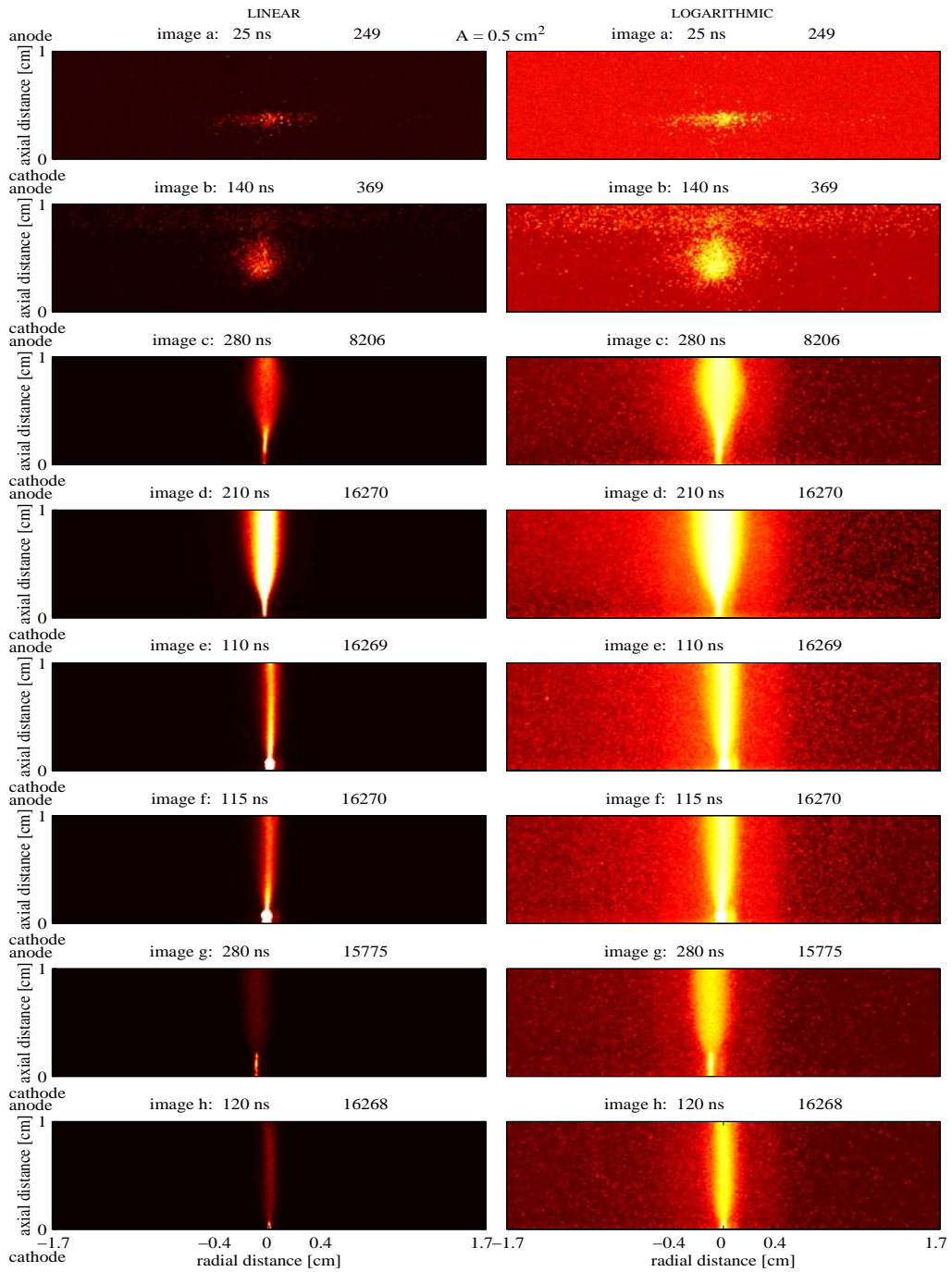


**Fig.4.11** Measured current waveforms ( $N_0=2 \cdot 10^8$ ,  $T_e=70 \text{ ns}$ ) and sequence of ICCD camera images of a laser-induced avalanche and its transition to a streamer. The initial electrons are released at  $t=0$  from the cathode (bottom) region around  $x=0$  ( $-0.4 \text{ cm} < x < 0.4 \text{ cm}$ ). Gate-shutter time of ICCD is  $5 \text{ ns}$ . Linear (left) and logarithmic (right) intensity scale. Conditions: atmospheric nitrogen  $E=30.5 \text{ kV/cm}$ , gap= $1 \text{ cm}$ .



### Simulation results

Similar to the measurements of Figs.4.10 and 4.11, **Figure 4.12** shows simulated avalanche current waveforms and the density distributions of electrons, positive ions and excited species and resulting electrical field at various time instances. The 2-D hydrodynamic model provides a good description of the external current.

For the simulation shown in Fig.4.12 we found the following classification, also summarized in **Figure 4.13** and **Table 4.1**:

In the early stages ( $0 < t < t_{space\ charge}=25\ ns$ ), the avalanche is nearly symmetric around the center (of mass) and disc-shaped and the current growth is exponential. Note: Comparison of the electron density in the early avalanche phase at  $5\ ns < t < 60\ ns$  in Fig.4.12 to the situation in Fig.4.3 with lower  $N_0$  shows the electron avalanche is much more confined to a small axial distance in the absence of considerable space charge.

For electron numbers between  $4.5 \cdot 10^8$  and  $10^9$  exponential growth is reduced due to a reduced overall ionization in the presence of space charge for  $t_{space\ charge} < t < t_{ADS}=50\ ns$ . At  $t_{ADS} < t < T_e=65\ ns$ , an ADS forms which propagates to the anode at speeds in excess of the electron drift velocity in a uniform field. At the location of the front  $E/E_0=1.3$ , and  $N_e(50\ ns)=3 \cdot 10^9\ electrons$ . Current growth is over-exponential. For  $T_e < t < 70\ ns$  the current stays constant, as was also observed in the measured current waveforms in Figs.4.11 and 4.12. At  $t=72\ ns$  delayed electrons result from gas phase photoionization starting near the avalanche head. During  $T_e < t < t_{CDS}=93\ ns$  a CDS forms (sometimes called the slow cathode directed streamer phase). At the location of the front  $E/E_0=1$ , and  $N_e(65\ ns)=1.1 \cdot 10^{10}\ electrons$ . This gives rise to an ionizing wave moving towards the cathode; the CDS. For  $t_{CDS} < t < t_{bd}=111.2\ ns$  the CDS propagates. During the propagation of the CDS a second ADS forms at  $t=110.5\ ns$ . For  $t_{ADS(2)} < t < t_{bd}$  at the location of the ADS front  $E/E_0=2.2$ , at a density of  $8.5 \cdot 10^{14}\ electrons/cm^3$  and at this time moment  $N_e=3 \cdot 10^{10}\ electrons$  and at the location of the CDS head  $E/E_0=12.2$ , at a density of  $3 \cdot 10^{15}\ electrons/cm^3$ . Once a second ADS has formed, for times  $t > t_{ADS(2)}$ , current growth is over-exponential.

The streamer radii are determined from the halfwidth value of the logarithmic field distribution.

For the streamer radii we find

$$\begin{aligned} r_{CDS} &= 0.5\ mm \\ r_{ADS} &= 0.5\ mm \end{aligned}$$

In nitrogen, gas phase photoionization is the predominant source for the "delayed electrons" which initiate the streamers. Both "cathode" and "anode directed streamers" occur.

From the electron distribution and the E-field plot at  $t=65\ ns$  in Fig.4.12 we can clearly observe the enhanced ionization in the space charge modified electric field at the avalanche head.

The optical experiments with high time-resolution have shown that, as soon as the primary avalanche reaches the anode, a cathode directed streamer forms in the mid-gap enhanced

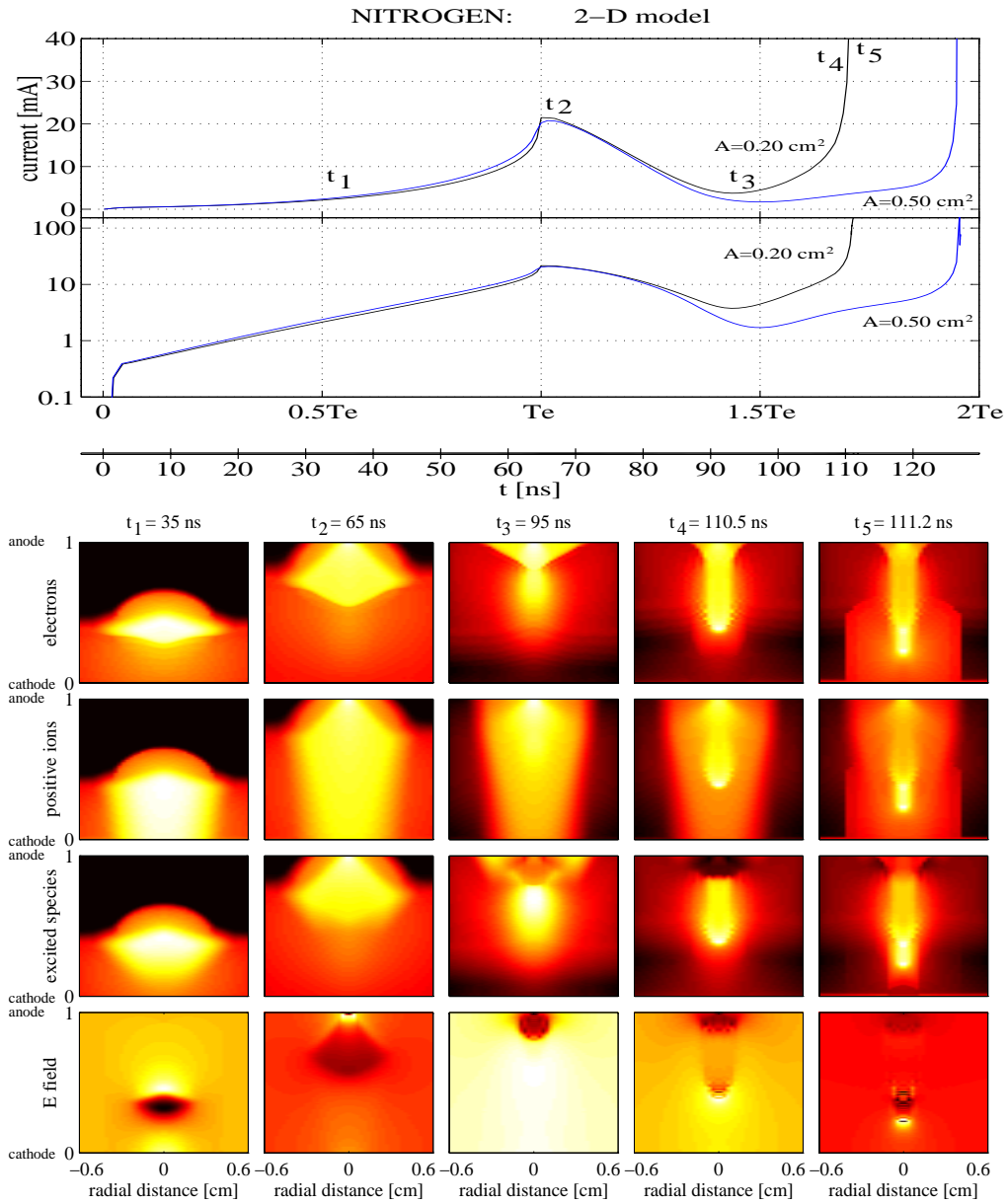


**Fig.4.12** Simulated current waveform ( $N_0=2 \cdot 10^8$ ,  $T_e=65-68 \text{ ns}$ ,  $A=0.20 / 0.50 \text{ cm}^2$ ). Electron, positive ion and excited species density and resulting electrical field at various time instances. Conditions: atmospheric nitrogen  $E=30.5 \text{ kV/cm}$ , gap= $1 \text{ cm}$ .

field region as a result of delayed electrons residing there<sup>6</sup>. This can be seen from the experimental observations shown in Fig.4.11 image *b* (on the right) at  $t=140$  ns as well as from the simulated excited species density in Fig.4.12 at  $t=95$  ns.

In the absence of considerable space charge for times up to  $t=T_e$  current growth is exponential and no ADS forms during the primary avalanche's transit. After the primary avalanche reaches the anode at first a CDS forms and thereafter an ADS forms.

Figure 4.13 and Table 4.1 summarize the development stages of streamer initiated dielectric breakdown in atmospheric nitrogen.

### Discussion

From the reduced current growth around the first current maximum it is clear that space charge effects occur at the conditions presented in both Figs.4.10 and 4.11. As was shown earlier<sup>19</sup> the current waveform strongly depends on the initial conditions.

Reflection of the  $N_2$ -laser beam at the cathode and the anode surface instantaneously releases small numbers of additional electrons over a broader cathode region outside the directly illuminated cathode area *A*. These electrons also form small avalanches and this corresponds to the large spread in radial direction during the primary avalanche's transit in the observed optical distribution, as can be seen in Fig.4.10 image *a* on the right (logarithmic intensity scale presentation).

Space charge effects form, later in time, a significant radial field which also results in a spread in radial direction for small illuminated cathode area *A* as is shown by Fig.4.12 at  $t=35$  ns. Diffusion alone cannot account for the relatively large radial expansion of the observed discharge activity as is concluded from 2-D model simulations.

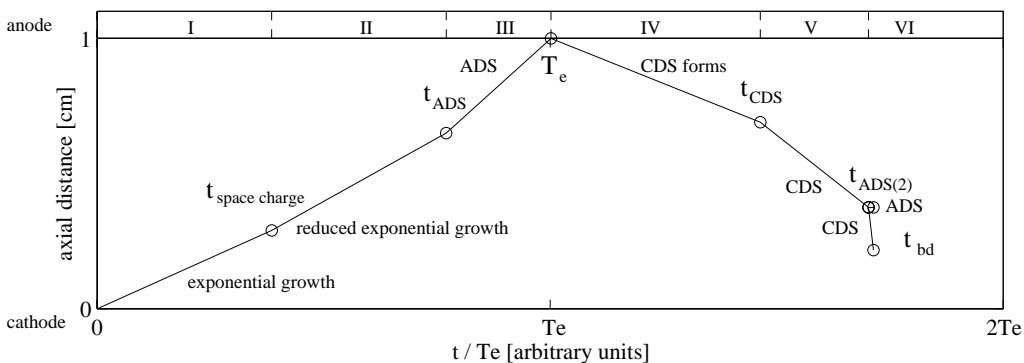


**Fig.4.13** Development stages of streamer initiated dielectric breakdown in atmospheric nitrogen.

Conditions: atmospheric nitrogen  $E=30.5$  kV/cm, gap=1 cm.

**Table 4.1** Development stages of streamer initiated dielectric breakdown in atmospheric nitrogen.

Stage (time interval)	$i(t)$	$E/E_0$	$N_e$ [electrons]	development
I $0 < t < t_{\text{space charge}}$	exponential growth	$\approx 1$	$< 4.5 \cdot 10^8$	in the early stages, the avalanche is nearly symmetric around the center (of mass) and is disc shaped
II $t_{\text{space charge}} < t < t_{\text{ADS}}$	reduced exponential growth	$> 1.1$	at $t_{\text{space charge}}$ $7.5 \cdot 10^8$	reduced overall ionization in the presence of space charge
III $t_{\text{ADS}} < t < T_e$	over- exponential growth	$> 1.3$	at $t_{\text{ADS}}$ $3 \cdot 10^9$	an ADS forms, which propagates to the anode at speeds in excess of the electron drift velocity in a uniform field
IV $T_e < t < t_{\text{CDS}}$	constant or decreasing	1	at $T_e$ $1.1 \cdot 10^{10}$	a CDS forms, due to "delayed electrons" residing in the mid-gap enhanced field
V $t_{\text{CDS}} < t < t_{\text{bd}}$	exponential growth	$> 1$	at $t_{\text{CDS}}$ $9 \cdot 10^9$	CDS propagation
VI $t_{\text{ADS}(2)} < t < t_{\text{bd}}$	over- exponential growth	ADS(2) 2.2 CDS 12.2	at $t_{\text{ADS}(2)}$ $3 \cdot 10^{10}$	during the propagation of the CDS a second ADS forms

The measured and simulated reduced exponential (current) growth is an inherent property of avalanches in the presence of space charge, and is due to non-uniform fields.

The reduced (current) growth results from the space charge field, which significantly reduces ionization growth at the place at which we have the highest charge concentration. At the boundaries of the space charge, ionization increases in the modified field. The overall ionization coefficient over the whole avalanche is hereby reduced. This effect sets in once the space charge field attains a value comparable to 5% of the applied field. From this point on the ionization coefficient  $\alpha$  becomes dependent on the charge multiplication, i.e. time and space dependent. Our results agree with earlier observations made by Saxe<sup>84</sup>, Tholl<sup>85,93</sup>, Allen and Phillips<sup>86</sup>, Wagner<sup>87,88</sup>, Koppitz<sup>83,89</sup>, Doran<sup>90</sup>, Haydon<sup>91</sup>, Cavenor and Meyer<sup>92</sup>, Chalmers et al.<sup>94</sup> and Bayle et al.<sup>95</sup>.

Under the influence of strong space charge the field becomes non-uniform. Recent work by Petcheraks<sup>58</sup> for non-uniform fields under the influence of space charge shows that this results in a lower streamer constant  $K$  for the streamer breakdown criterion (in the order of 10 instead of 18), corresponding to a reduced overall ionization coefficient under such conditions. This mechanism is supported by our observations.

The reduced overall ionization coefficient results in a large reduction of the ionization growth and thereby slightly reduces exponential avalanche current growth for nitrogen. Due to a larger space charge field, caused by the presence of negative ions, the effect of a change in the effective ionization coefficient is more pronounced in dry air. This more pronounced effect for dry air will be shown in Section 4.3.2.

### 4.3.2 Streamers in dry air in uniform applied fields

#### 4.3.2.1 Prebreakdown phenomena

##### Experimental observations

##### A study of streamer formation in dry air<sup>12</sup>

Results for a uniform applied field with space charge field distortion are presented. Processes responsible for streamer formation will be discussed.

**Fig.4.14** shows

- typical, measured prebreakdown currents (on a linear- and log-scale)
- corresponding photomultiplier output signals (PM1 and PM2) representing time-resolved space integrated optical activity in the gap
- sequence of ICCD images

in atmospheric air for different sizes of the area  $A$  from which the initial electrons are released.

The waveform change in the primary electron avalanche demonstrates the presence of space charge: with decreasing emitting cathode area the initial electron density increases which results in a change in the current waveform shape and the resulting time-to-breakdown.

For small emitting cathode areas ( $A < 0.13 \text{ cm}^2$ ) the current shows a transition point. From this point on in time the current growth is still exponential but with another exponent as if based on another effective ionization coefficient. With increasing emitting cathode area  $A$  the time-to-breakdown increases by almost a factor two.

The corresponding time-resolved space integrated optical activity upon streamer initiation is seen from the photomultiplier signals PM1 and PM2 (the first peak is the  $N_2$ -laser pulse).

ICCD images  $a$  through  $d$  for  $A = 0.008 \text{ cm}^2$  show:

the primary avalanche's transit and arrival at the anode.

Image  $e$  shows:

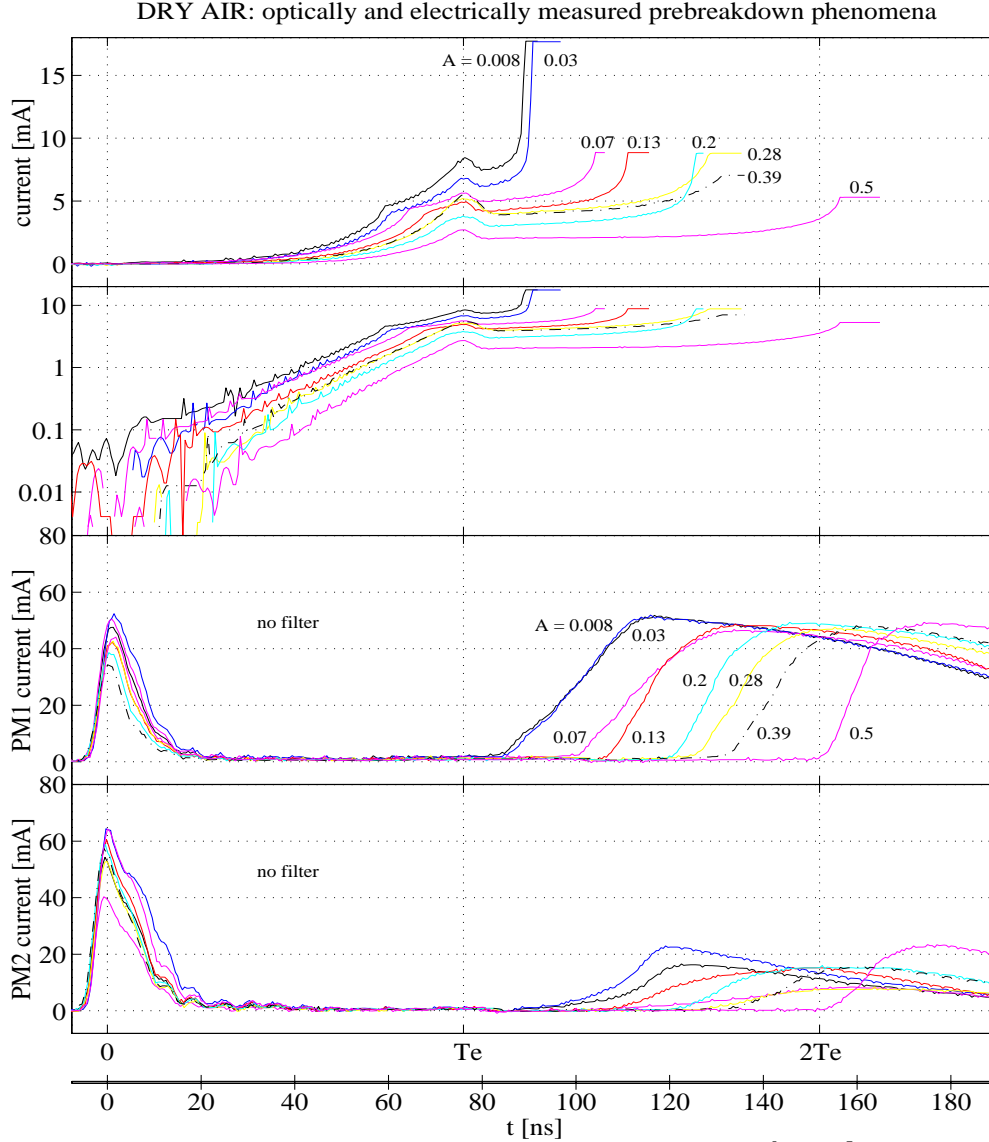
the subsequent cathode directed streamer (CDS) formation in the mid-gap enhanced field region, initiated by "delayed electrons" residing in this region.

Images  $f$  through  $h$  show:

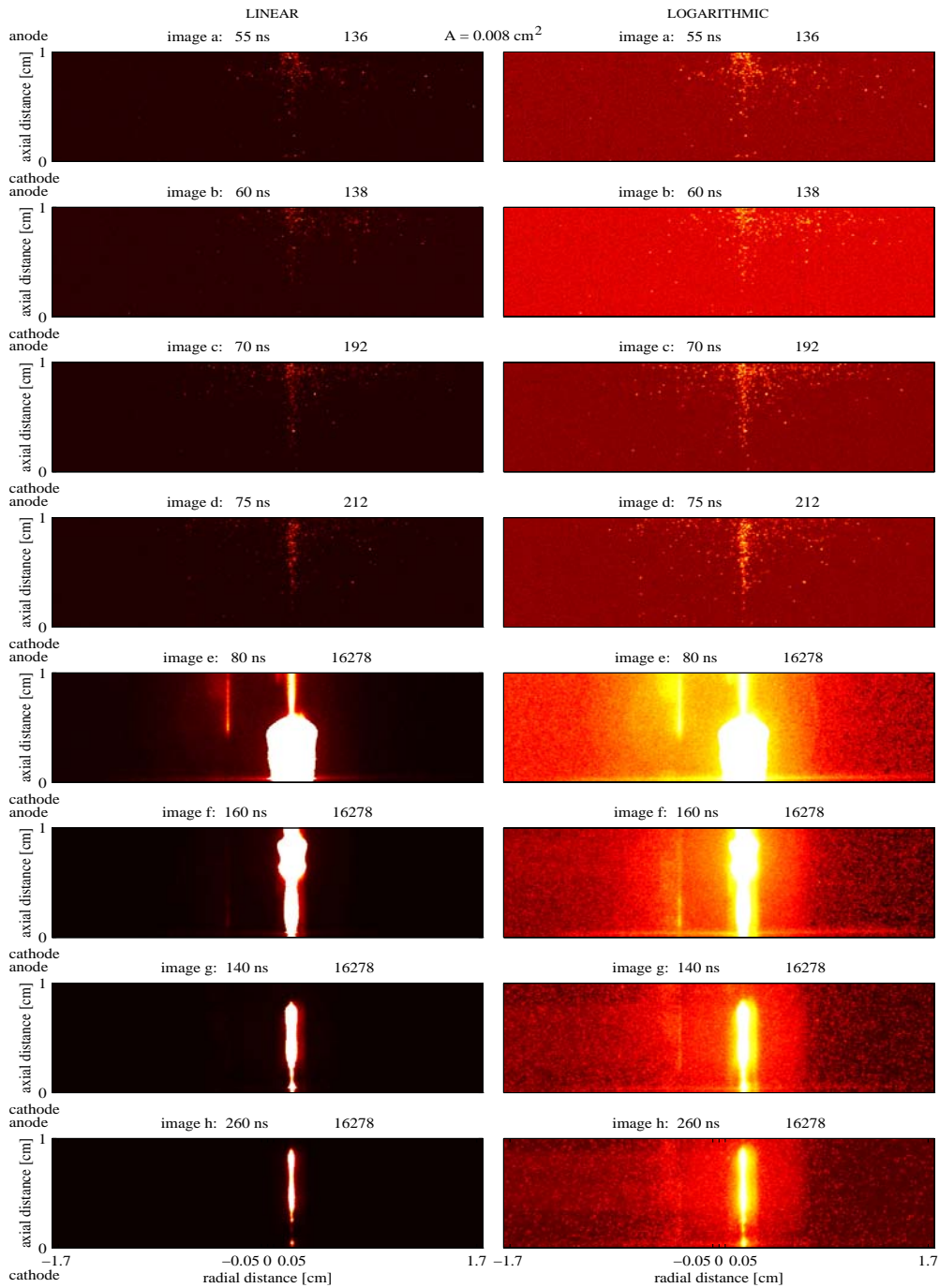
the anode directed streamer (ADS) formation, and CDS and ADS propagation.

In dry air, gas phase photoionization and detachment are the predominant sources for the delayed electrons as will be illustrated later with model simulations.

From the value of the maximum photon count per pixel it can be seen that the optical activity at first increases during the primary electron avalanche's transition towards the anode. Thereafter it still shows weak optical activity spread out over the whole gap volume. Upon the initiation of the cathode directed streamer the activity is rather intense.



**Fig.4.14** Measured current waveforms for different emitting areas ( $N_0=2.8 \cdot 10^5 - 4.4 \cdot 10^7$ ,  $T_e=73-78\text{ns}$ ). Emitting cathode area  $A=0.008 / 0.03 / 0.07 / 0.13 / 0.2 / 0.28 / 0.39 / 0.5 \text{ cm}^2$ . Photomultiplier output signals (PM1 and PM2), and sequence of ICCD camera images of a laser-induced avalanche and its transition to a streamer. The initial electrons are released at  $t=0$  from the cathode (bottom) region  $A$  around  $x=0$ . Gate-shutter time of ICCD is  $5 \text{ ns}$ . Linear (left) and logarithmic (right) intensity scale. Conditions: atmospheric air  $E=30 \text{ kV/cm}$ , gap= $1 \text{ cm}$ .



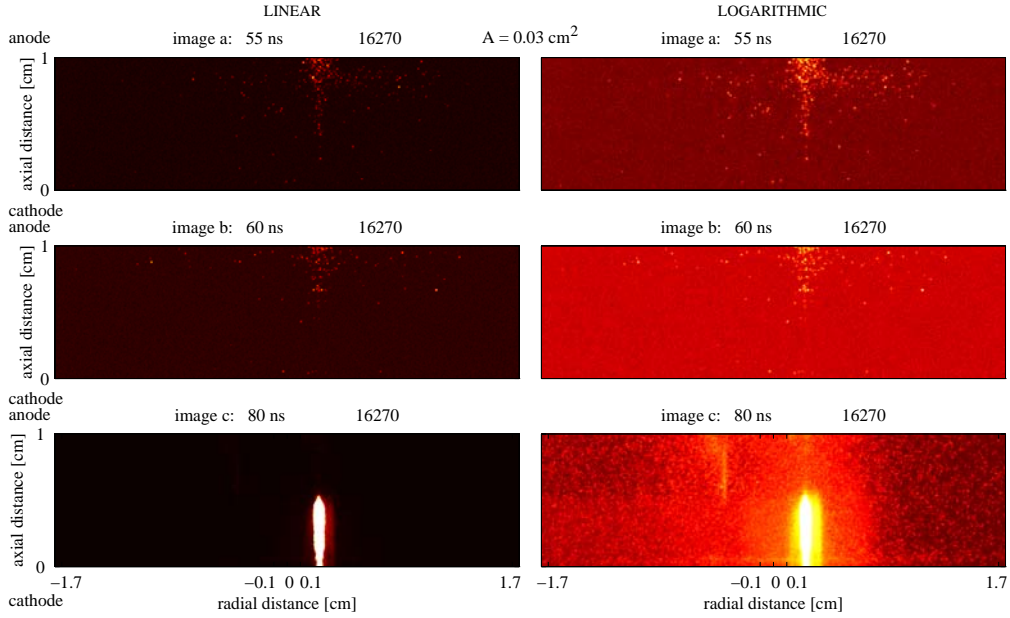


**Fig.4.14** (continued) ICCD camera images of a laser-induced avalanche and its transition to a streamer. The initial electrons are released at  $t=0$  from the cathode (bottom) region  $A$  around  $x=0$ . Linear (left) and logarithmic (right) intensity scale. Gate-shutter time of ICCD is  $5\text{ ns}$ .

In the ICCD images a spread in radial direction similar as for  $N_2$  is observed during the primary avalanche's transit. This is due to the artifact of the experimental setup described in Section 4.3.1, whereby small numbers of additional electrons are released over a broader cathode region.

At later times the radial expansion of the discharge activity resulted from a significant radial field, as was tested with the 2-D model. Diffusion did not account for this effect.

At the transition point in the current for  $t < T_e$ , space charge effects set in, corresponding to the ceasing of the radial expansion of the observed discharge activity, as was found from the ICCD images. From the ICCD image the pinching of the discharge activity upon streamer initiation can clearly be seen.

For  $A > 0.20\text{ cm}^2$  the streamer formation results from a broader volume of optical activity in which delayed electrons are present (ICCD images  $a$  through  $c$  for  $A = 0.39\text{ cm}^2$ ).



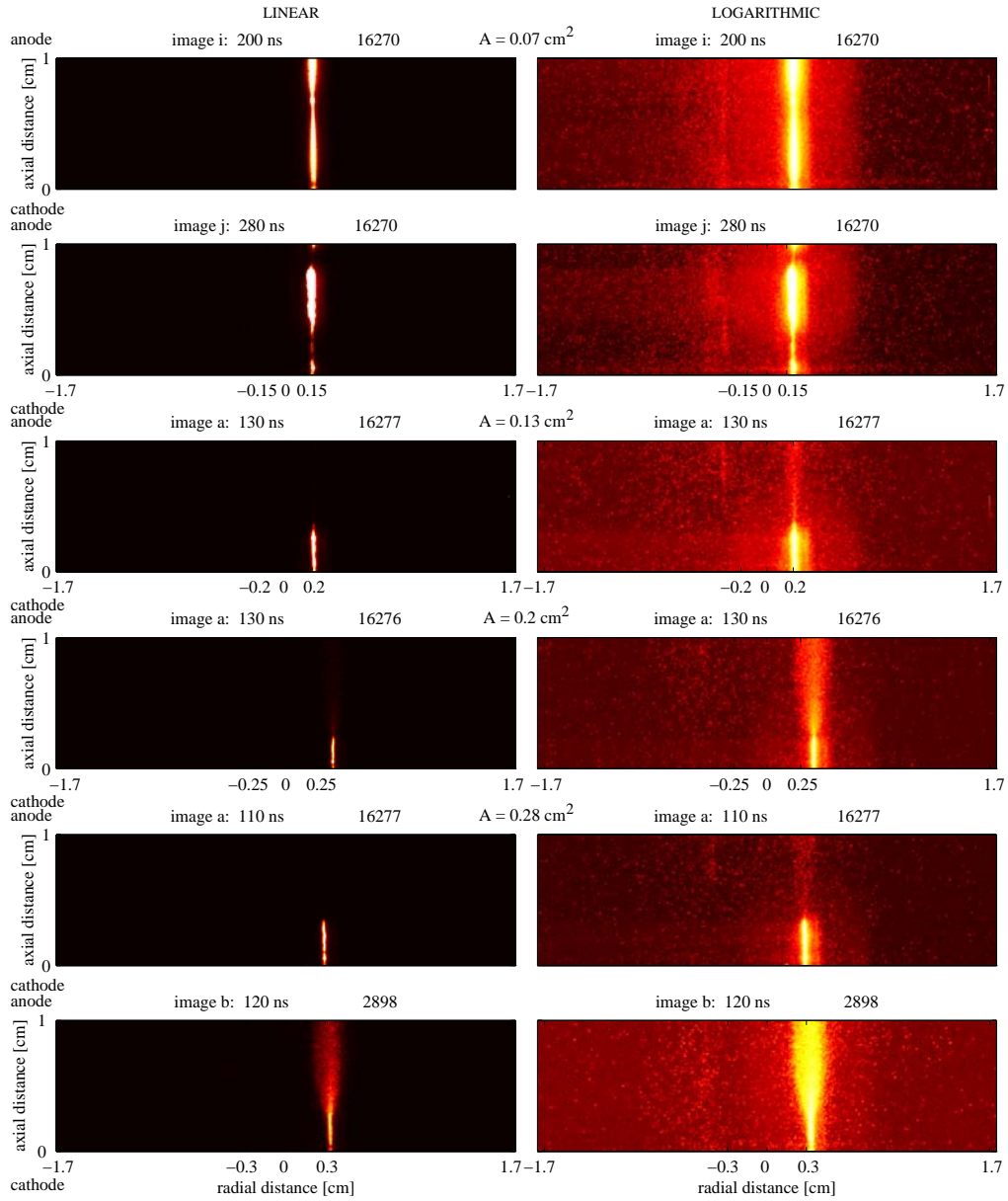
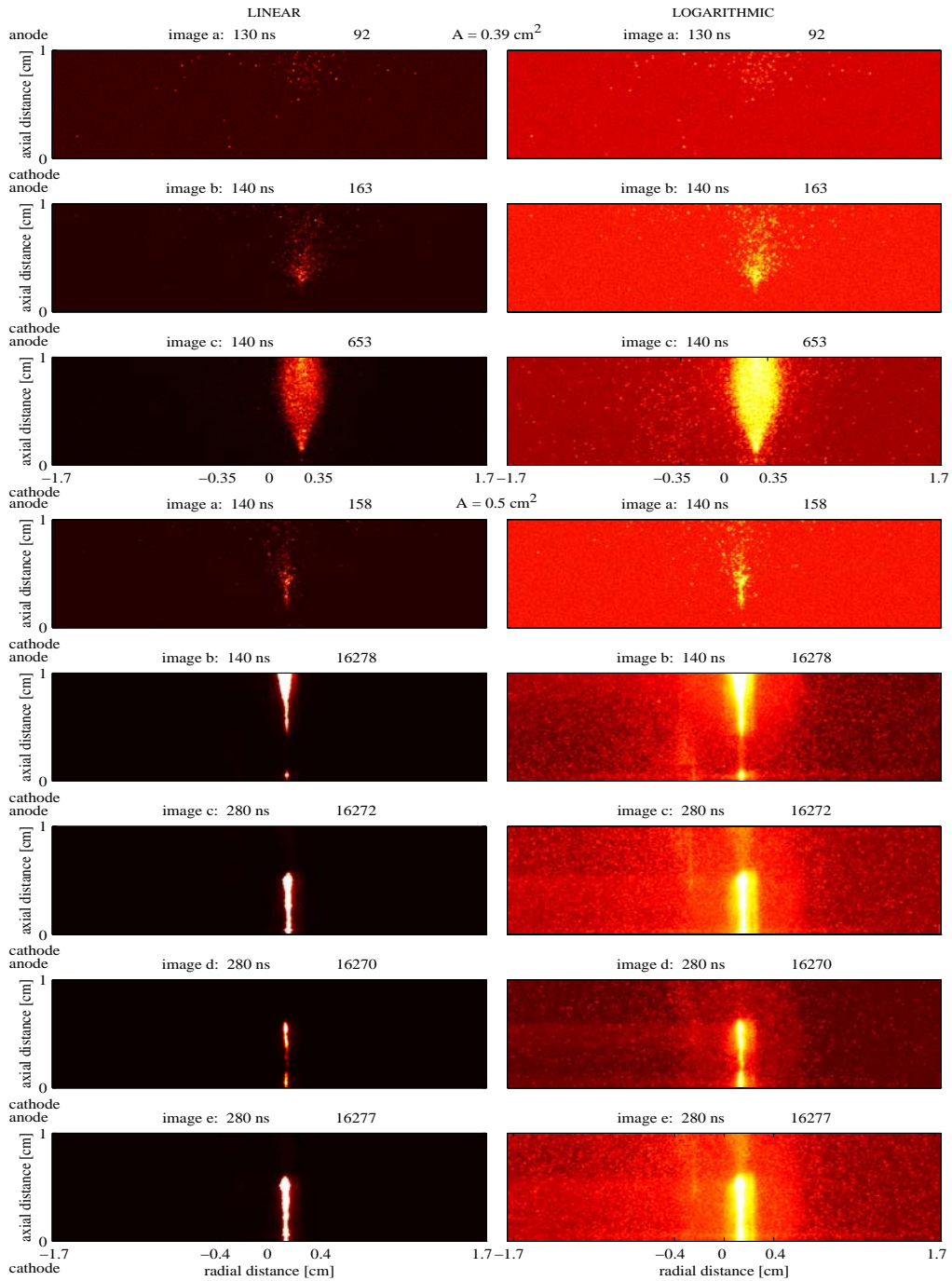


**Fig.4.14** (continued) ICCD camera images of a laser-induced avalanche and its transition to a streamer. The initial electrons are released at  $t=0$  from the cathode (bottom) region  $A$  around  $x=0$ . Linear (left) and logarithmic (right) intensity scale.  $5 \text{ ns}$  ICCD camera gate-shutter time.



The large delay time between the first avalanche and streamer breakdown formation, and the weak optical activity during this time suggests that cathode photoelectron emission and gas phase photoionization do not play a dominant role in the streamer formation for these conditions. On the other hand, in addition to enhanced ionization in the space charge modified electrical field, gas phase photoionization is vital for streamer propagation once the streamer has formed.

**Figure 4.15** shows an ICCD image at the moment at which the CDS head moves towards and almost reaches the cathode. In front of the anode the second ADS, which has formed out of the ionizing electron wave towards the positive anode, can be distinguished. During the movement of the ADS ionizing front also a second CDS forms due to space charge effects.

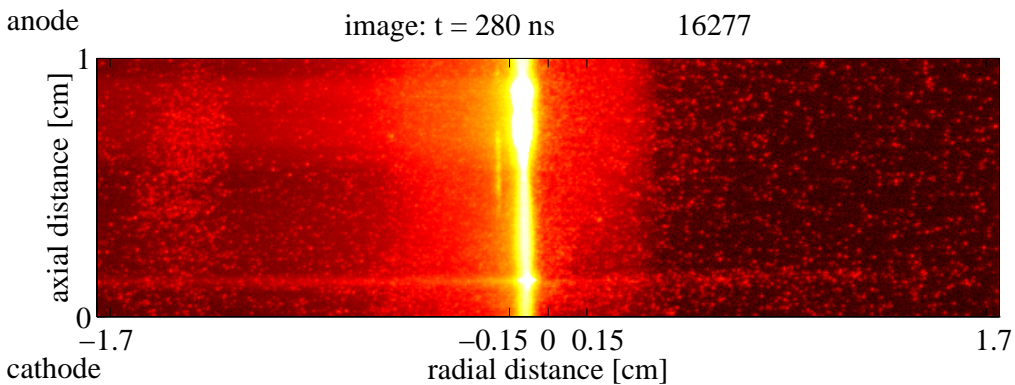


**Fig.4.15** ICCD camera image of a laser-induced streamer breakdown. The initial electrons are released from the cathode (bottom) at  $t=0$  indicated by the region around  $x=0$  ( $-0.15 \text{ cm} < x < 0.15 \text{ cm}$ ). ( $N_0=4 \cdot 10^7$ ,  $T_e=28 \text{ ns}$ ). Logarithmic intensity scale. Gate-shutter time of ICCD is  $5 \text{ ns}$ .  
Conditions: atmospheric air  $E=30.0 \text{ kV/cm}$ , gap= $1 \text{ cm}$ .

### Simulation results

The simulated electron, positive ion, stable and unstable negative ion and excited species density and resulting electrical field at various time instances are shown in **Fig.4.16** together with the corresponding simulated discharge current. In the simulated avalanche current waveform successive electron avalanches cannot be distinguished. On the horizontal axes the time is normalized to the electron transit time in a uniform field  $T_e$ . From the 2-D model simulation  $T_e=54 \text{ ns}$  is found. The first current maximum shows up after the primary electron avalanche transit time  $T_e$ .

The species density images show the primary avalanche's transition ( $5 \text{ ns} < t < 50 \text{ ns}$ ), arrival at the anode ( $t=60 \text{ ns}$ ) and the subsequent cathode directed streamer formation in the mid-gap enhanced field region ( $t>70 \text{ ns}$ ), initiated by delayed electrons in this region. In dry air, detachment and gas phase photoionization are the predominant sources for these delayed electrons. This can, for example, be deduced from the region of enhanced field together with the plots of the unstable negative ion and the excited species densities at  $t=70 \text{ ns}$  and  $75 \text{ ns}$ . As the CDS progresses towards the cathode the streamer becomes narrower as can be seen from the electron density and the total electrical field at  $t=75 \text{ ns}$  to  $79.5 \text{ ns}$ .

**Fig.4.17** shows similar results (also dry air,  $30 \text{ kV/cm}$ ,  $1 \text{ cm}$  gap), now for a larger number of initial electrons ( $N_0=4 \cdot 10^7$ ); the increased initial electron number results in a slightly faster gap transition, much more intense CDS development and therefore a much faster gas-breakdown at  $t_{bd}=59 \text{ ns}$  instead of  $79.5 \text{ ns}$ .

For the simulation shown in Fig.4.17 we found the following classification, also summarized in **Figure 4.18** and **Table 4.2**:

In the early stages ( $0 < t < t_{space \text{ charge}}=8 \text{ ns}$ ), the avalanche is nearly symmetric around the center (of mass) and disc-shaped and the current growth is exponential.

For electron numbers between  $1 \cdot 10^8$  and  $10^9$  exponential growth is reduced due to a reduced overall ionization in the presence of space charge for  $t_{space \text{ charge}} < t < t_{ADS}=35 \text{ ns}$ . At  $t=25 \text{ ns}$  a CDS forms. At the location of the front  $E/E_0=1.12$ , and at this moment in time  $N_e=7.4 \cdot 10^8 \text{ electrons}$ . At  $t=35 \text{ ns}$  an ADS forms. At the location of the CDS front  $E/E_0=1.2$ , and at the ADS front  $E/E_0=1.12$ , and at this moment  $N_e=2 \cdot 10^9 \text{ electrons}$ . Current growth is over-exponential. At  $t=52 \text{ ns}$  the ADS reaches the anode and the CDS starts to propagate towards the cathode. At the location of the streamer head  $E/E_0=1.4$ , and at the start of CDS propagation  $N_e=1.5 \cdot 10^{10} \text{ electrons}$ . During the propagation of the CDS a second ADS forms at  $t=55 \text{ ns}$ , at the location of the ADS front  $E/E_0=1$ , at a density of  $1.6 \cdot 10^{11} \text{ electrons/cm}^3$  and at this moment  $N_e=1.7 \cdot 10^{10} \text{ electrons}$  and at the location of the CDS head  $E/E_0=1.5$ , at a density of  $4.9 \cdot 10^{11} \text{ electrons/cm}^3$ .

Once a second ADS has formed, for times  $t > t_{ADS(2)}$ , current growth is over-exponential. During the propagation of the second ADS a second CDS forms at  $t=58.98 \text{ ns}$ , at the location of the CDS front  $E/E_0=8.2$ , at a density of  $3.7 \cdot 10^{17} \text{ electrons/cm}^3$ , at the location of the second ADS front  $E/E_0=1.05$ , at a density of  $2.5 \cdot 10^{11} \text{ electrons/cm}^3$ , at the location of the second CDS  $E/E_0=1.1$ , at a density of  $3.4 \cdot 10^{11} \text{ electrons/cm}^3$  and at this time moment  $N_e=2 \cdot 10^{10} \text{ electrons}$ .

For the streamer radii we find

$$\begin{aligned} r_{CDS} &= 0.3 \text{ mm} \\ r_{ADS} &= 0.5 \text{ mm} \end{aligned}$$

Comparison of Fig.4.14 and Figs.4.16 and 4.17 shows that the 2-D hydrodynamic model provides a good description of the external current, the avalanche-to-streamer transition and streamer initiated breakdown.

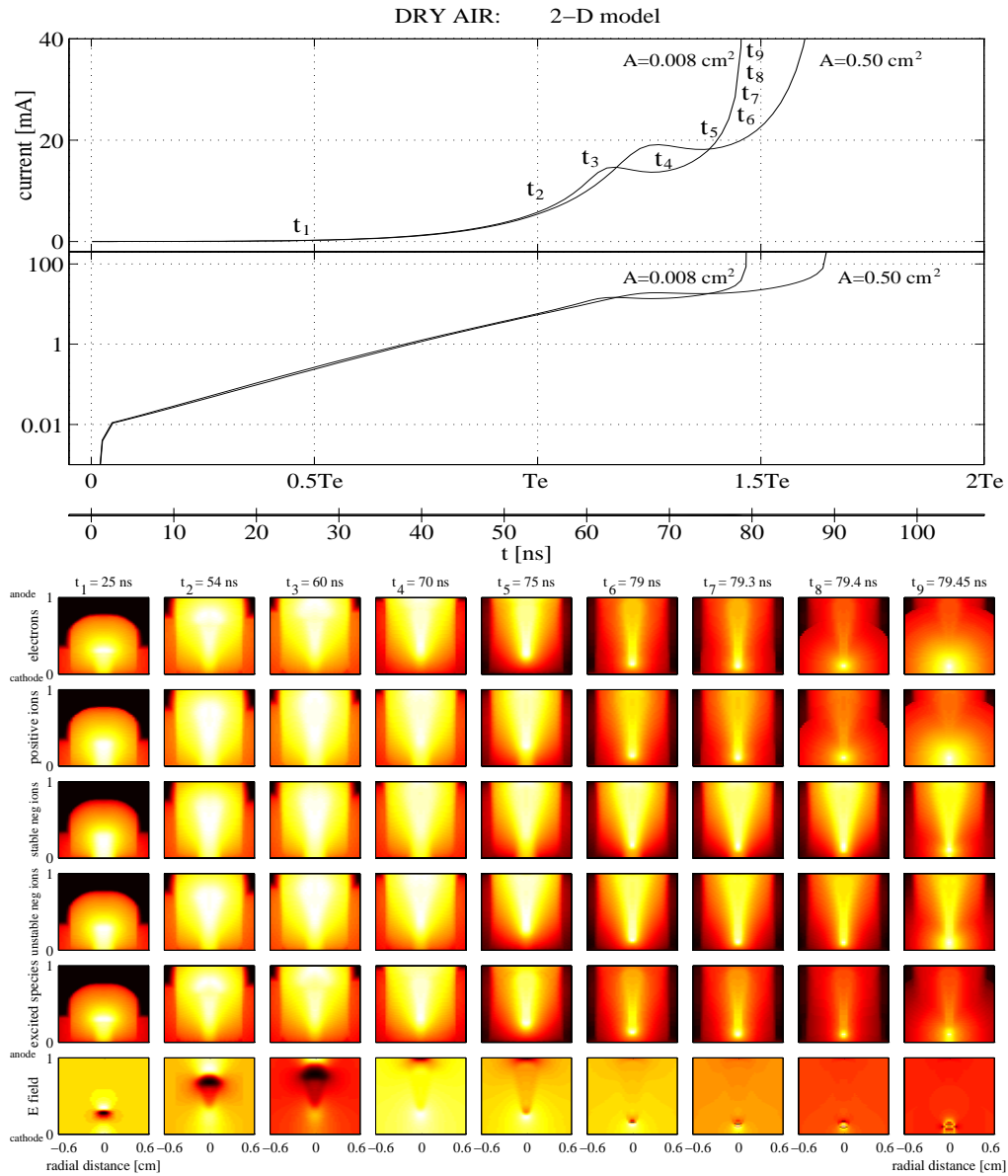


**Fig.4.16** Simulated current waveform ( $N_0=4 \cdot 10^6$ ,  $T_e=52-54 \text{ ns}$ ,  $A=0.008 / 0.5 \text{ cm}^2$ ).

Electron, positive ion, stable negative ion, unstable negative ion and excited species density and resulting electrical field at various time instances.

Conditions: atmospheric air  $E=30.0 \text{ kV/cm}$ ,  $\text{gap}=1 \text{ cm}$ .

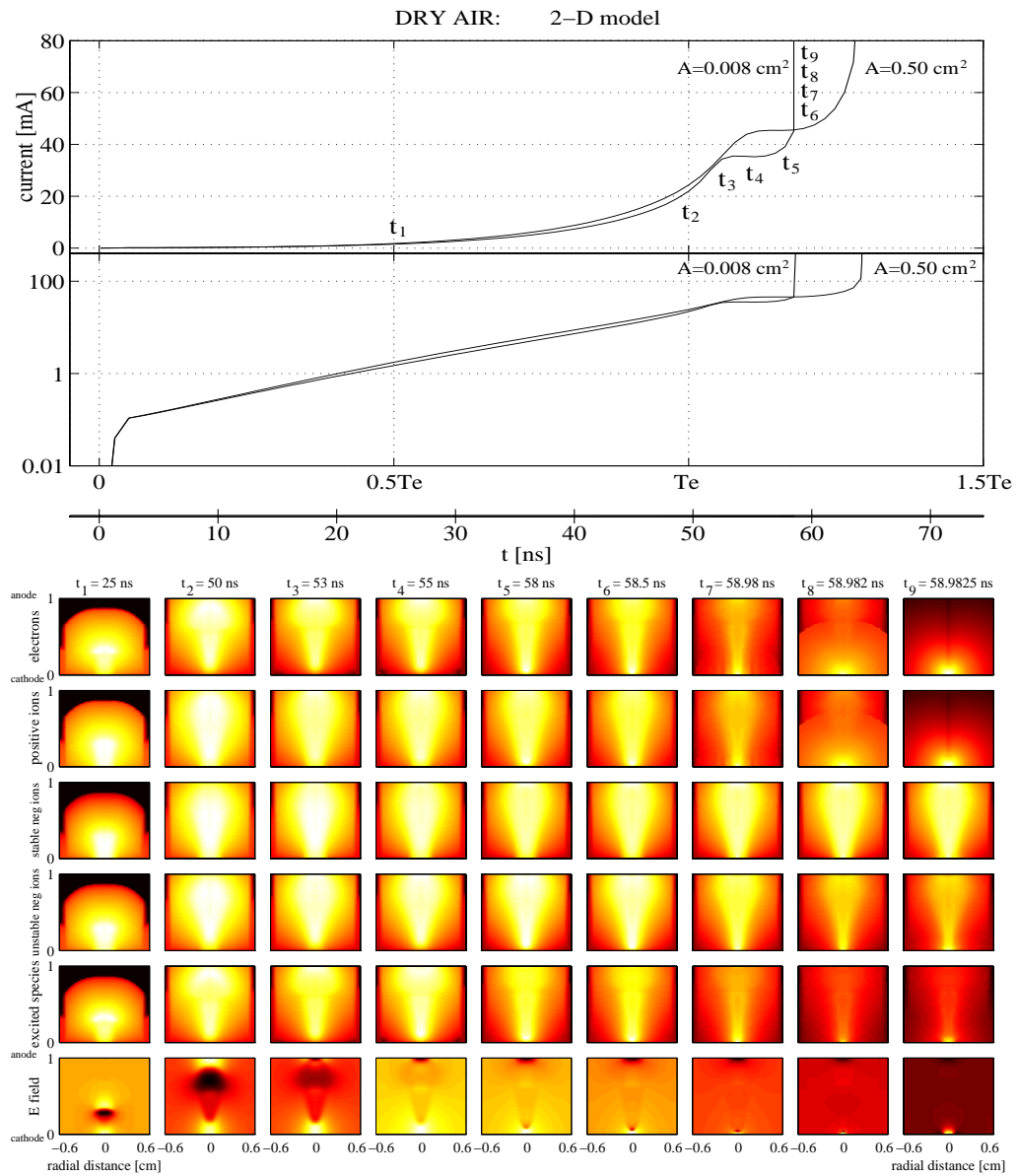


**Fig.4.17** Simulated current waveform ( $N_0=4 \cdot 10^7$ ,  $T_e=50-51 \text{ ns}$ ,  $A=0.008 / 0.5 \text{ cm}^2$ ).  
 Electron, positive ion, stable negative ion, unstable negative ion and excited species density and resulting electrical field at various time instances.  
 Conditions: atmospheric air  $E=30.0 \text{ kV/cm}$ , gap=1 cm.

For electron numbers between  $10^6$  and  $10^9$  exponential growth is reduced due to a lower overall ionization in the presence of space charge for  $t_{space\ charge} < t < t_{ADS}=35\ ns$ .

In the absence of considerable space charge for times up to  $t=T_e$  current growth is exponential and no ADS forms during the primary avalanche's transit. After the primary avalanche reaches the anode first a CDS streamer forms and thereafter an ADS forms.

Figure 4.18 and Table 4.2 summarize the development stages of streamer initiated dielectric breakdown in atmospheric dry air.

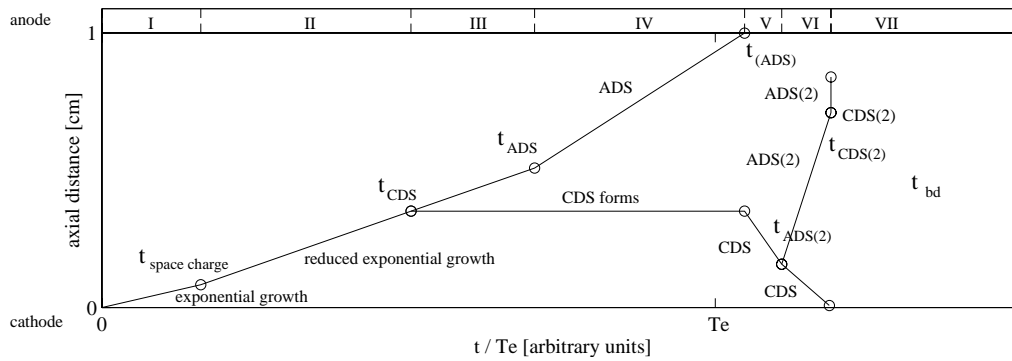


**Fig.4.18** Development stages of streamer initiated dielectric breakdown in atmospheric dry air.  
Conditions: atmospheric dry air  $E=30\ kV/cm$ , gap=1 cm.

**Table 4.2** Development stages of streamer initiated dielectric breakdown in dry air.

Stage (time interval)	$i(t)$	$E/E_0$	$N_e$ [electrons]	development
I $0 < t < t_{\text{space charge}}$	exponential growth	$\approx 1$	$< 1 \cdot 10^6$	in the early stages, the avalanche is nearly symmetric around the center (of mass) and is disc shaped
II $t_{\text{space charge}} < t < t_{\text{ADS}}$	reduced exponential growth	$> 1.05$	at $t_{\text{space charge}}$ $1 \cdot 10^8$	reduced overall ionization in the presence of space charge
III $t_{\text{CDS}} < t < t_{\text{ADS}}$	reduced exponential growth	1.12	at $t_{\text{CDS}}$ $7.4 \cdot 10^8$	in the space charge enhanced field a CDS forms
IV $t_{\text{ADS}} < t < t_{(\text{ADS})}$	over- exponential growth	CDS 1.2 ADS 1.12	at $t_{\text{ADS}}$ $2 \cdot 10^9$	an ADS forms, at the space charge enhanced field at the avalanche head
V $t_{(\text{ADS})} < t < t_{\text{bd}}$	decreasing or exponential growth	$> 1$	at $t_{(\text{ADS})}$ $1.5 \cdot 10^{10}$	CDS propagation
VI $t_{\text{ADS}(2)} < t < t_{\text{bd}}$	over- exponential growth	CDS 5 ADS(2) 1.06	at $t_{\text{ADS}(2)}$ $1.7 \cdot 10^{10}$	during the propagation of the CDS a second ADS forms
VII $t_{\text{CDS}(2)} < t < t_{\text{bd}}$	over- exponential growth	CDS >8 ADS(2) 1.05 CDS(2) 1.11	at $t_{\text{CDS}(2)}$ $3 \cdot 10^{14}$	during the propagation of the second ADS a second CDS forms

### 4.3.2.2 Time-to-breakdown

#### Prebreakdown phenomena in insulating gases; evaluation of the electron transit time and time-to-breakdown<sup>15</sup>

Results with regard to the electron transit time  $T_e$  and time-to-breakdown  $t_{bd}$  are discussed. It is shown how the time-to-breakdown is influenced by the applied field, the initial electron number and the pressure reduced field  $E/p$ .

Results for a uniform applied field including space charge field distortion are presented.

#### The influence of the applied field

**Figure 4.19** shows the simulated time-to-breakdown  $t_{bd}$  and the electron transit time  $T_e$  as a function of the applied field for nitrogen and dry air.

Shown are curves for initial electron numbers  $N_0$  of  $4 \cdot 10^6$  and  $4 \cdot 10^8$  electrons, corresponding to a (maximum) density of  $3 \cdot 10^9$  respectively  $2 \cdot 10^{11}$  electrons/cm<sup>3</sup>.

**Nitrogen:** Above  $E_{tr}=30.3$  kV/cm  $t_{bd}$  and  $T_e$  coincide and the gap breaks down within the first electron transit time resulting in a decrease in breakdown time. Below

$E_{min}=28.85$  kV/cm no breakdown is observed.

**Dry air:** For dry air the behavior is different: more gradually  $t_{bd}$  and  $T_e$  become equal, and above  $E_{tr}=36$  kV/cm the gap breaks down within the first electron transit time. An increase in the number of initial electrons by two orders of magnitude has only a moderate influence on the time-to-breakdown. Below  $E_{min}=26.7$  kV/cm no breakdown is observed. Also shown for both nitrogen and dry air are our measured values which correspond with the computer simulation results. The results in Fig.4.19 agree with literature data by Fletcher<sup>96</sup> in which formative time-lags required for breakdown in air are given as a function of applied field for different gap-widths.

#### The influence of the number of initial electrons

**Figure 4.20** shows the influence of the number of initial electrons on the simulated time-to-breakdown  $t_{bd}$  and the electron transit time  $T_e$  for an applied field of  $E=30$  kV/cm and  $E=30.5$  kV/cm respectively.

**Nitrogen:** Above  $N_{0,tr}=4.5 \cdot 10^8$  electrons  $t_{bd}$  and  $T_e$  coincide resulting in a decrease in  $t_{bd}$ , similar to the effect on the curves in Fig.4.19. Electron numbers exceeding this value enable streamer formation before the initial electron avalanche reaches the anode.

Below  $N_0=9 \cdot 10^7$  electrons no breakdown occurs at  $E=30$  kV/cm. Hence,  $N_{0,min}=9 \cdot 10^7$  is the critical minimum electron number at  $E=30$  kV/cm.

For  $E=30.5$  kV/cm no breakdown occurs below  $N_0=4 \cdot 10^7$  electrons. Hence,  $N_{0,min}=4 \cdot 10^7$  is the critical minimum electron number at  $E=30.5$  kV/cm.

**Dry air:** The influence of the initial electron number  $N_0$  for dry air shows a completely different pattern. Above  $N_0=2 \cdot 10^9$  electrons  $t_{bd}$  and  $T_e$  gradually coincide. Electron numbers above this value enable streamer formation before the initial electron avalanche reaches the anode.

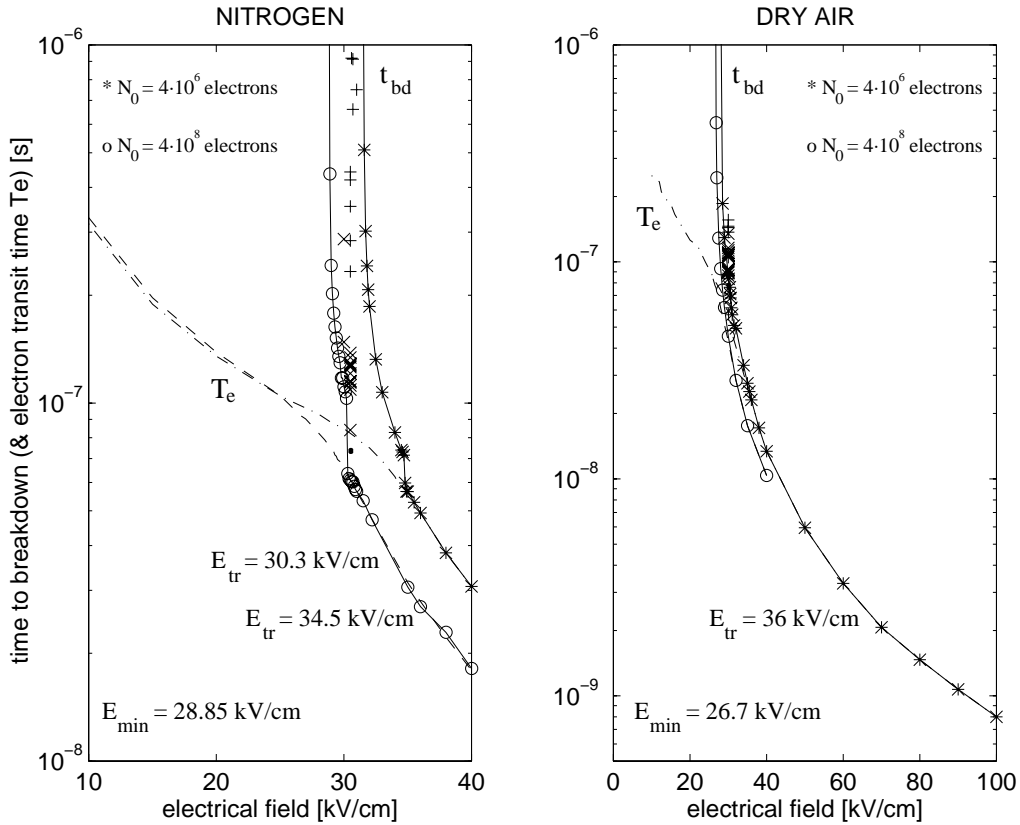


**Fig.4.19** Simulated time to breakdown  $t_{bd}$  (drawn line) and electron transit time  $T_e$  (dashed line) as a function of applied field  $E$ .

Measured values:	$N_2$	$t_{bd}$	+: $4 \cdot 10^7$ electrons	x: $2 \cdot 10^8$ electrons	•: $T_e$
	dry air	$t_{bd}$	+: $4 \cdot 10^6$ electrons	x: $4 \cdot 10^7$ electrons	•: $T_e$
Simulated values:		$t_{bd}$	*: $4 \cdot 10^6$ electrons	o: $4 \cdot 10^8$ electrons	-: $T_e$ .

Below  $N_0 = 9 \cdot 10^3$  electrons no breakdown occurs at  $E = 30$  kV/cm. Hence,  $N_{0,min} = 9 \cdot 10^3$  is the critical minimum electron number at  $E = 30$  kV/cm. For  $E = 30.5$  kV/cm no breakdown occurs below  $N_0 = 1.3 \cdot 10^3$  electrons. Hence,  $N_{0,min} = 1.3 \cdot 10^3$  is the critical minimum electron number at  $E = 30.5$  kV/cm. In dry air the critical minimum electron number is much smaller. This can be attributed to the effect of detachment creating "delayed electrons" for microseconds in time.

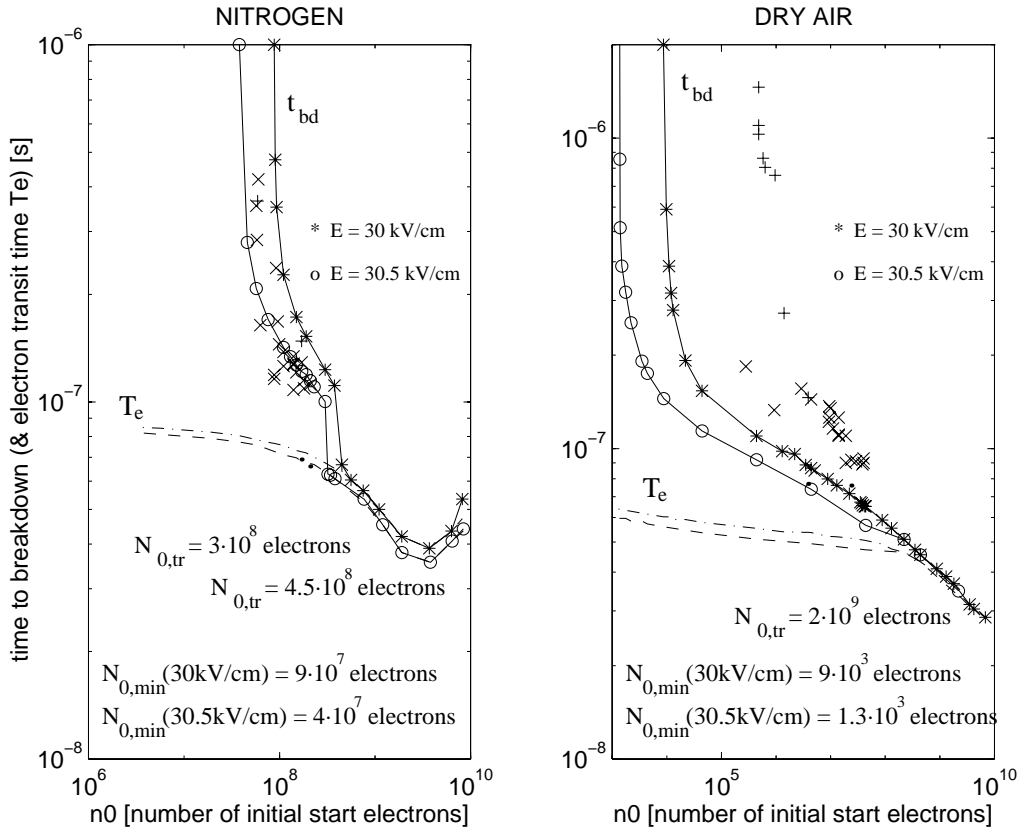


**Fig.4.20** Time to breakdown  $t_{bd}$  (drawn line) and electron transit time  $T_e$  (dashed line) as a function of the number of initial electrons  $N_0$ .

Measured values:  $t_{bd}$  +: 30 kV/cm    x: 30.5 kV/cm     $T_e$  •: 30 - 30.5 kV/cm.  
 Simulated values:  $t_{bd}$  \*: 30 kV/cm    o: 30.5 kV/cm     $T_e$  -: 30 - 30.5 kV/cm.

The differences between the experimental behavior and the modelling results for dry air in Fig.4.20 for small electron numbers could be explained by the fact that in the simulations (presented here) the initial electron distribution  $N_0$  is kept constant (only the density is varied) whereas in the experiments (and in the other simulations) the electron distribution changes by varying the emitting area: a smaller area results in a larger space charge field (even at identical  $N_0$ -value) which reduces the time-to-breakdown (as was shown in Figs.4.16 and 4.17 in Section 4.3.2.1).

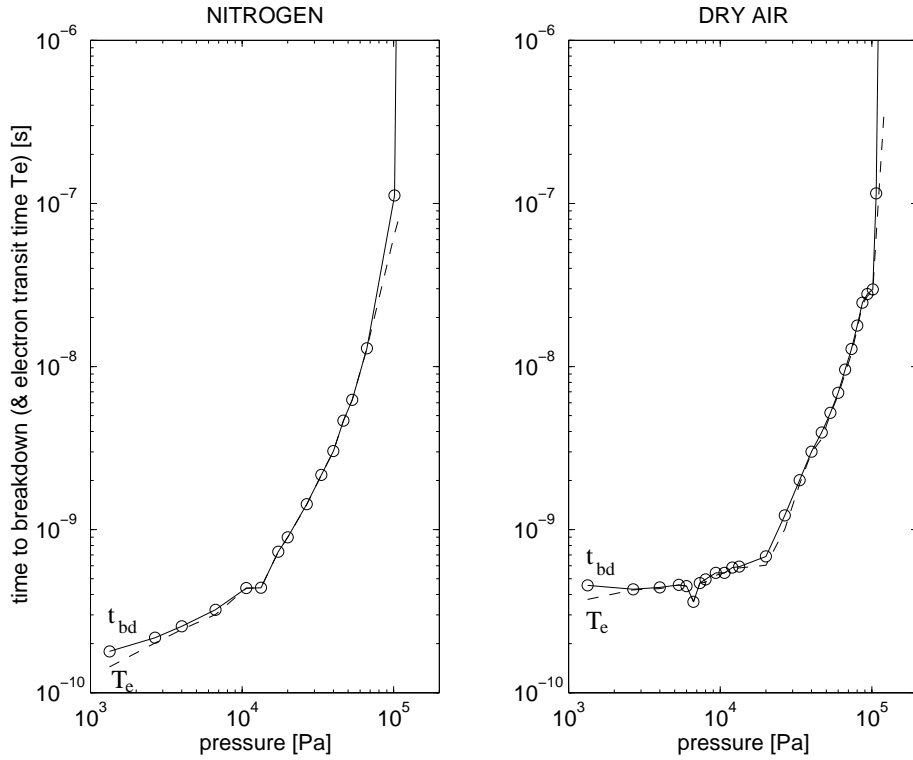


**Fig.4.21** Time to breakdown  $t_{bd}$  and electron transit time  $T_e$  as a function of pressure  $p$  ( $E=30$  kV/cm).

#### The influence of the pressure

**Figure 4.21** shows the influence of the pressure on the simulated time-to-breakdown  $t_{bd}$  and the electron transit time  $T_e$ . With increasing pressure the time-to-breakdown rapidly increases over more than two orders of magnitude. For nitrogen this happens gradually whereas for dry air the time-to-breakdown stays approximately constant up to a pressure of  $2 \cdot 10^4$  Pa. Above  $1.1 \cdot 10^5$  Pa no breakdown occurs for  $E=30$  kV/cm, and  $N_0=3.8 \cdot 10^8$  (nitrogen) and  $2 \cdot 10^6$  electrons (dry air).

#### The influence of the pressure reduced field $E/p$

In **Fig.4.22** the combined  $E/p$  curve for the simulated time-to-breakdown  $t_{bd}$  and the electron transit time  $T_e$  is shown.

The invariance to field  $E$  or pressure  $p$  in the  $E/p$ -plot indeed suggests an  $E/p$ -relationship.

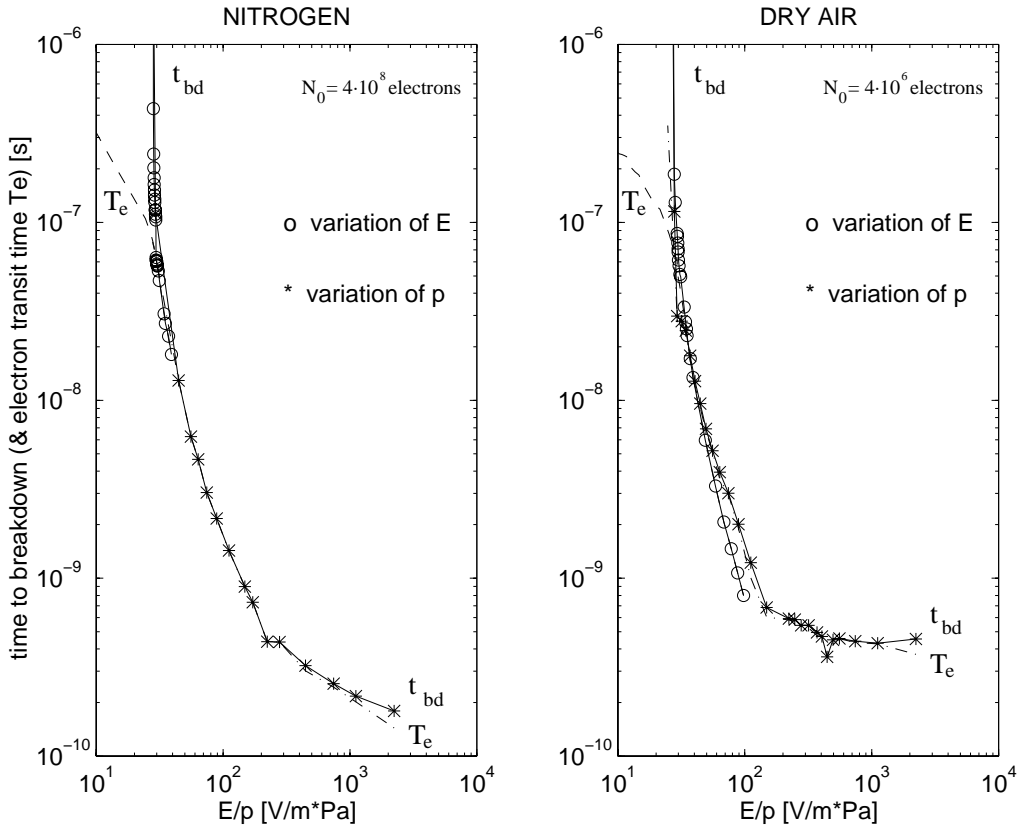


**Fig.4.22** Time to breakdown  $t_{bd}$  (drawn line) and electron transit time  $T_e$  (dashed line) as a function of applied field to pressure ratio  $E/p$ .

Concluding from the above:

- \* Differences in time-to-breakdown curves for dry air and nitrogen indicate a different discharge behavior. These fit the physical explanation of the occurring phenomena. The difference is caused by different mechanisms responsible for delayed electron production.
- \* A minimum critical electron number for streamer formation in nitrogen has been deduced from the two-dimensional model. The number is a function of the applied field.
- \* The simulated time-to-breakdown curves agree with literature data on impulse breakdown of air at atmospheric pressure.

### 4.3.3 Streamers in $SF_6$ in uniform and non-uniform fields

#### Experimental observations

##### A study of prebreakdown in $SF_6$ <sup>13</sup>

We will present results obtained from experiments:

- time-resolved optical and electrical measurements of streamer formation leading to breakdown in atmospheric  $SF_6$
- results for  $SF_6$  in uniform and **non-uniform fields**.

In section 4.2.3 examples of measured prebreakdown currents for  $SF_6$  in a uniform field were shown. From earlier data<sup>10</sup> it was found that an increase in the initial electron density (by reducing the area of photoemission on the cathode) results in a shorter time to first current maximum. A slight increase in applied field (just beyond the static breakdown field strength) results in a significant reduction of the time-to-breakdown for laser-induced breakdown in  $SF_6$ .

#### Non-uniform fields

Processes responsible for the formation of streamers in **non-uniform fields** will be discussed.

##### Half sphere - plane electrode geometry:

$$\text{Maximum field} = 3.3 \cdot E_0$$

For the half sphere - plane electrode geometry discussed in Chapter 3, section 3.3.4, and shown in Fig.3.6, the maximum field is calculated to be  $3.3 \cdot E_0$ , with  $E_0$  the uniform Laplacian field value.

**Fig.4.23** shows:

- (top) \* two current waveforms recorded at -37 kV
  - \* a current waveform recorded at -38 kV
  - (bottom) corresponding photomultiplier output signal
    - \* with "filter 89B ( $\lambda > 700 \text{ nm}$ )" and "filter 03FCG163 ( $300 \text{ nm} < \lambda < 700 \text{ nm}$ )"
    - \* or "filter 2B ( $\lambda > 400 \text{ nm}$ )" and "filter 03FCG121 ( $300 \text{ nm} < \lambda < 400 \text{ nm}$ )"
    - (see Fig.3.5)
  - ICCD camera images
- during prebreakdown for an inhomogeneous electrode geometry<sup>\*\*\*</sup>.

---

\*\*\* The optical activity seen in the ICCD images for  $SF_6$  is actually due to the 0.5%  $N_2$  contaminants in technically pure  $SF_6$ . The dominant emission band for both  $N_2$  and dry air is due to the 2<sup>nd</sup> positive system of  $N_2$ <sup>84,86,97,98</sup> with wavelengths ranging from 300 nm to 400 nm, well within the range of the ICCD's photocathode. For pure  $SF_6$  the generated optical activity typically has wavelengths in the far UV, thus outside the ICCD photocathode's operating region.



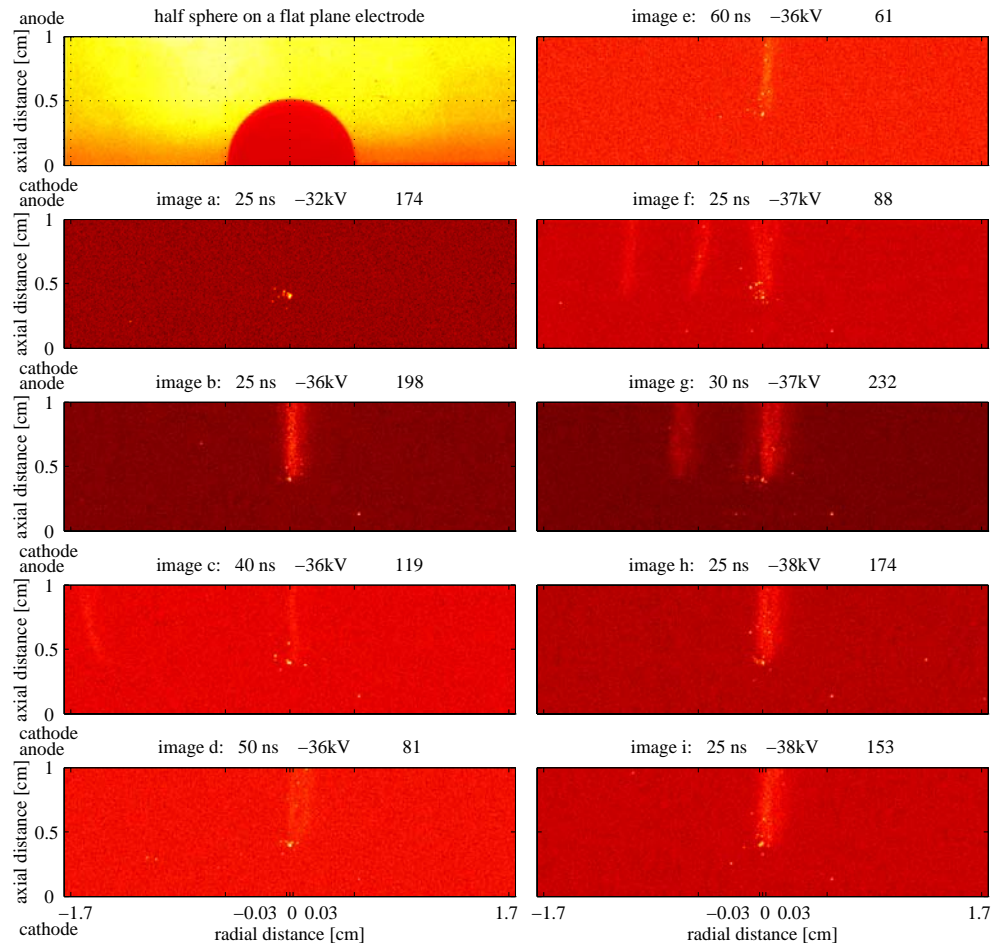


**Fig.4.23** (continued). Logarithmic intensity scale.

In Fig.4.23 the gap partially breaks down and recovers in which the applied voltage on the electrodes stays constant. After five consecutive Trichel-like-pulses (not shown), in which the complete gap is bridged by cathode directed streamers and an anode directed streamer, complete breakdown is observed.

The current in Fig.4.23 consecutively shows

- \* the laser-induced avalanche
- \* the ion drift phase
- \* the first Trichel-pulse.

The negative  $SF_6^-$  ions<sup>99</sup> do not play a role, as proposed by Gravendeel<sup>80</sup>, in the corona stabilization:

- \* The attachment time for electrons to  $SF_6$  molecules is too large to let attachment contribute to the cut off (quenching) of the discharge.
- \* The electron avalanche cloud itself creates the growth quenching space charge field.
- \* In its "tail" at the cathode half sphere tip the next avalanche is started, initiated by secondary electrons from positive ion impact or cathode photoemission (Trichel-pulses also occur for electrical field strength values at which there is no field emission at the cathode tip).

At later moments in time (after  $100\text{ ns}$  and until the peak of the Trichel-like current pulse) no optical discharge path can be observed in the drift phase, in agreement with the observation of negative ion clouds slowly drifting towards the plane anode electrode.

From the ICCD images shown in Fig.4.23 we observe:

- |  |   |
|--|---|
| ICCD image <i>a</i> :<br>(-32 kV)              | for voltages below -36 kV only small corona activity is observed (illuminated area $0.002\text{ cm}^2$ ).   |
| Images <i>b</i> through <i>e</i> :<br>(-36 kV) | corona activity around the sphere surface at different time instances, in which we see the formation of a discharge path of optical activity between half sphere and plane electrode. At this voltage level laser-induced gap-breakdown is obtained.      |
| Images <i>f</i> and <i>g</i> :<br>(-37 kV)     | increase in voltage up to -37 kV, causes typical "feathers", which (for wide enough electrode gaps) are superimposed on the corona activity present around the electrode, as discussed by Gravendeel <sup>80</sup> for negative corona discharges in air. |
| Images <i>h</i> and <i>i</i> :<br>(-38 kV)     | increasing the applied voltage even further leads to more optical activity and complete gap-breakdown.  |

**Figure 4.24** (left) shows the optical activity for a **larger emitting cathode area  $A$**  from which the initial electrons are released ( $N_2$ -laser spot area of  $0.1\text{ cm}^2$ ), resulting in

- \* more active corona regions
- \* an increased optical activity.

The number of consecutive Trichel-like-pulses is reduced to three (or four) after which gap-breakdown occurs.

A smaller initial electron density results in a slower build-up of the space charge field, and as a result a longer formation-time of the Trichel-like current pulse.

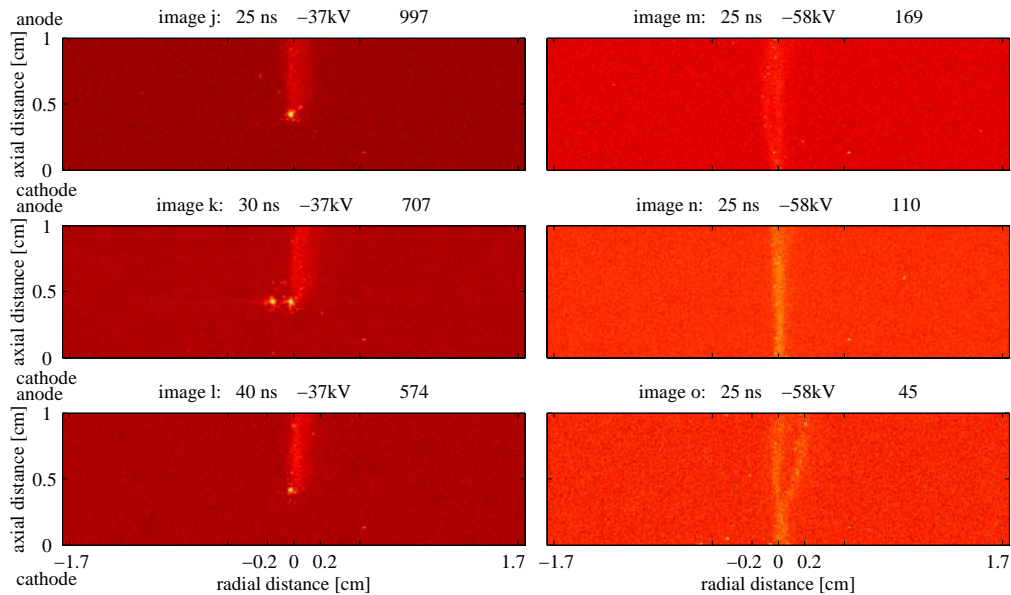


**Fig.4.24** ICCD images for prebreakdown in an inhomogeneous electrode geometry.  
 Half sphere - plane electrode geometry. 5 ns ICCD camera gate-shutter time.  
 Logarithmic intensity scale.  
 left: Optical activity for an  $N_2$ -laser spot area of  $0.1 \text{ cm}^2$ .  
 Top of sphere located at  $0.5 \text{ cm}$  on the vertical axis.  
 right: Optical activity for an increased gap width (gap= $1 \text{ cm}$ ).  
 Top of sphere located at  $0 \text{ cm}$  on the vertical axis.

On the right hand side in Fig.4.24 the activity is shown for an **increased gap width** (gap= $1 \text{ cm}$ )

- \* No or only one consecutive Trichel-like pulse is observed.
- \* The time between laser-induced activity and first Trichel-like pulse is larger than  $10 \mu\text{s}$ .
- \* The first negative ion cloud arriving at the anode results in immediate gap-breakdown.

ICCD images *m* and *o*: examples of multiple discharge activity paths in the gap region (the top surface of the half sphere is located at the bottom of these images).

Breakdown occurred at an applied voltage of  $-58 \text{ kV}$ .

**Paraboloid - plane geometry:**

$$\text{Maximum field} = 23 \cdot E_0$$

For the paraboloid - plane geometry discussed in Chapter 3, section 3.3.4, and shown in Fig.3.6, the maximum field is calculated to be  $23 E_0$ , with  $E_0$  the uniform Laplacian field value.

**Fig.4.25** shows results for a paraboloid - plane geometry (tip radius  $0.2 \text{ mm}$ ).

ICCD images *a* through *g*: corona activity around the tip for a negative (tip) voltage.

Images *h* through *o*: positive voltage.

(images *a* through *d*: illuminated area  $0.002 \text{ cm}^2$ ,

images *e* through *g*: illuminated area  $0.1 \text{ cm}^2$ )

Compared to the phenomena seen in Fig.4.23:

- \* The activity around the tip is more intense.
- \* No "feather"-like phenomena were observed anymore.

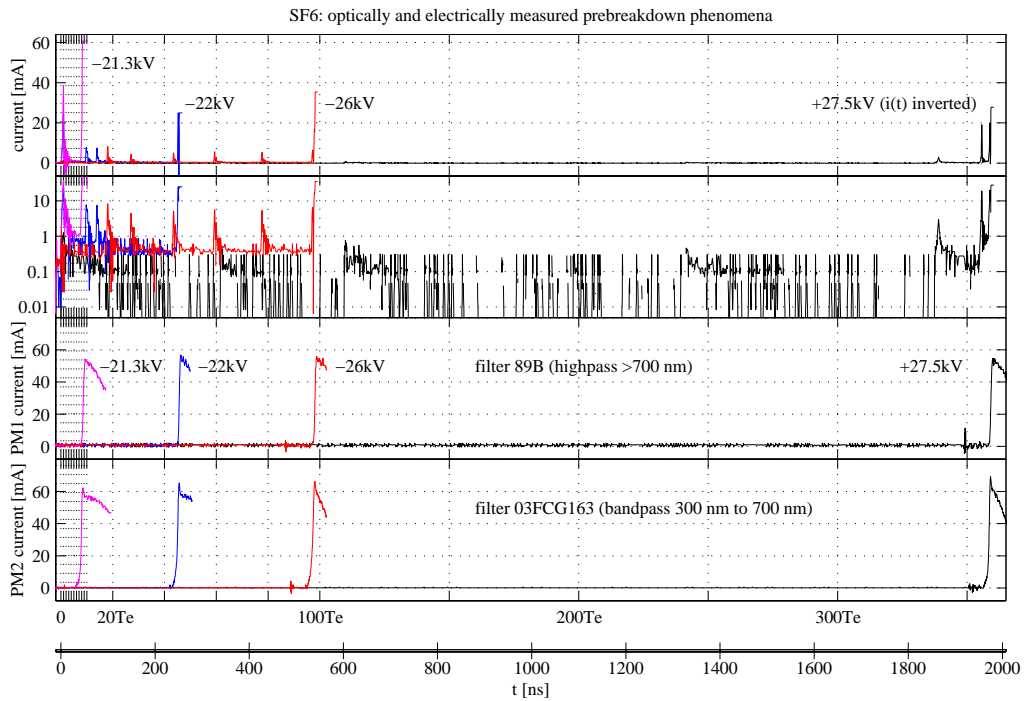


**Fig.4.25** Measured current waveforms, photomultiplier output and sequence of ICCD camera images of laser-induced discharge activity in an inhomogeneous electrode geometry.

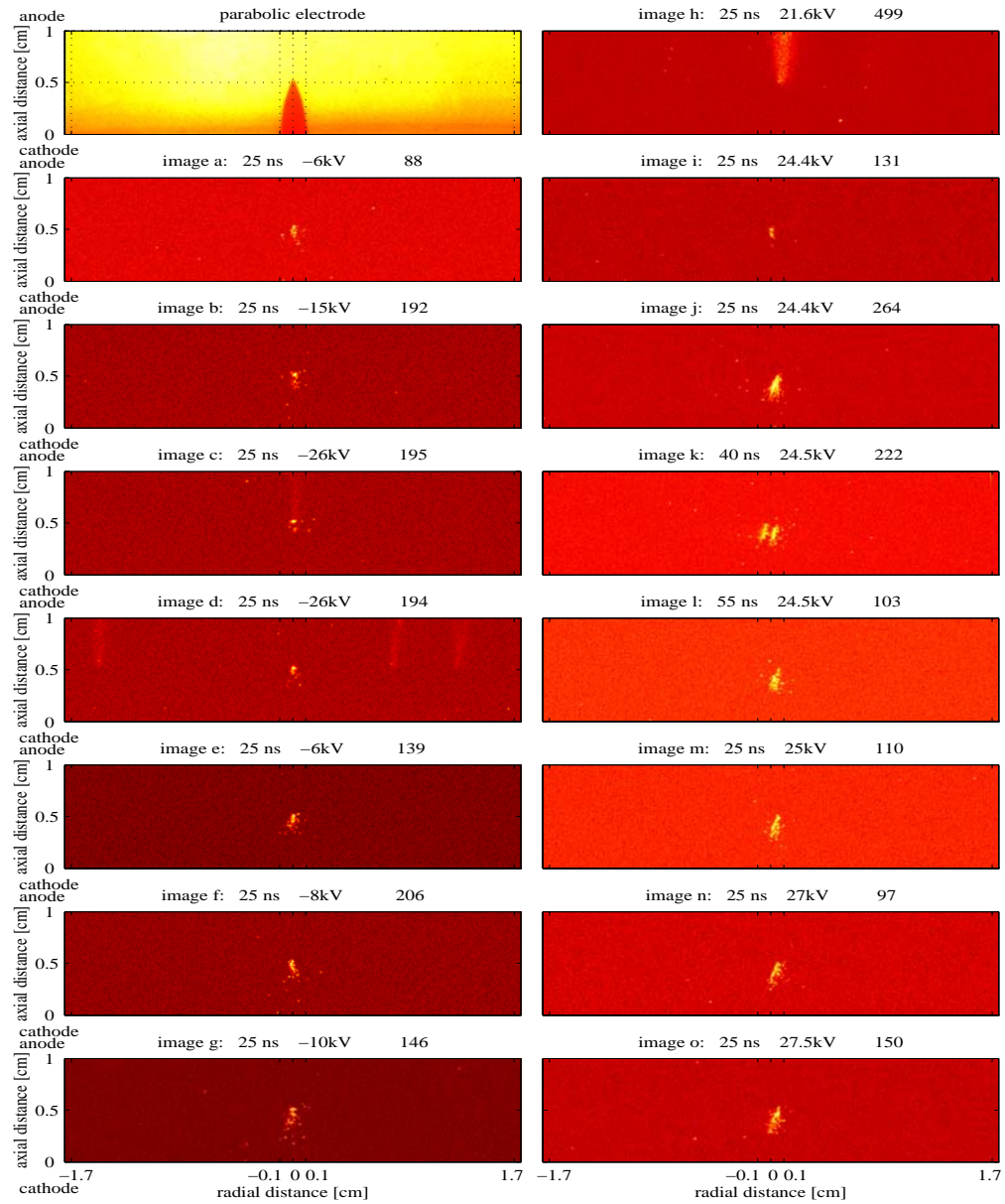


**Fig.4.25** (continued) ICCD images for prebreakdown in an inhomogeneous electrode geometry.

Paraboloid - plane electrode configuration. 5 ns ICCD camera gate-shutter time.

Logarithmic intensity scale.

left: Negative voltage

right: Positive voltage.

For negative applied voltages:

- \* Trichel-like-pulse regime.
- \* No regular (self-sustained) Trichel-pulses (as in air) were found
- \* Only irregular Trichel-pulses (as shown in Fig.4.25 for  $-21.3\text{ kV}$  ( $t \leq 42\text{ ns}$ ),  $-22\text{ kV}$  ( $t \leq 248\text{ ns}$ ) and  $-26\text{ kV}$  ( $t \leq 490\text{ ns}$ )).
- \* Gap breakdown for negative voltages larger than  $-22\text{ kV}$ .

For a positive applied voltage:

- \* Discharge activity starts at a higher voltage (also because we do not release photoelectrons from the tip).
- \* Gap breakdown occurs around the same voltage level ( $22\text{ kV}$ ).

This behavior in  $SF_6$  for positive voltage at the tip, known as "corona stabilization", for which the discharge activity starts at a higher voltage for positive tip voltages is also described by Kuffel and Zaengl<sup>57</sup>. Several electron avalanche generations arriving at the anode tip electrode are observed. In the positive space charge cloud left behind a cathode directed streamer forms leading to gap-breakdown. Initial electrons have to originate from atmospheric background irradiation since in the low field around the cathode plane no significant growth takes place, released electrons are attached to the strongly electronegative  $SF_6$  molecules forming negative ions preventing growth in discharge activity in these regions at low applied positive voltages.

From the above we conclude:

- \* We have succeeded in observing prebreakdown phenomena in  $SF_6$  at pressures up to atmospheric pressure.
- \* For non-uniform fields we have been able to make measurements of the optical activity related to prebreakdown phenomena in atmospheric  $SF_6$ .
- \* For large electrode radii we observe different simultaneous discharge paths ("feathers").
- \* For sharp electrodes we observe one path of optical activity.

In earlier work by Saxe<sup>84</sup>, Tholl<sup>85,93</sup>, Allen and Phillips<sup>86</sup>, Wagner<sup>87,88</sup>, Koppitz<sup>83,89</sup>, Doran<sup>90</sup>, Haydon<sup>91</sup>, Cavenor and Meyer<sup>92</sup>, Chalmers et al.<sup>94</sup> and Bayle et al.<sup>95</sup> the prevailing breakdown mechanisms in (atmospheric) nitrogen, dry air and sulphur hexafluoride were studied in a similar fashion, in which high-speed photographic recordings of ionization development were presented. The results described in Sections 4.2 through 4.3 of this thesis are in agreement with these experimental and theoretical observations.

## 4.4 Prebreakdown phenomena along insulator surfaces in dry air

### Introduction

This study is a continuation of earlier work by Verhaart<sup>21</sup> and deals with a study of avalanche and streamer formation along insulator surfaces in dry air<sup>14</sup>.

The field distribution for an insulator between two parallel plates in a dc field at the insulator gas interface will be determined. A dielectric can be characterized by a conductivity  $\sigma$  in parallel to a frequency dependent dielectric displacement "conductivity"  $j\omega\epsilon$ .

For the situation of two dielectrics between two parallel plates, in which one is a gas:  $\epsilon_r=1$  and conductivity  $\sigma_r \approx 0$ .

The condition for which the dielectric spacer is dominated by the electrical field through the dielectric constant rather than by conduction, can be derived from

$$J = (\sigma + j\omega \epsilon_0 \epsilon_r) E \quad (4.2)$$

$$|j\omega| > \frac{\sigma}{\epsilon} = \frac{1}{\epsilon \rho} \quad (4.3)$$

For epoxy  $\epsilon_r=5.0$  and  $\rho=10^{14} \Omega \text{ cm}$

$$f = \frac{\omega}{2\pi} > \frac{1}{2\pi \epsilon_0 \epsilon_r \rho} = \frac{1}{2\pi \tau} = 4 \cdot 10^{-5} \text{ Hz} \quad (4.4)$$

We can visualize this in the time-domain by applying a voltage step to an insulator. At first the behavior will be purely dielectric until, after an RC-time determined by the dielectric, a static dc field distribution is established which is governed by the conductivity ratio.

$$\tau = RC = \left(\frac{\rho d}{A}\right) \left(\frac{\epsilon_0 \epsilon_r A}{d}\right) = \epsilon_0 \epsilon_r \rho \quad (4.4a)$$

For the above worst case example we find  $\tau = \epsilon_0 \epsilon_r \rho = 8.85 \cdot 10^{-12} \cdot 5.0 \cdot 10^{14} = 4.4 \cdot 10^3 \text{ s} \approx 74 \text{ minutes}$ . Our measurement is taken well within this time frame, so though the applied field is dc, for our region of interest the field distribution for the discharge along the spacer is governed by the dielectric constant  $\epsilon_r$ .

### Experimental observations

Results for discharge phenomena in air along **PTFE**, **PVC** and **epoxy insulators** will be presented. The insulator geometries used are shown in Figs.3.7 and 3.8.

The results obtained from experiments consist of

- measured prebreakdown currents
  - photomultiplier output signals representing space-integrated optical activity in the gap
  - sequence of optical ICCD images
- at various time moments during breakdown for different insulator geometries.

As an example **Fig.4.26** shows:

- (top) \* current waveforms
  - (bottom) \* corresponding photomultiplier output signals with filters
- during breakdown for frustum of a cone PTFE spacer geometry I.

The characteristics of the filters used were shown in Fig.3.5.

On the horizontal axis the time is normalized to the electron transit time in a uniform field  $T_e$  in air with no spacer present.

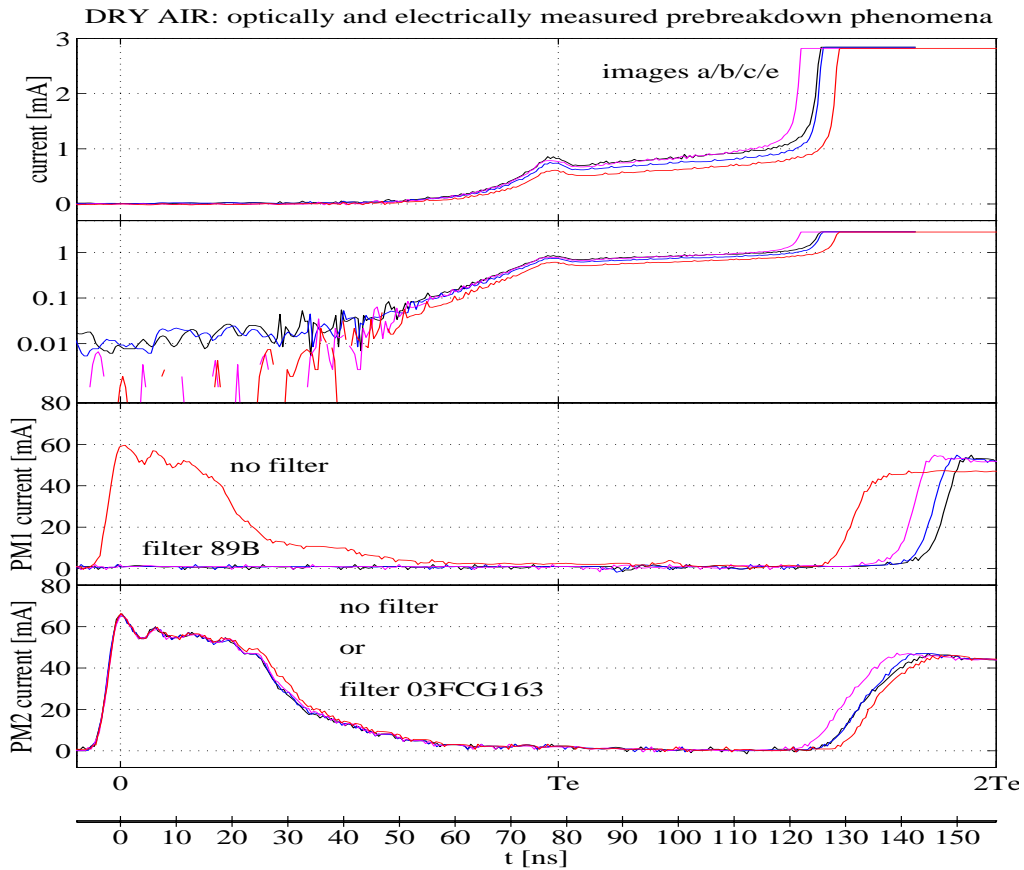


**Fig.4.26** Measured current waveforms (on a linear- and log-scale) and photomultiplier output signals for prebreakdown along frustum of a cone PTFE spacer geometry I (30 kV).

From Fig.4.26 the following observations are made:

- \* The photomultiplier output signals (except for filter 89B) show the  $N_2$ -laser pulse and thereby the time moment at which the laser-induced discharge activity starts.
- \* Filter 89B suppresses this dominant  $N_2$ -laser pulse line ( $\lambda=337 \text{ nm}$ ) completely.
- \* At breakdown and over-exponential current growth also optical activity in the IR ( $\lambda>700 \text{ nm}$ ) is generated (filter 89B).
- \* No difference was observed in photomultiplier signal (PM2) with filter 03FCG163 or without filter.

Use of photomultipliers helps to depict the time moment at which the laser-induced discharge activity starts, and to depict the occurrence of actual breakdown. The wavelength range for optical activity before breakdown is found to be below  $700 \text{ nm}$ . The ICCD camera used is however far more sensitive to optical activity.

After this first example we will now show some results for:

- 1) PTFE: influence of the spacer shape.
- 2) PVC: influence of the spacer shape.
- 3) Comparison between the results for PTFE and PVC for different spacer shapes.
- 4) Cylindrically shaped spacers: influence of insulating material.

#### Observations with different spacers

Figure 4.27 shows the

- measured prebreakdown currents
- photomultiplier output representing space-integrated light activity in the gap
- sequence of optical ICCD images

at various time moments during breakdown for different insulator geometries.

The influence of the spacer shape on the various parameters is shown in **Table 4.3**.

We will discuss the observations made for each situation.

**No spacer:** time-to-breakdown  $t_{bd}=110 \text{ ns}$   
 peak current  $i(T_e=79 \text{ ns})=9 \text{ mA}$ .  
 (the vertical scale is divided by 2).

#### Frustum of a cone PTFE spacer I:

- \* Electric field attenuation at the cathode side (and field enhancement ( $2E_0$ ) at the anode along the spacer surface) leads to an increase in the time-to-breakdown ( $t_{bd}=121 \text{ ns}$ ) relative to the situation with no spacer present.
- \* The small number of initial electrons ( $N_0=2 \cdot 10^6$ ) released results in a relatively small peak current  $i(T_e)$ .
- \* For times beyond  $T_e$  the current increases.

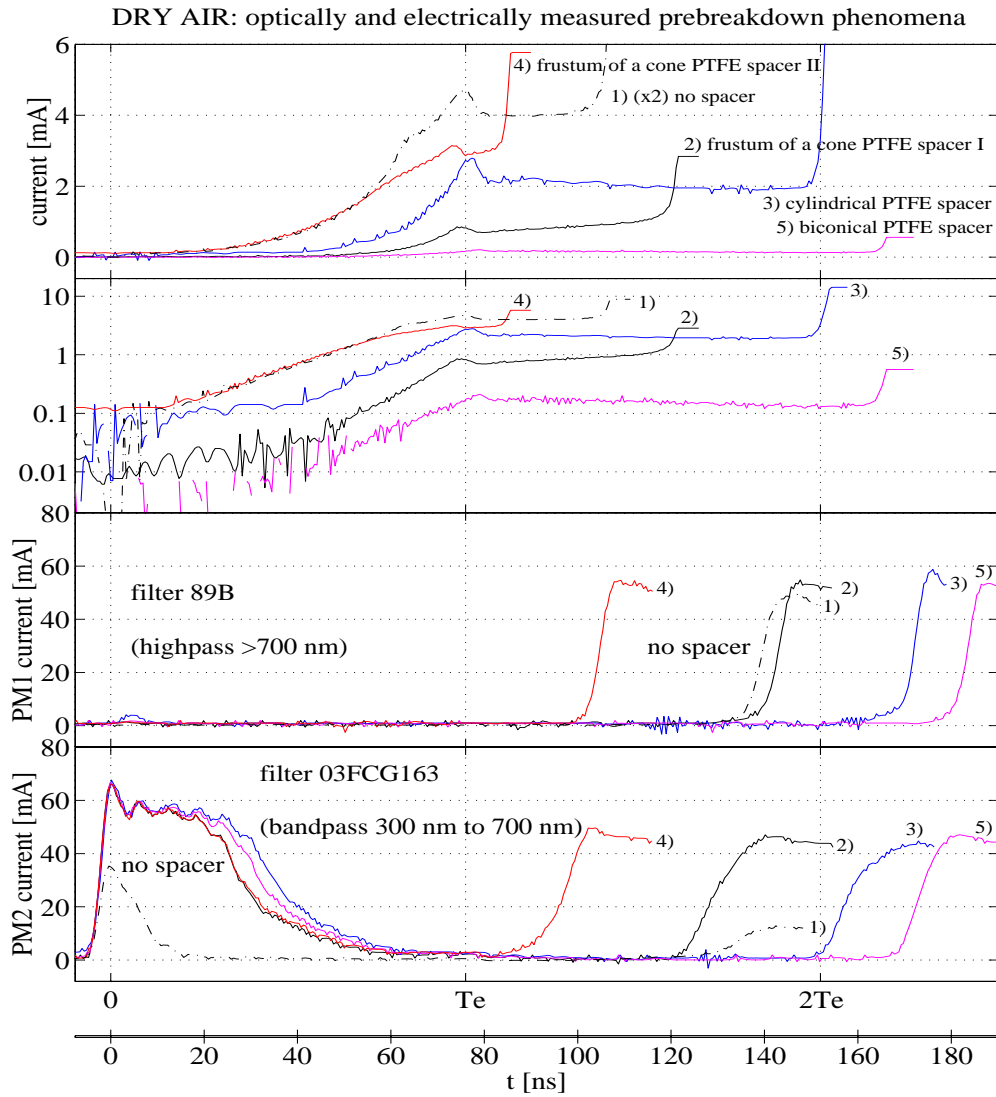


**Fig.4.27** Measured current waveforms, photomultiplier output and sequence of ICCD camera images of a laser-induced avalanche and its transition to a streamer along PTFE spacer geometries. The corresponding times on the measured current waveforms are indicated. The cathode (bottom) and anode (top) surfaces are located at  $0$  and  $1$  cm respectively on the vertical axis. The horizontal scaling in centimetres is also indicated. The initial electrons are released at  $t=0$  from the cathode (bottom) region around  $x=0$  ( $-0.05$  cm  $< x < 0.05$  cm). The maximum photon count per pixel is denoted in the upper right corner of each image. Gate-shutter time of ICCD is  $5$  ns. Logarithmic intensity scale.

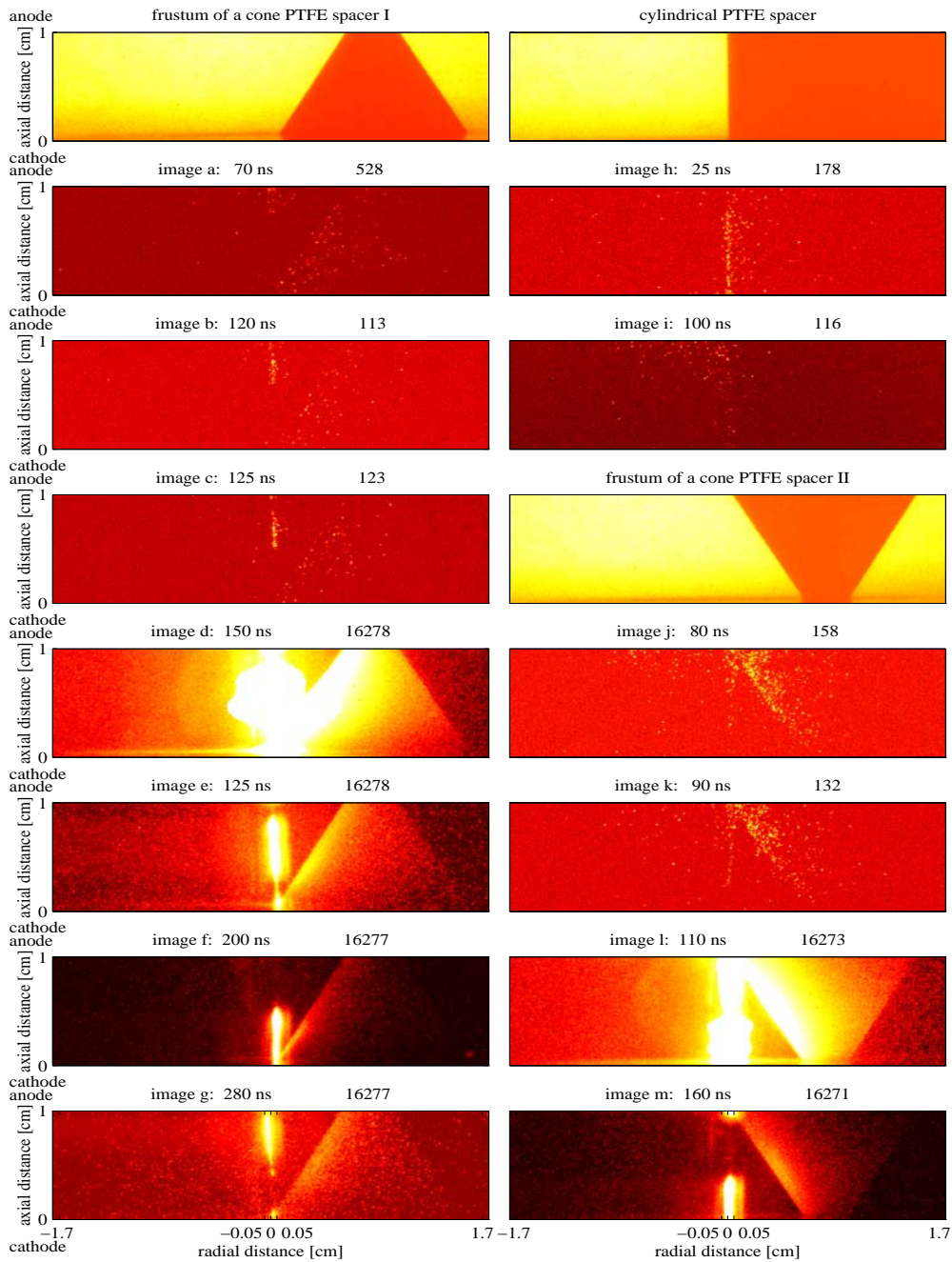


**Fig.4.27** (continued) ICCD camera images of breakdown along PTFE spacer geometries.

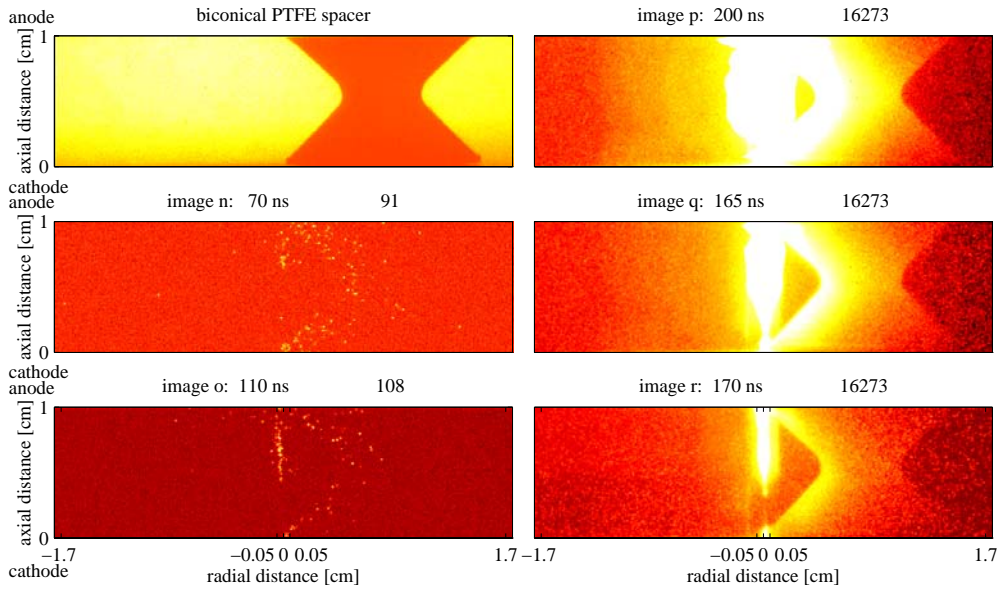


**Fig.4.27** (continued) ICCD camera images of breakdown along a biconical PTFE spacer geometry.

- \* Beyond  $T_e$ , due to the increased growth near the anode region, the time-to-breakdown  $t_{bd}$  is shortened.
  - \* The field attenuation at the cathode and the field enhancement at the anode together result in an overall similar value for  $T_e$  compared to the situation with no spacer present.
- ICCD image *a*: primary avalanche's arrival at the anode.  
 Images *b* and *c*: streamer formation.  
 Images *d* through *f*: streamer propagation.

#### **Cylindrical PTFE spacer:**

- \* The time-to-breakdown increases ( $t_{bd}=160\text{ ns}$ ) compared to the situation without a spacer.
- \* Immobilized electrons trapped at the surface delay breakdown formation.

#### **Frustum of a cone PTFE spacer II:**

- \* Small electric field enhancement at the cathode side and attenuation at the anode side lead to a lower breakdown voltage ( $29.9\text{ kV}$ ).
- \* Decrease in the time-to-breakdown ( $t_{bd}=89\text{ ns}$ ) compared to the situation with no spacer.
- \* Current growth deviates considerably from exponential avalanche growth.
- \* Due to the surface charging by trapped electrons a considerable radial space charge field is build up enabling shorter streamer formation times.

**Table 4.3** Influence of the spacer material and shape on the breakdown voltage,  $T_e$ ,  $t_{bd}$ , and the fields at the cathode / anode interfaces.

Field configuration	$V_{bd}$ [kV]	$T_e$ [ns]	$t_{bd}$ [ns]	$E_{cathode}$	$E_{anode}$
no spacer	30.0	79	110		
frustum of a cone PTFE spacer I	30.0	77	121	attenuated	enhanced
cylindrical PTFE spacer	30.0	80	160		
frustum of a cone PTFE spacer II	29.9	76	89	enhanced	attenuated
biconical PTFE spacer I	30.0	82	172	attenuated	attenuated
frustum of a cone PVC spacer I	29.5	74	94	attenuated	enhanced
cylindrical PVC spacer	29.0	76	316		
frustum of a cone PVC spacer II	29.0	54	92	enhanced	attenuated
cylindrical epoxy spacer	29.0	75	166		

ICCD images  $j$  and  $k$ : streamer formation.

Images  $l$  and  $m$ : streamer propagation.

**Biconical PTFE spacer:**

\* The time-to-breakdown increases ( $t_{bd}=172$  ns) relative to the situation with no spacer.

\* Like in the situation of frustum of a cone spacer I, only a very small number of initial electrons is released resulting in a relatively small peak current  $i(T_e)$ .

ICCD image  $n$ : primary avalanche's arrival at the anode.

Image  $o$ : streamer formation.

Images  $p$  through  $r$ : streamer propagation.

Figures 4.28 and 4.29 show similar results for PVC spacers and an epoxy spacer.

PTFE:  $\epsilon_r=2.05$

PVC:  $\epsilon_r=3.2$

epoxy:  $\epsilon_r=5.0$

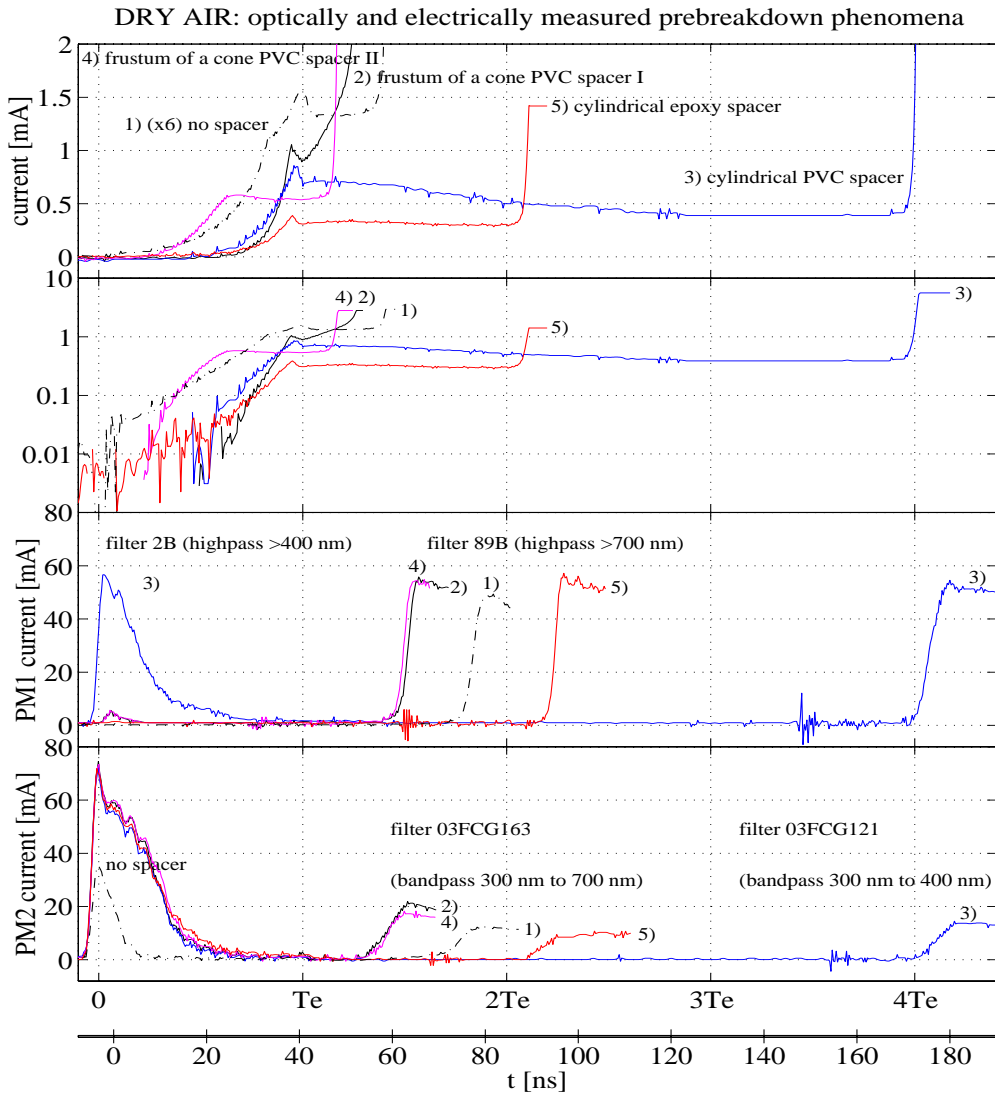
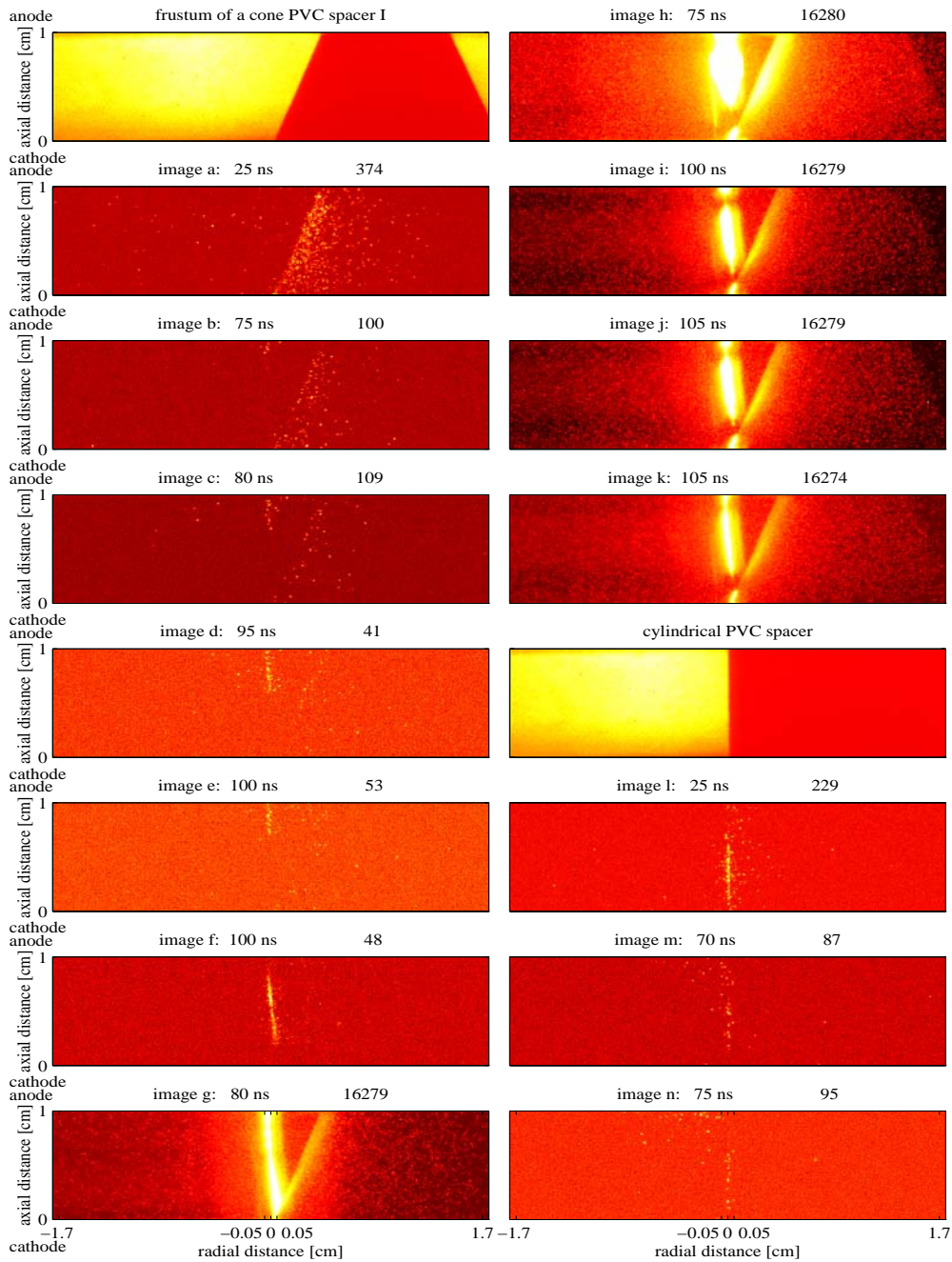
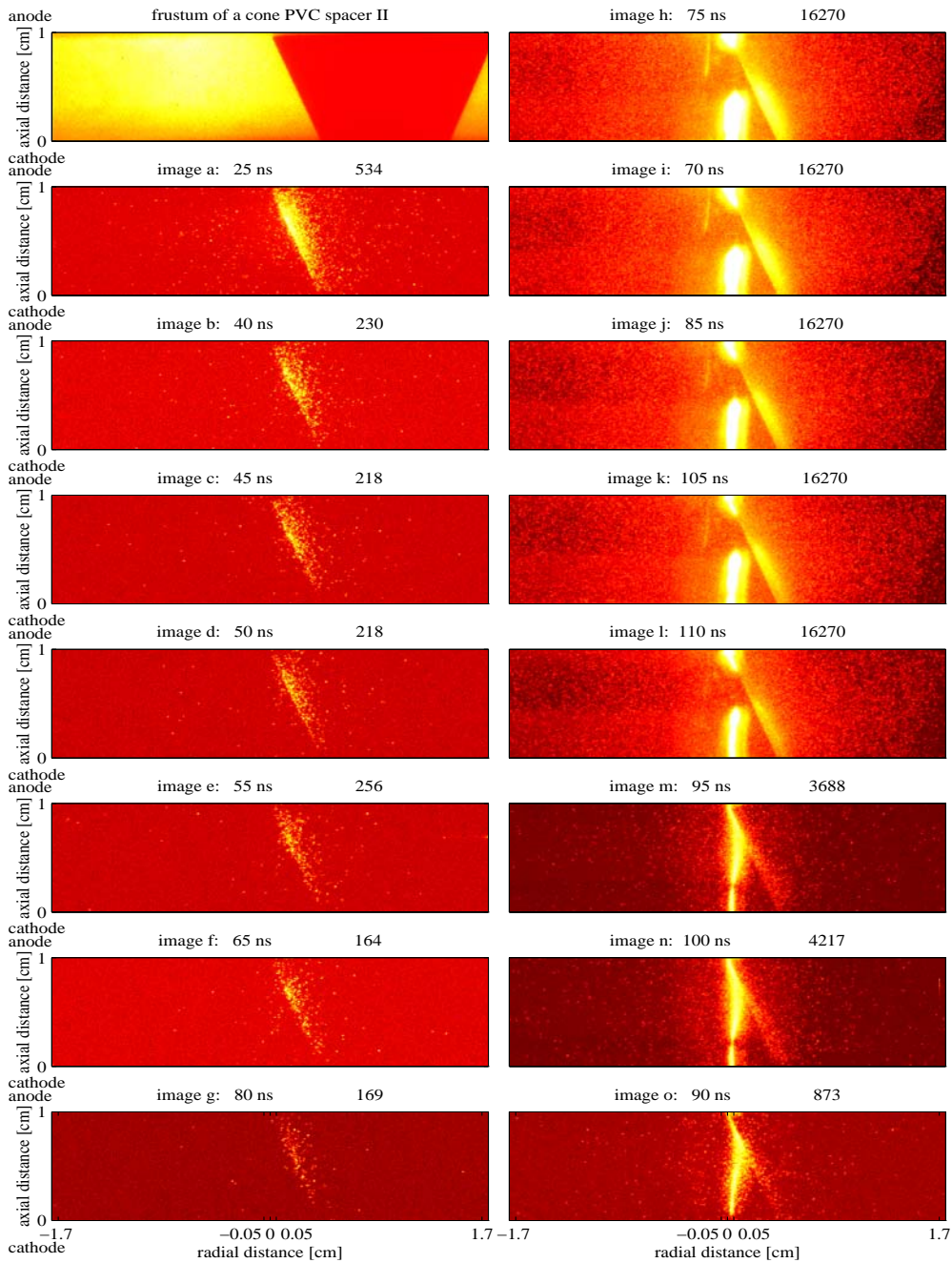


Fig.4.28 Measured current waveforms, photomultiplier output and sequence of ICCD camera images of breakdown along PVC spacer geometries.



**Fig.4.28** (continued) ICCD camera images of breakdown along PVC spacer geometries.



**Fig.4.28** (continued) ICCD camera images of breakdown along PVC spacer geometries.

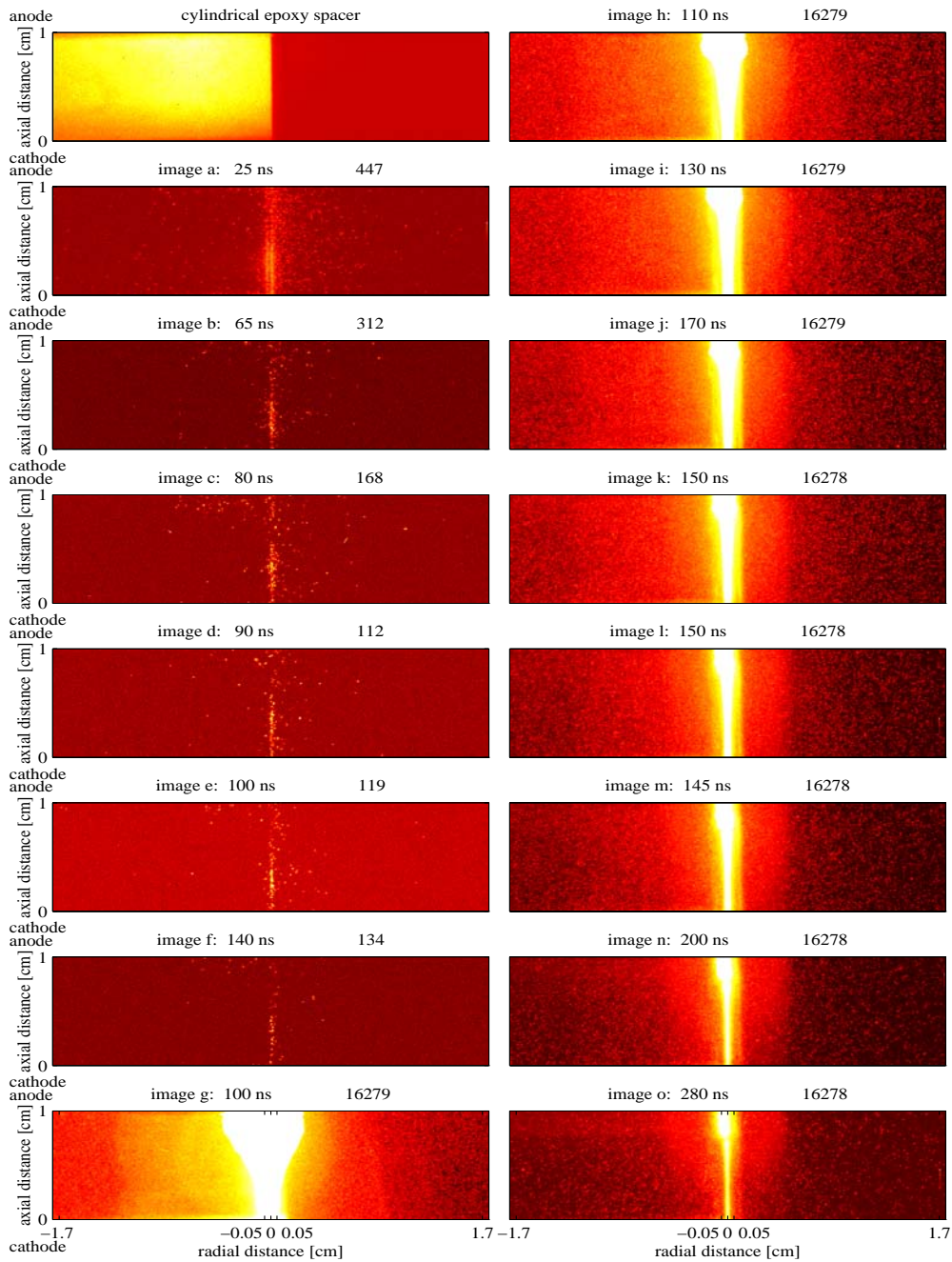


**Fig.4.29** ICCD camera images of breakdown along a cylindrical epoxy spacer geometry.

From Figs.4.28 and 4.29 the following observations are made:

**Frustum of a cone PVC spacer I:**

- \* Beyond  $T_e$ , due to the increased growth near the anode region, the time-to-breakdown  $t_{bd}$  is shortened relative to the situation with no spacer present.

ICCD images *a* and *b*: primary avalanche's transit and arrival at the anode.

Images *c* through *f*: streamer formation.

Images *g* through *k*: as the streamer propagates it becomes narrower.

**Cylindrical PVC spacer:**

- \* The time-to-breakdown increases ( $t_{bd}=316\text{ ns}$ ) compared to the situation without a spacer.

**Frustum of a cone PVC spacer II:**

- \* Small electric field enhancement at the cathode side and attenuation at the anode side lead to a lower breakdown voltage.

- \* Decrease in the electron transit time  $T_e$ .

- \* Decrease in the time-to-breakdown ( $t_{bd}=92\text{ ns}$ ) compared to the situation with no spacer.

- \* Current growth deviates considerably from exponential avalanche growth.

ICCD images *a* through *e*: primary avalanche's transit and arrival at the anode.

Images *f* and *g*: streamer formation.

Images *h* through *o*: streamer propagation.

**Cylindrical epoxy spacer:**

- \* The time-to-breakdown increases ( $t_{bd}=166\text{ ns}$ ) compared to the situation without a spacer.

ICCD images *a* and *b*: primary avalanche's transit and arrival at the anode.

Images *c* through *f*: streamer formation.

Images *g* through *o*: as the formed streamer propagates it becomes narrower.

For larger dielectric constants (PVC and epoxy) the gap breaks down partially along the spacer surface, in other words not perpendicular to the electrode surface (no influence is seen in Fig.4.27, whereas in Fig.4.28 influences are shown in image *k* for the frustum of a cone PVC spacer I and images *h* through *o* for the frustum of a cone PVC spacer II).

From the above the following can be concluded:

- \* For larger dielectric constants  $\epsilon_r$  the gap breaks down partially along the spacer surface, and not just perpendicular to the electrode surface.
- \* The modification of the electric field by a spacer is dominating the discharge resulting in an increase/decrease of the breakdown field strength and time-to-breakdown.
- \* This is ascribed to the field distortion and (only in case of a cylindrical spacer) to surface trapping or detrapping processes.
- \* For other than cylindrical shapes the insulator surface itself seems to be playing a minor role on the prebreakdown behavior.
- \* From the good reproducibility of the resulting breakdown voltages and the observed phenomena we conclude breakdown conditioning through surface charging is of minor importance under these conditions, in contrast to the situation in vacuum<sup>100,101</sup>.

## Chapter 5

### Application to Partial Discharges in Voids

*In this chapter an application of the insights from the work done on prebreakdown phenomena in gases to partial discharges in voids in solid insulating materials is presented. The following six papers are all international conference contributions on this subject. The first paper "A Time-Dependent Model of Partial Discharges in Voids" and the second paper "A Time-Resolved Study of the Physical Processes Governing Void Discharges" are a good introduction to the subject.*

*The third paper presents "The Influence of Dielectric Material on Partial Discharges in Voids". The fourth paper "Partial Discharge Detection in Insulators; Scaling Relationships and Practical Implications" shows some of the modelling results.*

*The fifth and sixth paper, "Partial Discharges in Micrometer Voids in PTFE" and "Partial Discharge Modelling and Measurements on Micrometer Voids in Solid Dielectrics", present measurements on partial discharges in micrometer voids.*

**5.1 A time-dependent model of partial discharges in voids<sup>1</sup>**

7<sup>th</sup> International Symposium on Gaseous Dielectrics, Knoxville, TN, USA, April 1994















**5.2 A time-resolved study of the physical processes governing void discharges<sup>2</sup>**

1994 Conference on Electrical Insulation and Dielectric Phenomena, Arlington, Texas, USA, October 1994.











**5.3 The influence of dielectric material on partial discharges in voids<sup>3</sup>**

Presented at the 9<sup>th</sup> International Symposium on High Voltage Engineering, Graz, Austria, August 28<sup>th</sup> to September 1<sup>st</sup>, 1995.







#### **5.4 Partial discharge detection in insulators; scaling relationships and practical implications<sup>4</sup>**

Presented at the 11<sup>th</sup> International Conference on Gas Discharges and Their Applications, Tokyo, Japan, September 11<sup>th</sup> to September 15<sup>th</sup>, 1995.







### **5.5 Partial discharges in micrometer voids in ptf<sup>e</sup>**

Presented at the 1996 IEEE International Symposium on Electrical Insulation, Montréal, Québec, Canada, June 1996.







**5.6 Partial discharge modelling and measurements on micrometer voids in solid dielectrics<sup>8</sup>**

Presented at the IEE Seventh International Conference on Dielectric Materials, Measurements and Applications, Bath, United Kingdom, September 1996.







## 5.7 Other applications

With the high bandwidth experimental setup PD-currents for small voids in various solid insulating materials have been measured. The 1-D hydrodynamic model assumes a realistic discharge radius as based on both optically and electrically measured data on discharges and yields a satisfactory description. Photoemission of secondary electrons from void surfaces has to be included. For relatively large void heights successive avalanche generations are clearly distinguishable in both the measured and the simulated PD-currents. The bandwidth of the measurement setup allows to distinguish the influences of electrons and ions. The measured PD-current waveforms for different insulating materials yield more information on the relevant PD-processes. Secondary electron emission from the void surfaces, together with the void geometry, determine the current waveform.

The dielectric material influences the discharge characteristics:

- \* the dielectric constant  $\epsilon_r$  of the dielectric material influences the void field.
- \* the quantum yield for secondary-electrons from surfaces influences the inception field.
- \* Experiments show the  $q_{real} / E_{inc}$  ratio is independent of the dielectric material; this is due to field quenching.

Scaling relations are derived for the charge and inception voltage for PD's in cylindrical and spherical voids. Only for very large or small void height to radius ratios the considered models for cylindrical voids lose their validity in describing the charge. The dipole model gives a good description of the measurable quantities for spherical voids.

The results of the work presented in the preceding sections in which void sizes down to  $10 \mu m$  were studied, do not suggest the existence of a smallest detectable void size. For micrometer voids the discharge phenomena changes from gas discharge like avalanche and streamer breakdown towards a spark like plasma (with electron temperatures up to  $20 eV$  at an electron density of  $10^{19} cm^{-3}$ ) as was found by Lepoint et al.<sup>102</sup>.

Besides application to partial discharges in voids presented in the preceding sections, there are many other applications of the insights gained from the work described in this thesis on Dielectric Breakdown in Insulating Gases.

For example in flue gas treatment by electrical corona discharges as a means of pollution control<sup>18</sup>, we find the need of understanding the discharge behavior and the relevant reactions to achieve higher cleaning efficiencies by controlling the discharge characteristics.

Also Electrostatic Discharges (ESD) are of interest as an object of study, since especially the miniaturization of integrated circuits leads to circuits more sensitive to all kinds of EMC problems including ESD. In the context of ESD the time-to-breakdown is important since it determines the high frequency content of the discharge. Therefore better understanding of these phenomena by insights gained from the prebreakdown modelling techniques<sup>47</sup> can be very helpful.

## Chapter 6

### Evaluation of the Model

*In this chapter an analysis and a discussion of the relevant parts of our 2-D hydrodynamic model for different gases and various situations is presented. Through parameter variation techniques insight is gained on the relevant and redundant parts for specific conditions of interest. The result is a simplified model which can give results more quickly.*

#### 6.1 Introduction

In this chapter we study the limitations of the modelling techniques used and discuss possible solutions. It is shown on the basis of simulations what processes are mainly responsible for the formation of a streamer. Simulated particle density distributions give insight in the streamer formation phases leading to breakdown. From this we can determine relevant processes and parameters, and thereby "strip" the complex physical 2-D hydrodynamic model developed initially, to a "simplified" model only incorporating the dominant processes and species for a specific condition range.

#### 6.2 Limitations of numerical techniques for describing prebreakdown

In a preliminary study on the 2-D hydrodynamic model itself we looked at the possibility (often used in the field of electromagnetics) of neglecting higher order (or lower order) flux terms, to thereby greatly reduce the simulation time. This may for instance result in negative species densities which are then set to zero, since negative species densities have no meaning physically. Various techniques were tried.

**Figure 6.1** is an illustration of numerical diffusion, in which an originally gaussian electron distribution propagates from cathode to anode in an applied field, using an FCT routine<sup>33,37,42</sup> with Zalesac's peak preserver<sup>29</sup>. Also shown are the situations in which lower-order, respectively higher-order, flux terms were excluded. A linear mesh is used with 400 axial and 22 radial elements, in which the cathode is located at 0 and the anode at 400. This clearly shows for both situations, excluding the lower-order or the higher-order flux terms, the broadening and distortion of the initial pulse.

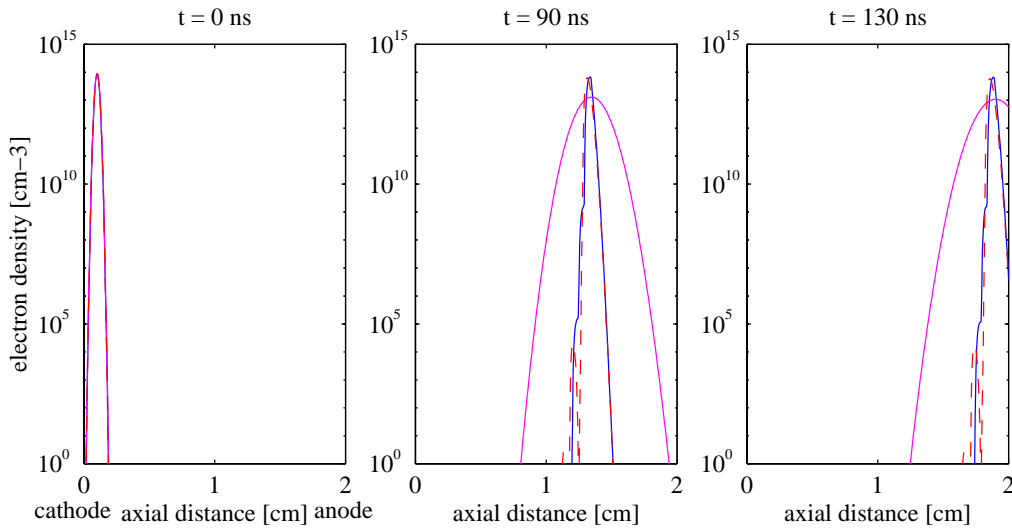


**Figure 6.1** Numerical diffusion illustrated by a gaussian electron distribution ( $N_0=7 \cdot 10^{12}$ ) propagating from cathode to anode for a positive applied voltage in an applied field using an FCT routine with Zalesac's peak preserver<sup>29</sup> (solid line), neglecting lower-order (grey line), respectively higher-order flux terms (dashed line).  
Conditions:  $E=30 \text{ kV/cm}$ ,  $\text{gap}=2 \text{ cm}$ .

**Figure 6.2** shows the influences of considering fluxes in the numerical calculations on a simulated avalanche in atmospheric nitrogen at  $E=30 \text{ kV/cm}$ . On the horizontal axes the time is given in terms of the electron transit time in a uniform field  $T_e$ . Excluding the higher order flux terms results in a less pronounced current maximum due to an increase in numerical diffusion which broadens the density distributions as in Fig.6.1. The time-to-breakdown increased by 15%, whereas the total simulation time decreased by 6%. Neglecting lower-order fluxes results in even larger errors as can be seen from Fig.6.2 (bottom). In the actual computer runs we used the ZFCT routine and included the higher and lower order terms to avoid the above mentioned problems.

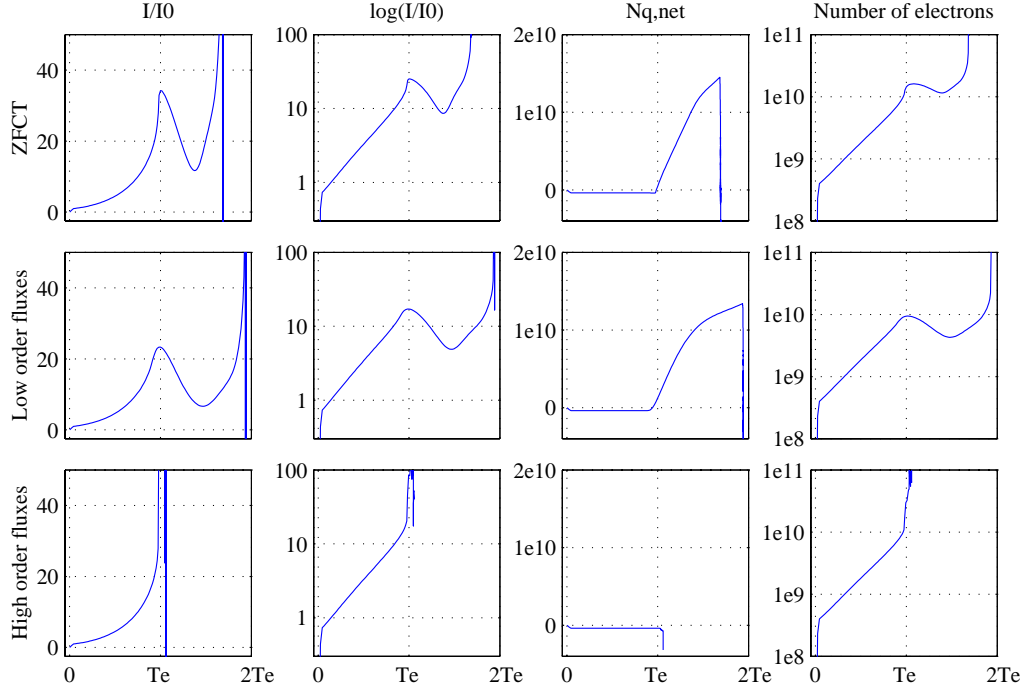


**Figure 6.2** Normalized current  $i(t)/i_0$ , total net number of charge carriers  $N_{q,net}$  and number of electrons  $N_e$  as a function of time for the full 2-D model using the FCT routine with Zalesac’s peak preserver, only including lower-order or only including higher-order flux terms.

From the above we conclude that under our ionizing growth conditions small changes in remote regions of the mesh still have a very large influence elsewhere. The reason that we have to retain all higher order and lower order terms results from the complexity of our model in which gain and loss terms play a role. Still the model is a relatively simple approximation of reality, since it does not consider the (statistical) particle behavior (as in a Monte-Carlo simulation), but only the "average" (fluid) behavior.

The space and time dependency of the various gas discharge parameters, in particular  $\alpha$  and  $\eta$ , is much more important than in the situation in which we only consider resulting fields, as in electromagnetics. Here we also look at the space and time integrated quantities like the volume integral resulting in the time-resolved current.

### 6.3 Different discharge regimes

In **Fig.6.3** (top) the current is shown as a function of time and applied field for nitrogen. For fields below  $E=28.85 \text{ kV/cm}$  ( $E < E_{min}$ ) only avalanches develop (light shaded region in Fig.6.3). With increasing field values the primary electron avalanche's magnitude and the number of successive avalanches increases.

Above  $E=28.85 \text{ kV/cm}$  ( $E_{min} < E < E_{tr}$ ) the primary avalanche crosses the gap after which one of the subsequent avalanches develops into a streamer leading to breakdown.

With increasing field the time-to-breakdown rapidly decreases, as does the number of successive avalanches preceding streamer formation and breakdown.

At  $30.3 \text{ kV/cm}$  a streamer forms even before the primary avalanche has crossed the gap, causing breakdown in times smaller than the electron transit time in a uniform field.

At even higher fields ( $E > E_{tr}$ ) the time-to-breakdown decreases further towards nanosecond breakdown. (Remark: the line plot at the intersection of  $50 \text{ mA}$  in the time - applied field plane is the time-to-breakdown parameter curve for nitrogen of Fig.4.19.)

Figure 6.3 (middle) shows the total net number of charge carriers (positive ions  $N_p$  minus electrons  $N_e$ ) in the gap region as a function of time and applied field. For times smaller than the electron transit time in a uniform field, due to the released initial electron pulse, the total net number of charge carriers is constant and negative.

After the primary electron avalanche reaches the anode a total net number of positive charge carriers results.

Above  $28.85 \text{ kV/cm}$  the total net positive number of charge carriers is of the order of  $10^{10}$ , and stays constant until  $30.3 \text{ kV/cm}$  for increasing field values. For this regime breakdown occurs as soon as the net positive number of charge carriers in the gap reaches  $10^{10}$ .

Above  $30.3 \text{ kV/cm}$  the number of electrons itself exceeds the order of  $1.2 \cdot 10^{10}$  and the avalanche develops into a streamer before the initial primary electron avalanche reaches the anode.

Figure 6.3 (bottom) shows the development of the number of electrons  $N_e$  as a function of time and applied field. From this the abrupt transition between one avalanche and successive avalanches before breakdown can be seen.

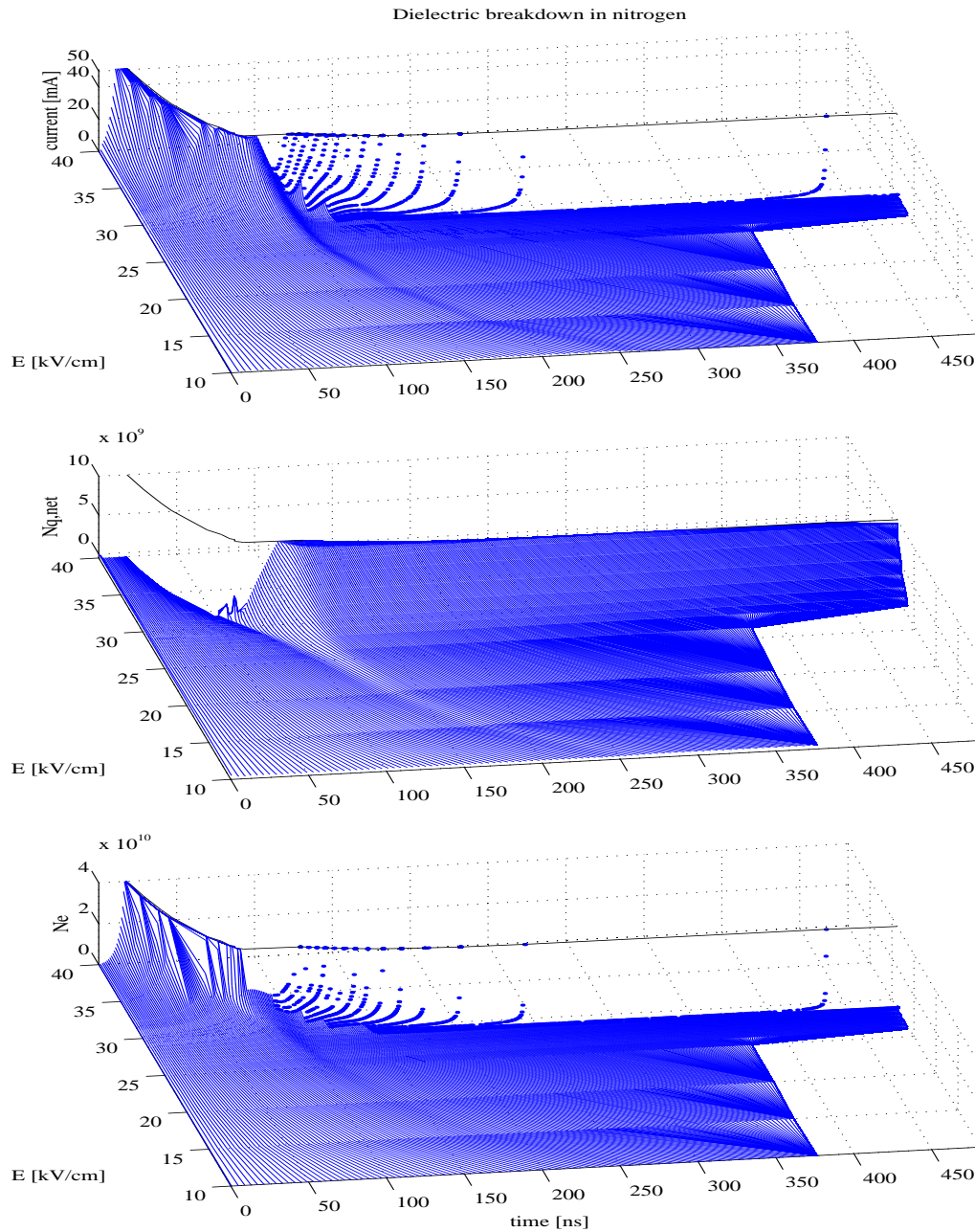


**Figure 6.3** Current  $i(t)$ , total net number of charge carriers  $N_{q,net}$  and number of electrons  $N_e$  as a function of time and applied field  $E$ .

To analyze the situation close to the transition between no breakdown and breakdown, the simulated particle density distributions are analyzed for  $E=30$  kV/cm and  $E=30.5$  kV/cm.

**Figure 6.4** shows the development of prebreakdown for  $N_0=4 \cdot 10^8$  electrons for  $E=30$  kV/cm (at which  $N_{0,min}=9 \cdot 10^7 < N_0 < N_{0,tr}=4.5 \cdot 10^8$ ), and  $E=30.5$  kV/cm (at which  $N_{0,tr}=3 \cdot 10^8 < N_0$ ). The electrical field is normalized to the applied Laplacian field.

The important role of the enhanced ionization, in the space charge modified electrical field, and gas phase photoionization for CDS formation and streamer propagation leading to breakdown can be observed from Fig.6.4, as well as the in section 4.3.2.2 discussed behaviour for the regimes in which  $N_{0,min} < N_0 < N_{0,tr}$  or  $N_{0,tr} < N_0$ .

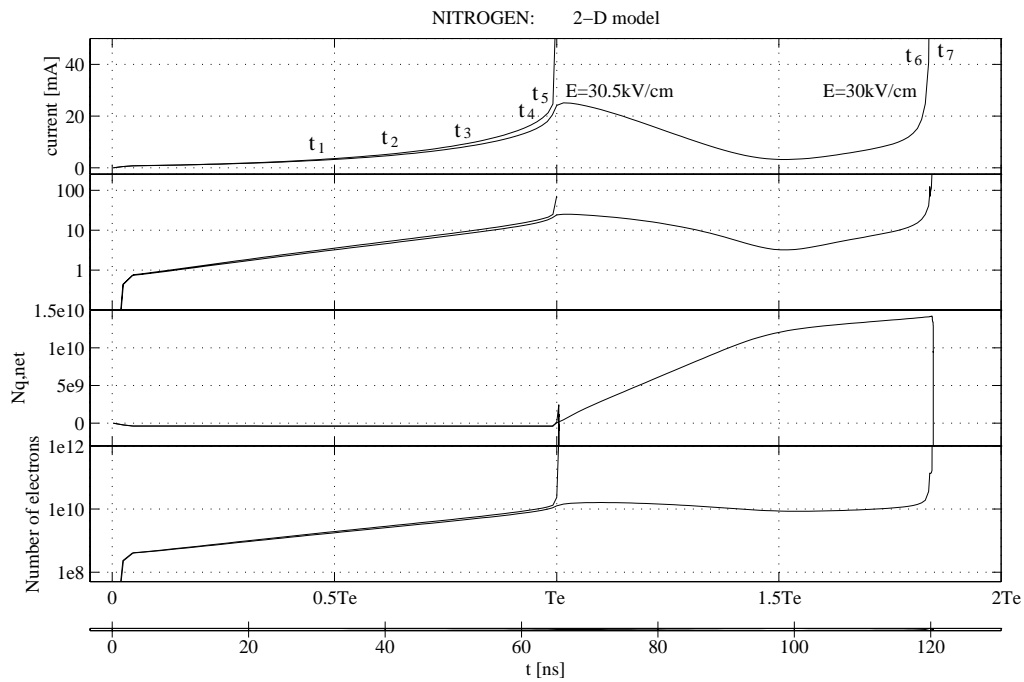


**Figure 6.4a** Simulated current waveforms ( $N_0=4 \cdot 10^8$ ).

Conditions: atmospheric nitrogen  $E=30.0-30.5$  kV/cm, gap=1 cm.

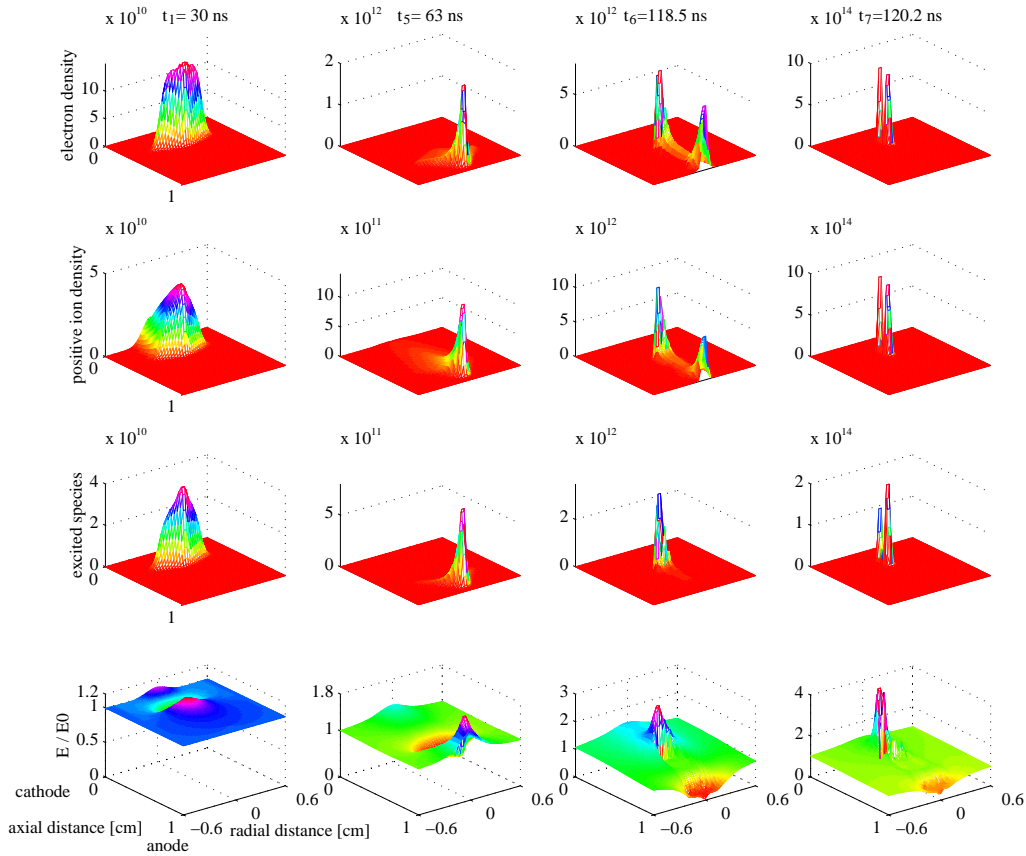


**Figure 6.4b** Simulated density of electrons, positive ions and excited species and resulting normalized electrical field at various time instances. ( $N_0=4 \cdot 10^8$ ).

Similar 3-D plots for  $E=30.5 \text{ kV/cm}$  are shown on the next page.

Conditions: atmospheric nitrogen  $E=30 \text{ kV/cm}$ , gap=1 cm.

For  $N_0 < N_{0,min}$  (as was shown in Fig.4.3) we find:

- \* No breakdown occurs.
- \* Immediately before the primary electron avalanche leaves the gap, the total field strength in the tail (at the cathode side) is still much smaller than in the electron avalanche's head. The secondary electron avalanche does not lead to breakdown and neither do the subsequent ones.

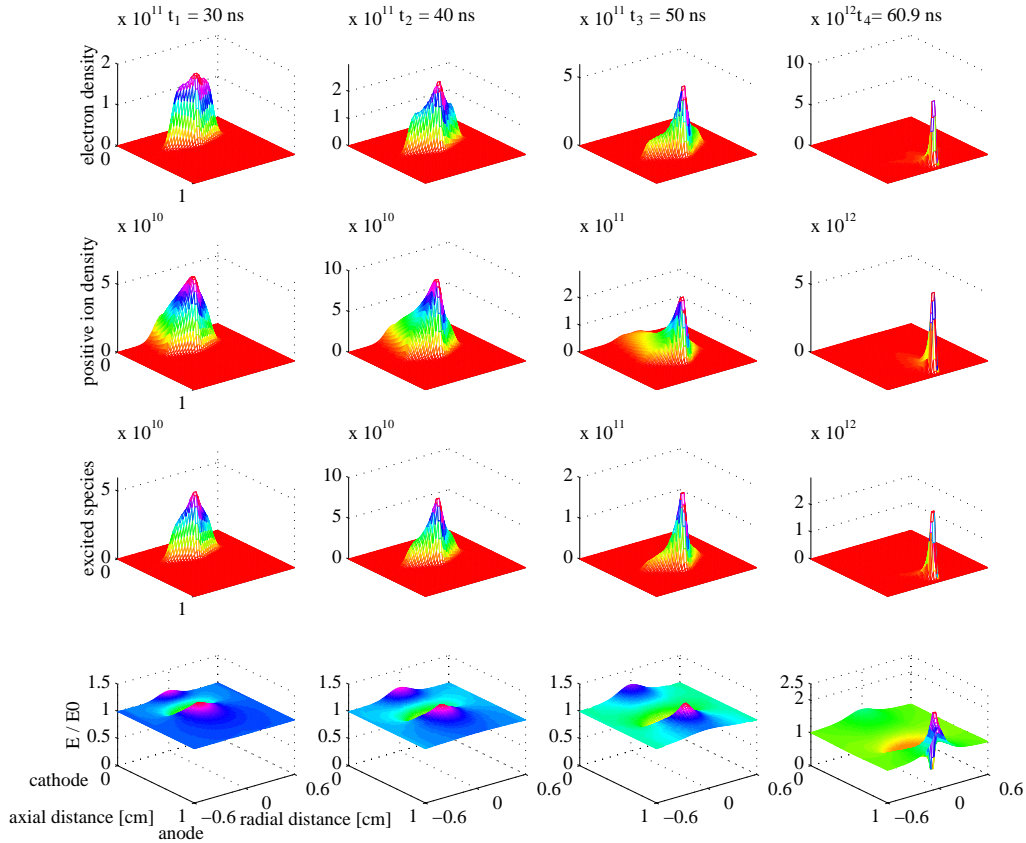


**Figure 6.4c** Simulated density of electrons, positive ions and excited species and resulting normalized electrical field at various time instances. ( $N_0=4 \cdot 10^8$ ).  
 Conditions: atmospheric nitrogen  $E=30.5 \text{ kV/cm}$ , gap=1 cm.

- \* At  $t \approx 110 \text{ ns}$  the "excited species density" (the source of photoionization) vanishes in the "mid-gap region", because the field strength becomes subcritical. Therefore there is no possibility anymore for the creation of a "cathode directed streamer" through released "delayed electrons".
- \* No CDS or ADS forms. No breakdown occurs.
- \* Only the positive ion density is observed. These positive ions slowly drift towards the cathode.

## 6.4 Parameter variations to identify relevant mechanisms

For the parameter variation study we artificially shut down one process and include all other processes\*\*\*\*. Thereby we can estimate the influence of this process and its relevance to the actual development of the various stages preceding breakdown. Hereby we can also conclude whether or not in the regime studied, a mechanism is of importance or may be neglected. We also check the influence of shutting down multiple processes.

We consider as tests:

- 1) the time-resolved current  $i(t)$
- 2) the total net number of charge carriers  $N_{q,net}(t)$
- 3) the total number of electrons  $N_e(t)$
- 4) the 3-D plots of the particle densities for various time instances.

### 6.4.1 Nitrogen

We compare the results with those of the full model in which all processes were included, i.e. the results shown in Fig.4.12 (conditions: atmospheric nitrogen,  $E=30.5 \text{ kV/cm}$ ,  $\text{gap}=1 \text{ cm}$ ,  $N_0=2 \cdot 10^8$ ). The reduction in simulation times by excluding various processes is shown in **Table 6.1**.

#### No source and loss terms

Shutting down the source and loss terms results in no ionization, so no growth, therefore this will never lead to an avalanche / streamer and therefore neither to gas breakdown. Without these we can only simulate propagation of particle density distributions. The source and loss terms are obviously relevant; excluding these reduces the simulation time by 63%.

#### No charge conservation integration test

By excluding the charge conservation integration test we also do no longer get output for the charge quantities. The simulation time decreases by 12% by excluding this procedure. The charge conservation integration test is included in normal runs, but is not relevant to the model outcome.

#### No space charge field

Without a space charge field no physically meaningful output results for the considered conditions, so this cannot be excluded. Excluding the space charge field calculation reduces the simulation time by 92%, a large reduction because the repeated field calculations are no longer done.

---

\*\*\*\* Remark: For situations in which space charge fields do not play a role, and which might therefore also be solved analytically, the simulation times are only shortened if the irrelevant algorithms/mechanisms are actually shut down.

**Table 6.1** Relevance of processes for the full 2-D model description of prebreakdown in nitrogen and dry air and reduction in simulation times by excluding processes or using optimizations.

Process	N <sub>2</sub>		Dry air	
	relevant	reduction in simulation time	relevant	reduction in simulation time
source and loss terms	yes	63%	yes	37%
charge conservation integration test	no	12%	no	0%
space charge field	yes	92%	yes	89%
optimization in the space charge field calculation speed	no	29%	no	38%
ion drift	no	48%	no	11%
electron diffusion	no	28%	no	2%
gas phase photoionization	yes	34%	yes	53%
secondary electron emission from surfaces by positive ion impact	yes	25%	yes	2%
secondary photoelectron emission from surfaces	yes	30%	yes	1%

#### **Optimization in the space charge field calculation speed**

Through the use of an optimization in the space charge field calculation speed, by only calculating the space charge field every second step, the simulation time can be shortened by 29% with (under most conditions) no significant influence on the output results. This optimization is included, but is not relevant to the model outcomes.

**No ion drift**

No influence is observed by excluding the ion drift velocity component, as could be expected at the nanosecond timescales considered because of the low ion drift velocity. Excluding the ion drift shortens the simulation time by 48%. The ion drift is not relevant under these conditions.

**No thermal electron diffusion**

No influence on the resulting 2-D model output quantities is seen when we shut down the thermal electron diffusion. Excluding the thermal electron diffusion shortens the simulation time by 28%.

**No gas phase photoionization**

Simulations have also been carried out neglecting photoionization. It results in a decrease in the time-to-breakdown  $t_{bd}$  from  $111\text{ ns}$  to  $65\text{ ns}$  and an incorrect resultant current waveform. In this case, the cathode directed motion resulting in a CDS is not observed. Excluding gas phase photoionization shortens the simulation time by 34%. For a proper description of streamer initiated gas breakdown gas phase photoionization cannot be excluded.

**No gas phase photoionization and no space charge field**

Some simplified models do not incorporate both gas phase photoionization and the space charge field. In this situation only avalanches are observed in the current  $i(t)$ , and as a result of the absence of streamer propagation no breakdown occurs, but to prove this it is needed to exclude the space charge field. The electron transit time  $T_e$  increases from  $65\text{ ns}$  to  $85\text{ ns}$  as could be expected in the absence of space charge. The simulation time is reduced by 95%.

**No cathode photoelectron emission**

This situation is simulated by neglecting excited species. No subsequent avalanches contribute to the initiation of breakdown. A streamer can still be formed due to gas phase photoionization. This however results in differences for times beyond the transit of the primary electron avalanche in comparison to the full model; the streamer structure is changed into a hollow cylinder shape. The streamer initiation occurs at  $t=280\text{ ns}$ . The time-to-breakdown  $t_{bd}$  strongly increases from  $111\text{ ns}$  to  $361\text{ ns}$ . Excluding cathode photoelectron emission shortens the simulation time by 30%.

**No cathode electron emission by positive ion impact**

This process is especially important when the CDS with all its positive ions approaches the cathode. For the situation in which cathode electron emission by positive ion impact was excluded multiple avalanche generations are distinguishable in the logarithmic plot of the current before breakdown. For the avalanche initiated prebreakdown it can be excluded but for the CDS initiated gas breakdown it cannot be excluded. Excluding cathode electron emission by positive ion impact reduces the simulation time by 25%.

### 6.4.2 Dry air

We compare the results to the full model in which all processes were included, i.e. the results shown in Fig.4.17 (conditions: atmospheric dry air,  $E=30$  kV/cm, gap=1 cm,  $N_0=4 \cdot 10^7$ ). The reduction in simulation times by excluding various processes is shown in Table 6.1.

#### **No source and loss terms**

Shutting down the source and loss terms results in no ionization, so no growth. Therefore this process is absolutely necessary for meaningful results. Without these we can only simulate propagation of particle density distributions. The source and loss terms are relevant, excluding these reduces the simulation time by 37%.

#### **No charge conservation integration test**

By excluding the charge conservation integration test we also do no longer get output for the charge quantities. Excluding this does not noticeably save time. The charge conservation integration test is included in normal runs, but is not relevant to the model outcome.

#### **No space charge field**

Without a space charge field no physically meaningful output results for the considered conditions, so this cannot be excluded. Excluding the space charge field calculation reduces the simulation time by 89%.

#### **Optimization in the space charge field calculation speed**

Through the use of an optimization in the space charge field calculation speed, the simulation time can be shortened by 38% with (under most conditions) no significant influence on the resulting 2-D model output quantities. This optimization is included, but is not relevant to the model outcome.

#### **No ion drift**

No influence is observed by excluding the ion drift velocity component, as could be expected at the nanosecond timescales considered because of the low ion drift velocity. Excluding the ion drift reduces the simulation time by 11%. The ion drift is not relevant under these conditions.

#### **No thermal electron diffusion**

No influence on the resulting 2-D model output quantities is seen when we shut down the thermal electron diffusion. Excluding thermal electron diffusion results in no significant reduction in simulation time.

**No gas phase photoionization**

Simulations have also been carried out neglecting photoionization. In this case, the current  $i(T_e)$  increases from 22 mA to 34 mA due to an increase in  $T_e$  from 51 ns to 64 ns, therefore also the time-to-breakdown  $t_{bd}$  increases from 65 ns to 80 ns. Excluding gas phase photoionization shortens the simulation time by 53%. The observed effect is different than in  $N_2$ . For a proper description of streamer initiated gas breakdown gas phase photoionization cannot be excluded.

**No gas phase photoionization and no space charge field**

Some simplified models do not incorporate both gas phase photoionization and the space charge field. The electron transit time  $T_e$  increases from 51 ns to 72 ns as could be expected in the absence of space charge. In this situation only avalanches are observed in the current  $i(t)$ , and as a result of the absence of streamer propagation no breakdown occurs, but to prove this it is needed to exclude the space charge field. Without a space charge field also the by detachment supplied "delayed electrons" cannot initiate streamer formation. So no breakdown occurs. The simulation time is reduced by 94%.

**No cathode photoelectron emission**

Excluding cathode photoelectron emission does not seem to have any significant influence on the gas breakdown under these conditions, indicating the importance of gas phase photoionization and detachment as dominant processes to the breakdown initiation in dry air. Excluding cathode photoelectron emission results in no significant reduction in simulation time.

**No cathode electron emission by positive ion impact**

No influence on the output results is seen under many conditions, though this process is especially important when the CDS approaches the cathode. Excluding cathode electron emission by positive ion impact results in no significant reduction in simulation time.

**No gas phase photoionization and no cathode photoelectron emission**

In this case, the current  $i(T_e)$  increases from 22 mA to 34 mA due to an increase in  $T_e$  from 51 ns to 64 ns. This however results in differences for times beyond the transit of the primary electron avalanche in comparison to the full model in dry air; a streamer could be formed due to detachment of electrons supplying "delayed electrons" to create an ADS. The time-to-breakdown  $t_{bd}$  increases from 65 ns to 81 ns. Cathode photoelectron emission is in addition to gas phase photoionization relevant. This could not be seen from the test of excluding solemnly the cathode photoelectron emission as was shown above. The simulation time is reduced by 54%.

If in this case also **cathode electron emission by positive ion impact** is excluded, the current maximum in  $i(t)$  is seen to occur at  $t=T_e$  and this results in no further reduction in simulation time.

### **No gas phase photoionization and no cathode electron emission by positive ion impact**

In this case, the current  $i(T_e)$  increases from 22 mA to 34 mA due to an increase in  $T_e$  from 51 ns to 64 ns. The time-to-breakdown  $t_{bd}$  increases from 65 ns to 80 ns. Excluding cathode electron emission by positive ion impact in addition to excluding gas phase photoionization does not result in a further reduction in simulation time. For a proper description of streamer initiated gas breakdown these processes are relevant.

From the above we can see:

- 1) What is needed for streamer formation and propagation, and how propagation can be stopped through quenching.
- 2) What the applied voltage's (applied field / driving external force) role is in influencing the streamers' behavior and propagation.
- 3) The total net number of positive charge carriers after the initial electrons have left the gap to result in a positive (plasma) column; its effect on the formation of streamers thereby initiating gas breakdown.
- 4) The role of electrons, positive ions and negative ions.

What else is there to be discovered from a fluid model description?

We can determine the electron temperatures, and by coupling the above (charged) species densities to a set of differential equations describing the chemical reactions we can obtain the various atomic and molecular (radical) species densities<sup>47</sup>.

A further improvement would be to include gas dynamic effects, so heating of the background gas. Such a complete model may help to further develop models valid at higher currents and later times (describing the arc phase in circuit-breakers).

In search for solutions to inherent problems in describing instabilities of streamers, more attention should also be addressed towards branching. In review of this a hypothesis for describing streamers from another point of view has been set up by Eber and Saarloos<sup>51,52</sup>.

## **6.5 Discussion on other modelling aspects**

The luminous fronts in a streamer are generally observed to propagate away from the evolving avalanche with speeds higher than the local mean-velocity at the avalanche boundaries<sup>60-63</sup>.

Such streamers should be considered as a subset of ionizing waves, propagating in an initially neutral background gas. For the explanation of the (cathode or anode directed) streamer dynamics, mechanisms are associated with:

- gas phase photoionization ahead of the avalanche by photons created by the avalanche
- the distribution in velocity of the electrons in the avalanche (electron drift respectively electron pressure) and possibly runaway electrons.

In a study on the kinetics of avalanche and streamer development Kunhardt and Tzeng<sup>35</sup>

discuss whether runaway electrons play a role<sup>\*\*\*\*\*</sup>. In this the dynamics of the electrons was simulated using a Monte-Carlo technique. For the considered time-scales the ions and neutrals were assumed stationary. This gave information on the role of the electron velocity distribution and gas phase photoionization in the formation of streamers and on the streamer properties like propagation speed and streamer radius.

*Single electron initiation, or a 1.5 ps electron distribution with 1500 electrons/ $8 \cdot 10^{-5} \text{ cm}^2$ , resulted in rather similar results, only differing in evolution time and time moment at which space charge effects set in. In the traversal towards the anode, the non-equilibrium distribution of the initial pulse rapidly evolved into a temporary state of dynamic equilibrium maintained by the external field and collisions with the background gas molecules. At first, the space charge field had little effect on the development of the avalanche, and the growth in the total number of electrons was exponential. As the population of charged particles increased, the electrons and ions start to shield the applied field from inside the avalanche. The total field decreased within the avalanche with an accompanied increase near the avalanche boundaries. This resulted in a net decrease in the rate of electron production, as we also observed. Therefore the growth in the total number of electrons starts to deviate from exponential current growth. The deviation from exponential growth decreases with increasing pressure. At high pressures, the decrease in the ionization rate in the center of the avalanche is compensated by the accompanied increase in the region of high field near the boundaries. At a background gas density of  $2 \cdot 10^{19} \text{ cm}^{-3}$ , the avalanche growth was nearly exponential for times up to the formation of streamers. This explains the success of earlier models for determining the breakdown time of overvolted gaps. In these simplified models, space charge effects were neglected and the growth of the number of electrons was taken to be exponential<sup>18,32</sup>.*

*At the time moment of anode directed streamer formation, the field near the head of the avalanche was approximately 1.3 times the Laplacian field value. The photoelectrons produced ahead of the avalanche rapidly multiply in this enhanced field. The boundary of the avalanche is extended towards the anode by the avalanche growth of these photoelectrons and not by the drift of the electrons at the boundary. The total number of electrons in the avalanche at this time moment was  $1.1 \cdot 10^8$ , which is in good agreement with the value of  $10^8$  that has been experimentally determined for these conditions<sup>63</sup>, and as was also found from our 2-D hydrodynamic model outcomes in section 4.3.2.2.. Photoelectrons created at the rear of the avalanche initiate the CDS. As the total field at the rear of the avalanche increases due to space charge (as also shown in Fig.6.4c at  $t=50 \text{ ns}$ ), these photoelectrons ionize efficiently and are pulled into the parent avalanche by the enhanced field. The concentration of electrons in the secondary avalanches at the cathode side was  $\approx 10^{14} \text{ particles/cm}^3$ , which was an order of magnitude higher than at the anode*

---

\*\*\*\*\* The quotations of Kunhardt and Tzeng are printed in italic.

*side. The CDS started to propagate step by step, due to the (in the Monte-Carlo particle description) avalanche growth of the few photoelectrons produced by the parent avalanche.*

The large field enhancement at the streamer tip is caused by its high ion density and small radius of curvature. Successive avalanches started by the photoelectrons generated by the first few secondary avalanches grow at a faster rate in this space charge enhanced field. The rate of photoelectron production also increases, so that the merger of successive avalanches produce a smoother profile. The propagation of the streamer is due to this rapid growth of the secondary (photoelectron) avalanches.

*The CDS had a diameter of approximately 50  $\mu\text{m}$ , while the ADS had a diameter of 100  $\mu\text{m}$ , which is around five times smaller than was found from our 2-D hydrodynamic model. These values increase with decreasing pressure. The velocities of the CDS and ADS were determined from the simulation data: the CDS was found to propagate at a lower velocity than the ADS (in the early stages the ADS was found to propagate at nearly twice the velocity of the CDS).*

Simulations were also carried out by Kunhardt and Tzeng<sup>35</sup> neglecting photoionization. The cathode directed motion of the avalanche was not observed, similar to the results of this thesis in Section 6.4. Under these conditions, space charge effects alone do not support CDS propagation. *Also, the anode-directed front was observed to propagate at a lower velocity. However, the velocity was a factor of 1.7 higher than the drift velocity in the enhanced field, indicating that space charge plays a role when photoionization is not included.*

*At an (artificially high) applied field of  $E/N=300$  Td (75 V/m·Pa), electrons in the avalanche did not gain sufficient energy to show runaway. Thus, runaways play no role in the propagation of the ADS at moderate values of  $E/N$ . Runaways were observed in nitrogen when the local value of  $E/N$  exceeded 1500 Td (375 V/m·Pa). At an applied  $E/N=1000$  Td (250 V/m·Pa) and in the absence of photoionization, the field at the head of the avalanche exceeded 1500 Td. Runaway electrons appeared and the velocity of the anode front increased considerably. However, when photoionization was included, the density profiles were less steep and the enhanced field at the head was below 1500 Td, runaway electrons were not observed and the front propagated at a lower velocity.*

Thus for  $E/N$  values of up to 1000 Td and in the presence of photoionization, runaway electrons were not observed, and the density profiles were sufficiently well behaved that a fluid description of the electron gas is justified.

In conclusion: the electron energy distribution function was relatively well-behaved in velocity space (i.e., no runaway electrons). It was shown it was possible to model the dynamics of avalanches and streamers with a proper set of fluid equations. Although electron kinetics determine the fine structure of the streamer fronts, the propagation of the streamers is due to the avalanche growth of the photoelectrons produced in the enhanced

fields near the streamer boundaries. These conclusions are supported by our 2-D model simulations which were found to give a good description of the measured phenomena. The properties of the streamers presented by Kunhardt and Tzeng<sup>35</sup> from a Monte-Carlo simulation at a background density of  $2 \cdot 10^{19} \text{ cm}^{-3}$  were consistent with experimental observations of luminosity tracks<sup>95</sup>. These results are also consistent with our ICCD images presented in Sections 4.2 and 4.3.

As a concluding remark: Leader formation (for long air gaps) involves a series of successive streamers (leader steps). The behavior of each of these streamers is similar to the role of streamers as described here in this thesis with the difference that they only bridge part of the gap in each step.



## Chapter 7

### Conclusions

*In this chapter the conclusions that can be drawn from the preceding chapters will be listed.*

From the above the following can be concluded for the investigations in  $N_2$  and **dry air** (without spacers):

- \* A strongly non-uniform avalanche structure is observed at very short camera exposure times. A strong radial expansion is observed during the primary avalanche's gap transition. This expansion is ascribed to an artifact of the experimental setup in creating photons outside the illuminated area through reflection of the  $N_2$ -laser beam at the anode and cathode surface thereby instantaneously releasing small numbers of additional electrons over a broader cathode region.
- \* The 2-D model correctly predicts (qualitatively and quantitatively) the externally measured current, as well as the discharge structure in the streamer phase.
- \* Very small variations in the initial conditions, at voltages just below the static breakdown voltage, cause large variations in the experimental current waveforms.
- \* In both nitrogen and dry air a large enough number of initial electrons and space charge effects can create conditions for "undervolted breakdown" (gas-breakdown below the static breakdown voltage).
- \* The differences with respect to dominant processes for prebreakdown and streamer formation in  $N_2$  and dry air:  
In addition to enhanced ionization in the space charge modified electrical field responsible for streamer propagation, for  $N_2$  gas phase photoionization supplies the delayed electrons responsible for streamer formation and propagation, whereas for dry air detachment of electrons from unstable ( $O^-$ ) negative ions is the dominant mechanism for supplying delayed electrons.
- \* Modelling of these processes yields more insight in the mechanisms responsible for streamer breakdown.
- \* The time-to-breakdown curves resulting from 2-D model simulations yield more insight in the parameter dependence of gas-breakdown and agree with literature data on impulse breakdown of air at atmospheric pressure.
- \* Differences in time-to-breakdown curves for dry air and nitrogen indicate a different discharge behavior; these fit the physical explanation of the occurring phenomena.

- \* A minimum critical electron number for streamer formation in nitrogen of  $9 \cdot 10^7$  electrons at  $30 \text{ kV/cm}$  and  $4 \cdot 10^7$  electrons at  $30.5 \text{ kV/cm}$  has been deduced from the 2-D model. These numbers are in agreement with data by Raether<sup>60,63</sup> and Loeb and Meek<sup>61,62</sup>.
- \* The physical model forms the basis for "engineering models" for practical geometries.

Application of the techniques to the description of physical discharge mechanisms in  $SF_6$ :

- \* In the experiments a strong radial expansion and a non-uniform avalanche structure are observed in the early avalanche phase, as was previously found from similar investigations for nitrogen and dry air. The models and insights for  $N_2$  and dry air are in principle applicable to  $SF_6$ .
- \* In  $SF_6$ , just as in dry air: 1) attachment is dominant in preventing breakdown at low electrical field strengths, 2) detachment is proposed as the dominant mechanism for streamer formation and 3) streamer propagation is governed by the enhanced ionization in the space charge modified electrical field and by gas phase photoionization.
- \* In this work the study of prebreakdown phenomena is extended to the study of atmospheric  $SF_6$ , in contrast to work by others on prebreakdown in  $SF_6$ .
- \* Future application of our 2-D model to  $SF_6$  would help to make progress in understanding prebreakdown phenomena in  $SF_6$ .

For **non-uniform fields** measurements of the optical activity related to prebreakdown phenomena in atmospheric  $SF_6$  yield the following observations:

- \* We observe corona-like discharges at voltages well below the dc breakdown field strengths and multiple sites of optical activity for larger laser-illuminated areas.
- \* For large electrode radii we observe different simultaneous discharge paths ("feathers").
- \* For sharp electrodes we observe only one path of optical activity.

From the present work on prebreakdown phenomena in **dry air along spacers** the following can be concluded:

- \* For larger dielectric constants  $\epsilon_r$  the gap breaks down partially along the spacer surface, and not just perpendicular to the electrode surface.
- \* Differences in time-to-breakdown curves for dry air with a spacer indicate a different discharge behavior. Localized field enhancement is proposed as the physical explanation of the occurring phenomena.
- \* The modification of the electric field by a spacer is dominating the discharge resulting in an increase/decrease of the breakdown field strength and of the time-to-breakdown.
- \* This is ascribed to the field distortion and (only in case of a cylindrical spacer) to surface trapping or detrapping processes.
- \* For other than cylindrical shapes the insulator surface itself seems to be playing a minor role on the prebreakdown behavior
- \* From the good reproducibility of the resulting breakdown voltages and the observed phenomena we conclude breakdown conditioning through surface charging is of minor importance under these conditions, in contrast to the situation in vacuum.<sup>100,101</sup>.

#### Application to **partial discharges in voids**:

The dielectric material influences the discharge characteristics:

- \* the dielectric constant  $\epsilon_r$  of the dielectric material influences the void field.
- \* the quantum yield for secondary-electrons from surfaces influences the inception field.
- \* Experiments show the  $q_{real} / E_{inc}$  ratio is independent of the dielectric material; this is due to field quenching.
- \* A "Paschen-like" empirical relation for partial discharges in voids in solid dielectrics has been assessed. The experimental studies have shown that the measured values for the inception voltage correspond well with calculated inception voltages based on the critical streamer criterion<sup>103</sup>. The trends of externally measurable PD quantities corresponds with those predicted by our simplified models.
- \* The hydrodynamic model provides a good qualitative description of the phenomena. Simulated and measured PD waveforms are in quantitative agreement. In order to overcome the shortcomings of the 1-D hydrodynamic model a 2-D model, including diffusion, has been developed. This led to a more correct simulated real charge value.

- \* Discharge mechanisms and material influences can be recognized from partial discharge current waveforms. Charge magnitude and inception voltage alone do not provide such detailed information.
- \* PTFE and polycarbonate both show a current waveform with a fast electron current component and an after current due to detachment, conversion processes and ions slowly moving in the quenched void field. This current behaviour depends on material and geometry.
- \* Measurements on voids with height dimensions below  $100\ \mu\text{m}$  (in the field direction) are possible. Measurements were made on voids with sizes down to  $10\ \mu\text{m}$  (note that real size voids are  $1\text{-}30\ \mu\text{m}$ ). As yet no indication of a smallest detectable void size was found.

Future work should be focused on a further investigation of PD-mechanisms and the ongoing development and application of more accurate models. Of major importance is the development of an "engineering model", relating measured quantities and void geometry, based on the insights gained from laboratory research and numerical models.

## Appendix A

### Data used in the 2-D model simulations

#### A.1 Swarm parameters

##### Nitrogen

Values for the ionization coefficient  $\alpha$ , the longitudinal electron diffusion coefficient  $D_{eL}$  and the electron drift velocity  $v_e$  are taken from Wen<sup>20</sup>. The data for the positive ion drift velocity  $v_p$  and the recombination coefficient  $\varepsilon_{pe}$  are from Badaloni and Gallimberti<sup>69</sup>, the transversal electron diffusion coefficient  $D_{eT}$  is from Dutton<sup>70</sup>.

Electron and positive ion drift velocities (cm/s)

$$\begin{aligned} v_e &= 3 \cdot 10^5 (E/p) & \text{for } E/p \leq 100 \text{ V/cm torr} \\ v_e &= 6 \cdot 10^6 + 2.4 \cdot 10^5 (E/p) & \text{for } 100 \text{ V/cm torr} < E/p \leq 300 \text{ V/cm*torr} \\ v_e &= 1.2 \cdot 10^7 + 2.2 \cdot 10^5 (E/p) & \text{for } 300 \text{ V/cm torr} < E/p \\ v_p &= 2 \cdot 10^3 (E/p) \end{aligned}$$

Transverse and longitudinal electron diffusion coefficient (cm<sup>2</sup>/s)

$$\begin{aligned} D_T &= 1.75 \cdot 10^4 (E/p^2) & \text{for } E/p \leq 60 \text{ V/cm torr} \\ D_T &= (v/p) (2 \cdot 10^2 + 2.3 (E/p)) & \text{for } 60 \text{ V/cm torr} < E/p \\ D_L &= 2.123 \cdot 10^5 / p & \text{for } E/p < 13 \text{ V/cm torr} \\ D_L &= 10^4 (E/p^2) & \text{for } 13 \text{ V/cm torr} \leq E/p < 50 \text{ V/cm torr} \\ D_L &= (6 \cdot 10^5 / p) + 6.353 \cdot 10^3 (E/p^2) & \text{for } 50 \text{ V/cm torr} \leq E/p < 220 \text{ V/cm torr} \\ D_L &= 10^4 (E/p^2) - (10^5 / p) & \text{for } 220 \text{ V/cm torr} \leq E/p \end{aligned}$$

Ionization coefficient (cm<sup>-1</sup>)

$$\begin{aligned} \alpha/p &= 0 & \text{for } E/p < 1 \text{ V/cm torr} \\ \alpha/p &= 4173.87 \exp[-446/(E/p)] & \text{for } 1 \text{ V/cm torr} \leq E/p \leq 27.78 \text{ V/cm torr} \\ \alpha/p &= 2.873 \exp[-243.392/(E/p)] & \text{for } 27.78 \text{ V/cm torr} < E/p \leq 36.36 \text{ V/cm torr} \\ \alpha/p &= 5.8019 \exp[-268.81/(E/p)] & \text{for } 36.36 \text{ V/cm torr} < E/p \leq 74.07 \text{ V/cm torr} \\ \alpha/p &= 10.335 \exp[-312.042/(E/p)] & \text{for } 74.07 \text{ V/cm torr} < E/p \end{aligned}$$

##### Dry air

Values for the stable negative ion detachment frequency  $k_{sd}$ , the conversion frequency  $k_c$ , the stable attachment coefficient  $\eta_s$ , the recombination coefficients  $\varepsilon_{pm}$  and  $\varepsilon_{pe}$ , and the stable and unstable negative ion drift velocities  $v_{sn,un}$  are taken from Badaloni and Gallimberti<sup>69</sup>. Values for the electron and positive ion drift velocities  $v_{e,p}$  are taken from Wen<sup>20</sup> and Novak and

Bartnikas<sup>41</sup>, respectively. For the ionization coefficient  $\alpha$ , in the range of  $31 < E/p < 45$  (V/cm torr) the data from Davies<sup>28</sup> is used, otherwise the data from Badaloni and Gallimberti<sup>69</sup> is used. For  $E/p < 25$  (V/cm torr) data for the unstable attachment coefficient is from Badaloni and Gallimberti<sup>69</sup>, otherwise along with the data for  $\alpha$  and  $\eta_s$ ,  $\eta_u$  determined from the experimental  $(\alpha - \eta_s - \eta_u)/p$  values from Wen<sup>20</sup>. The data for the unstable negative ion detachment frequency  $k_{ud}$  is from Badaloni and Gallimberti<sup>69</sup> but adjusted by a factor of two<sup>26</sup>. Furthermore, in the range  $30 < E/p < 50$  (V/cm torr)  $k_{ud}$  is adjusted to agree with Wen's<sup>20</sup>  $(\eta_s + \eta_u) \cdot D/p^2$ , where  $D = (k_{sd} + k_{ud})/v_e$ . The electron diffusion coefficients  $D_{eL}$  and  $D_{eT}$  are taken from Badaloni and Gallimberti<sup>69</sup>.

Electron, positive ion, stable and unstable negative ion drift velocities (cm/s)

$$\begin{aligned} v_e &= 10^6 (E/p)^{0.715} & \text{for } E/p \leq 100 \text{ V/cm torr} \\ v_e &= 1.55 \cdot 10^6 (E/p)^{0.62} & \text{for } 100 \text{ V/cm torr} < E/p \\ v_p &= 1.4 \cdot 10^3 (E/p) \\ v_{sn} &= 1.7 \cdot 10^3 (E/p) \\ v_{un} &= 3.3 \cdot 10^3 (E/p) \end{aligned}$$

Transverse and longitudinal electron diffusion coefficient (cm<sup>2</sup>/s)

$$D_T = D_L = 0.3483 v_e / (p \cdot \sqrt{E/p})$$

Ionization coefficient (cm<sup>-1</sup>)

$$\begin{aligned} \alpha/p &= \exp[(E/p) - 58.2]/4.95 & \text{for } E/p \leq 31 \text{ V/cm torr} \\ \alpha/p &= 3.8553 \exp[-213/(E/p)] & \text{for } 31 \text{ V/cm torr} < E/p \leq 45 \text{ V/cm torr} \\ \alpha/p &= \exp[\text{polynomial}(E/p)] & \text{for } 45 \text{ V/cm torr} < E/p \leq 250 \text{ V/cm torr} \\ \text{polynomial}(x=E/p) &= -64.927 + 5.2642x - 0.20238x^2 + 0.45178 \cdot 10^{-2}x^3 \\ & - 0.63081 \cdot 10^{-4}x^4 + 0.56724 \cdot 10^{-6}x^5 - 0.3278 \cdot 10^{-8}x^6 \\ & + 0.11739 \cdot 10^{-10}x^7 - 0.23661 \cdot 10^{-13}x^8 + 0.20479 \cdot 10^{-16}x^9 \\ \alpha/p &= 14.5 \exp[-356/(E/p)] & \text{for } 250 \text{ V/cm torr} < E/p \end{aligned}$$

Stable and unstable electron attachment coefficients (cm<sup>-1</sup>)

$$\begin{aligned} \eta_s &= 3.64 \cdot 10^{-3} p^{1.94} & \text{for } E/p \leq 0.6 \text{ V/cm torr} \\ \eta_s &= 1.426 \cdot 10^{-3} p^{1.94} (E/p)^{-1.834} & \text{for } 0.6 \text{ V/cm torr} < E/p \leq 10 \text{ V/cm torr} \\ \eta_s &= 3.94 \cdot 10^{-3} p^{1.94} (E/p)^{-2.277} & \text{for } 10 \text{ V/cm torr} < E/p \end{aligned}$$

$$\begin{aligned} \eta_u &= 0 & \text{for } E/p < 3 \text{ V/cm torr} \\ \eta_u/p &= 1.95 \exp[-60/(E/p)] (E/p)^{-1} & \text{for } 3 \text{ V/cm torr} \leq E/p < 25 \text{ V/cm torr} \\ \eta_u/p &= 2 \cdot 10^{-4} (E/p) + 2 \cdot 10^{-3} & \text{for } 25 \text{ V/cm torr} \leq E/p < 30 \text{ V/cm torr} \\ \eta_u/p &= 8 \cdot 10^{-3} & \text{for } 30 \text{ V/cm torr} \leq E/p \end{aligned}$$

Stable and unstable electron detachment frequencies ( $s^{-1}$ )

$$k_{sd}=0 \quad \text{for} \quad E/p \leq 10 \text{ V/cm torr}$$

$$k_{sd}=(8.73 \cdot 10^{-7}/p) \exp[388/(E/p)]^{-1} \quad \text{for} \quad 10 \text{ V/cm torr} < E/p$$

$$k_{ud}=0 \quad \text{for} \quad E/p \leq 10 \text{ V/cm torr}$$

$$k_{ud}=(1.6 \cdot 10^{-8}/p) \exp[322/(E/p)]^{-1} \quad \text{for} \quad 10 \text{ V/cm torr} < E/p \leq 30 \text{ V/cm torr and}$$

$$50 \text{ V/cm torr} < E/p$$

$$k_{ud}=v_e p (3 \cdot 10^{-4} (E/p) - 8.806 \cdot 10^{-3}) \quad \text{for} \quad 30 \text{ V/cm torr} < E/p \leq 50 \text{ V/cm torr}$$

Negative ion conversion frequency ( $s^{-1}$ )

$$k_c = 3.3 \cdot 10^{16} p \cdot A + 1.09 \cdot 10^{33} p^2 \cdot B$$

$$A = 10^{-18} \quad \text{for} \quad E/p < 20 \text{ V/cm torr}$$

$$6.6323 \cdot 10^{-32} (E/p)^{12.666} \quad \text{for} \quad 20 \text{ V/cm torr} \leq E/p < 30 \text{ V/cm torr}$$

$$6.7147 \cdot 10^{-17} (E/p)^{2.737} \quad \text{for} \quad 30 \text{ V/cm torr} \leq E/p < 100 \text{ V/cm torr}$$

$$2.35 \cdot 10^{-14} (E/p)^{1.465} \quad \text{for} \quad 100 \text{ V/cm torr} \leq E/p < 300 \text{ V/cm torr}$$

$$10^{-10} \quad \text{for} \quad 300 \text{ V/cm torr} \leq E/p$$

$$B = 10^{-30} \quad \text{for} \quad E/p < 10 \text{ V/cm torr}$$

$$8.78 \cdot 10^{-30} (E/p)^{-0.94342} \quad \text{for} \quad 10 \text{ V/cm torr} \leq E/p < 20 \text{ V/cm torr}$$

$$1.01 \cdot 10^{-25} (E/p)^{-4.0661} \quad \text{for} \quad 20 \text{ V/cm torr} \leq E/p < 30 \text{ V/cm torr}$$

$$6.65 \cdot 10^{-20} (E/p)^{-8} \quad \text{for} \quad 30 \text{ V/cm torr} \leq E/p < 40 \text{ V/cm torr}$$

$$10^{-35} \quad \text{for} \quad 40 \text{ V/cm torr} \leq E/p$$

## A.2 Data for secondary electron photon processes

### Gas phase photoionization<sup>68</sup>

**Nitrogen** (number of photoionizations at  $r'$  / (number of ionizing collisions at  $r$ ) sr cm torr)

$$\Psi = 2.5 \cdot 10^{-3} \exp[-0.6715 (|r-r'| p)] \quad \text{for} \quad |r-r'| p \leq 10 \text{ cm torr}$$

$$\Psi = 1.9 \cdot 10^{-5} (|r-r'| p)^{-1.43206} \quad \text{for} \quad 10 \text{ cm torr} < |r-r'| p \leq 100 \text{ cm torr}$$

$$\Psi = 4.7 \cdot 10^{-6} (|r-r'| p)^{-1.08541} \quad \text{for} \quad 100 \text{ cm torr} < |r-r'| p$$

**Dry air** (number of photoionizations at  $r'$  / (number of ionizing collisions at  $r$ ) sr cm torr)

$$\Psi = 7.145 \cdot 10^{-4} \quad \text{for} \quad |r-r'| p \leq 100 \text{ cm torr}$$

$$\Psi = 5.463 \cdot 10^{-2} (|r-r'| p)^{-2.23619} \quad \text{for} \quad 100 \text{ cm torr} < |r-r'| p \leq 300 \text{ cm torr}$$

$$\Psi = 21.469 (|r-r'| p)^{-3.30483} \quad \text{for} \quad 300 \text{ cm torr} < |r-r'| p$$

### Photoelectron emission from the cathode surface

The values for  $p_{qm}$ ,  $\tau_m$ ,  $\mu_m$  and  $\delta_m$  for both  $N_2$  and dry air are assumed to be that representative of the 2<sup>nd</sup> positive system ( $C^3\Pi_u$ - $B^3\Pi_g$ ) for the  $N_2$  molecule<sup>84,86,97,98</sup>. In addition we assume an integrated excitation coefficient  $\delta_m \rightarrow \delta$  to the  $C^3\Pi_u$  electronic state. We represent the properties of this state by a single time constant and quenching pressure, and of energy 3.5 eV above that off the  $B^3\Pi_g$  electronic state (the use of the 2<sup>nd</sup> positive system is only an approximation).

The ionization reduced excitation coefficient is given by

$$\frac{\delta}{\alpha} = 0.101 + 268\left(\frac{E}{p}\right)^{-1} - 353.4 \cdot 10^2 \left(\frac{E}{p}\right)^{-2} + 547.3 \cdot 10^4 \left(\frac{E}{p}\right)^{-3} - 160.5 \cdot 10^6 \left(\frac{E}{p}\right)^{-4} + 212.4 \cdot 10^7 \left(\frac{E}{p}\right)^{-5}$$

From the quenching pressures and the unquenched lifetime  $\tau_{qm} = 36$  ns for the electronic state the resulting lifetimes  $\tau_m$ , of the  $C^3\Pi_u$  excitation level at atmospheric pressure result from

$$\tau_m = \frac{p_{qm}}{p + p_{qm}} \tau_{qm}$$

Initially, it was assumed by Kennedy<sup>19</sup> that the background gas was transparent to 3.5 eV photons thus setting  $\mu_m$  equal to zero. In later simulations extrapolated data from Penney and Hummert<sup>68</sup> for nitrogen and dry air, combined with data by Badeloni and Gallimberti<sup>69</sup> for  $N_2 / O_2$  mixtures for the absorption coefficients  $\mu_m$  in the band 12.0 eV to 14.0 eV, showed the contribution to photoelectron emission from surfaces to mainly result from 12.25 eV excitation. In this, summation of the contributions of photoionization efficiency  $\eta_m$ , the photon production efficiency  $\omega_m$  and the absorption coefficient  $\mu_m$  for the m<sup>th</sup> electronic level according to (5.11) in Badeloni and Gallimberti<sup>69</sup> was used to obtain this result of an integrated value for the absorption coefficient  $\mu_m$ .

The quantum efficiency  $Q$  has been estimated to be  $3 \cdot 10^{-4}$  electrons/photon for both  $N_2$  and air<sup>19</sup>.

#### Nitrogen

$$p_{qm} = 60 \text{ torr}$$

$$\tau_m = 2.6 \text{ ns}$$

$$\mu_m = 5.3 \text{ cm}^{-1}$$

#### Dry air

$$p_{qm} = 10 \text{ torr}$$

$$\tau_m = 0.47 \text{ ns}$$

$$\mu_m = 4.6 \text{ cm}^{-1}$$

## Bibliography

- [1] Wetzer, J.M.  
Kennedy, J.T.  
Gaxiola, E.H.R. "A Time-Dependent Model of Partial Discharges in Voids".  
7<sup>th</sup> International Symposium on Gaseous Dielectrics, Knoxville, TN, USA,  
April 1994.  
In: "Gaseous Dielectrics VII". Editors: L.G. Christophorou and J.K. Olthoff,  
pp.231-237, Plenum Press, 1995
- [2] Wetzer, J.M.  
Kennedy, J.T.  
Gaxiola, E.H.R. "A Time-Resolved Study of the Physical Processes Governing Void  
Discharges".  
1994 Conference on Electrical Insulation and Dielectric Phenomena,  
1994 Annual Report, Arlington, Texas, USA, pp.85-90, October 1994
- [3] Gaxiola, E.H.R.  
Wetzer, J.M. "The Influence of Dielectric Material on Partial Discharges in Voids".  
9<sup>th</sup> International Symposium on High Voltage Engineering, Graz, Austria,  
Vol.5, Paper No.5646, pp.1-4, August 28<sup>th</sup> to September 1<sup>st</sup>, 1995
- [4] Gaxiola, E.H.R.  
Wetzer, J.M. "Partial Discharge Detection in Insulators; Scaling Relationships and  
Practical Implications".  
11<sup>th</sup> International Conference on Gas Discharges and Their Applications,  
Tokyo, Japan, Vol.2, pp.226-229, September 11<sup>th</sup> to September 15<sup>th</sup>, 1995
- [5] Gaxiola, E.H.R.  
Wetzer, J.M. "Partial Discharges in Micrometer Voids in PTFE".  
1996 IEEE International Symposium on Electrical Insulation, Montréal,  
Québec, Canada, Vol.1, pp.420-423, June 1996
- [6] Gaxiola, E.H.R.  
Wetzer, J.M. "A Time-Resolved Optical Study of the Avalanche and Streamer Formation  
in Atmospheric Nitrogen".  
1996 IEEE International Symposium on Electrical Insulation, Montréal,  
Québec, Canada, Vol.2, pp.793-796, June 1996
- [7] Gaxiola, E.H.R.  
Wetzer, J.M. "Avalanch and Streamer Formation in N<sub>2</sub> and Dry-Air".  
IEE Seventh International Conference on Dielectric Materials, Measurements  
and Applications, Bath, United Kingdom, Conf.Publ.No.430, pp.116-119,  
September 1996
- [8] Gaxiola, E.H.R.  
Wetzer, J.M. "Partial Discharge Modelling and Measurements on Micrometer Voids in  
Solid Dielectrics".  
IEE Seventh International Conference on Dielectric Materials, Measurements  
and Applications, Bath, United Kingdom, Conf.Publ.No.430, pp.322-325,  
September 1996

- [9] Gaxiola, E.H.R. "Vorming van Streamers in Stikstof en Lucht".  
Energietechniek, jaargang 75, pp.25-27, Januari 1997
- [10] Gaxiola, E.H.R.  
Wetzer, J.M. "Optical & Electrical Study of the Avalanche and Streamer Formation in Sulfurhexafluoride".  
10<sup>th</sup> International Symposium on High Voltage Engineering, Montréal, Québec, Canada, Vol.2, pp.293-296, August 1997
- [11] Gaxiola, E.H.R.  
Wetzer, J.M. "A Study of Streamer Formation in Nitrogen".  
12<sup>th</sup> International Conference on Gas Discharges and Their Applications, Greifswald, Germany, Vol.1, pp.232-235, September 8<sup>th</sup> - 12<sup>th</sup>, 1997
- [12] Gaxiola, E.H.R.  
Wetzer, J.M. "A Study of Streamer Formation in Dry Air".  
12<sup>th</sup> International Conference on Gas Discharges and Their Applications, Greifswald, Germany, Vol.1, pp.236-239, September 8<sup>th</sup> - 12<sup>th</sup>, 1997
- [13] Gaxiola, E.H.R.  
Wetzer, J.M. "A Study of Prebreakdown in SF<sub>6</sub>".  
8<sup>th</sup> International Symposium on Gaseous Dielectrics, Virginia Beach, Virginia, U.S.A., June 2<sup>nd</sup> to June 5<sup>th</sup>, 1998  
In: "Gaseous Dielectrics VIII". Editors: L.G. Christophorou and J.K. Olthoff, pp.105-110, Plenum Press, 1999
- [14] Gaxiola, E.H.R.  
Wetzer, J.M. "Prebreakdown Phenomena in Dry Air along PTFE Spacers".  
8<sup>th</sup> International Symposium on Gaseous Dielectrics, Virginia Beach, Virginia, U.S.A., June 2<sup>nd</sup> to June 5<sup>th</sup>, 1998  
In: "Gaseous Dielectrics VIII". Editors: L.G. Christophorou and J.K. Olthoff, pp.511-516, Plenum Press, 1999
- [15] Gaxiola, E.H.R.  
Wetzer, J.M. "Prebreakdown Phenomena in Insulating Gases; Evaluation of the Time-to-Breakdown".  
1998 IEEE International Symposium on Electrical Insulation, Washington, D.C., U.S.A., Vol.2, pp.693-696, June 7<sup>th</sup> to June 10<sup>th</sup>, 1998
- [16] Christophorou, L.  
Olthof, J.K.  
Green, D.S. "Gases for Electrical Insulation and Arc Interruption: Possible Present and Future Alternatives to Pure SF<sub>6</sub>".  
National Institute of Technology, NIST Technical Note 1425, 1997
- [17] Klein, M. "Barrierentladungen zur Entstickung motorischer Abgase".  
Dissertation, Universität Fridericiana Karlsruhe, Karlsruhe, Germany, 1995
- [18] Blom, P.P.M. "High-Power Pulsed Corona".  
Ph.D. thesis, Eindhoven Univ. of Techn., Eindhoven, The Netherlands, 1997
- [19] Kennedy, J.T. "Study of the Avalanche to Streamer Transition in Insulating Gases".  
Ph.D. thesis, Eindhoven Univ. of Techn., Eindhoven, The Netherlands, 1995

- [20] Wen, C. "Time-Resolved Swarm Studies in Gases with Emphasis on Electron Detachment and Ion Conversion".  
Ph.D. thesis, Eindhoven Univ. of Techn., Eindhoven, The Netherlands, 1989
- [21] Verhaart, H.F.A. "Avalanches in Insulating Gases".  
Ph.D. thesis, Eindhoven Univ. of Techn., Eindhoven, The Netherlands, 1982
- [22] Davies, A.J.  
Davies, C.S.  
Evans, C.J. "Computer Simulation of Rapidly Developing Gaseous Discharges".  
Proceedings of the IEE, Vol.118, No.6, pp.816-823, 1971
- [23] Kline, L.E.  
Siambis, J.G. "Computer Simulation of Electrical Breakdown in Gases; Avalanches and Streamer Formation".  
Physical Review A, Vol.5, No.2, pp.794-805, 1972
- [24] Reininghaus, W. "Calculation of Streamers in Gaseous Discharges".  
Journal of Physics D: Applied Physics, Vol.6, pp.1486-1493, 1973
- [25] Bayle, P.  
Bayle, M. "Simulation of Secondary Processes in Breakdown in Air".  
Zeitschrift für Physik, Vol.266, pp.275-281, 1974
- [26] Kline, L.E. "Effect of Negative Ions on Current Growth and Ionizing Wave Propagation in Air".  
Journal of Applied Physics, Vol.46, No.5, pp.1994-2000, 1975
- [27] Marode, E. "The Mechanism of Spark Breakdown in Air at Atmospheric Pressure between a Positive Point and a Plane. I. Experimental: Nature of the Streamer Track. II. Theoretical: Computer Simulation of the Streamer Track".  
Journal of Applied Physics, Vol.46, No.5, pp.2005-2015 2016-2020, 1975
- [28] Davies, A.J.  
Evans, C.J.  
Townsend, P.  
Woodison, P.M. "Computation of Axial and Radial Development of Discharges between Plane Parallel Electrodes".  
Proc. IEE, Vol.124, No.2, pp.179-182, 1977
- [29] Zalesak, S.T. "Fully Multidimensional Flux-Corrected Transport Algorithms for Fluids".  
Journal of Computational Physics, Vol. 31, pp.335, 1979
- [30] Gallimberti, I. "The Mechanism of the Long Spark Formation".  
Journ. de Physique, Vol.40, pp.193-250, 1979
- [31] Abbas, I.  
Bayle, P. "Non-Equilibrium between Electrons and Field in a Gas Breakdown Ionising Wave: I. Macroscopic Model. II. Structure of the Leading Edge".  
Journal of Physics D: Applied Physics, Vol.14, pp.649-660 661-674, 1981

- [32] Llewelyn-Jones, F. "Numerical Solution of Hyperbolic Equations for Electron Drift in Strongly Non-Uniform Electric Fields".  
Journal of Computational Physics, Vol.43, pp.1-15, 1981
- [33] Morrow, R. "Electrical Breakdown and Discharges in Gases".  
NATO ASI Series, Editors: E.E. Kunhardt and L.H. Tuessen, Vol.89a, Plenum Press, New York, pp.1-89, 1983
- [34] Dhali, S.K.  
Williams, P.F. "Numerical Simulation of Space-Charge-Controlled Transport".  
Proceedings of the 4<sup>th</sup> IEEE Pulsed Power Conference, Albuquerque, New Mexico, U.S.A., pp.227-230, 1983
- [35] Kunhardt, E.E.  
Tzeng, Y. "Kinetic Investigation of Avalanche and Streamer Development".  
In: "Gaseous Dielectrics IV". Editors: L.G. Christophorou and M.O. Pace, pp.146-153, Pergamon Press, New York, 1984
- [36] Kline, L.E. "Monte Carlo Study of Ionization Zone Electron Kinetics in Negative Pin-Plane Coronas in Air".  
Journal of Applied Physics, Vol.58, No.10, pp.3715-3719, 1985
- [37] Kunhardt, E.E.  
Wu, C. "Towards a More Accurate Flux Corrected Transport Algorithm".  
Journal of Computational Physics, Vol.8, pp.127-150, 1987
- [38] Dhali, S.K.  
Williams, P.F. "Two-dimensional studies of streamers in gases".  
Journal of Applied Physics, Vol.62, No.12, pp.4696-4707, 1987
- [39] Wu, C.  
Kunhardt, E.E. "Formation and Propagation of Streamers in N<sub>2</sub> and SF<sub>6</sub> mixtures".  
Physical Review A, Vol.37, pp.4396, 1988
- [40] Satoh, K.  
Tagashira, H.  
Sakamoto, S. "Electron Swarm Development in SF<sub>6</sub>: I. Boltzmann Equation Analysis.  
II. Monte Carlo Simulation".  
Journal of Applied Physics D, Vol.21, pp.922-930 931-936, 1988
- [41] Novak, J.P.  
Bartnikas, R. "Short Gap Breakdown: 2-D model for Air".  
Proceedings of the Tenth International Conference on Gas Discharges and Their Applications, Vol.2, pp.864-867, 1992
- [42] Boris, J.P.  
Landsberg, E.M.  
Oran, E.S.  
Gardner, J.H. "LCPFCT - A Flux Corrected Algorithm for Solving Generalized Continuity Equations".  
Naval Research Lab., Dept. of Navy, NRL/MR/6410-93-7192, 1993
- [43] Guo, J.M.  
Wu, C.H.J. "Two-dimensional nonequilibrium fluid models for streamers".  
IEEE Trans. on Plasma Science, Vol.21, pp.684-695, 1993

- [44] Kurrat, M. "Modellierung und Messung von Teilentladungen in Hohlräumen zur Bestimmung schädigungsrelevanter Energien". Dissertation, Universität Dortmund, Dortmund, Germany, 1993
- [45] Kulikovski, A.A. "The Structure of Streamers in  $N_2$ . I: Fast Method of Space Charge Dominated Plasma Simulation". Journal of Physics D: Appl. Physics, Vol.27, pp.2556-2563 2564-2569, 1994
- [46] Kulikovski, A.A. "Two-Dimensional Simulation of the Positive Streamer in  $N_2$  between Parallel-Plate Electrodes". Journal of Physics D: Applied Physics, Vol.28, pp.2483-2493, 1995
- [47] Djemoune, D.  
Samson, S.  
Marode, E.  
Ségur, P. "A time resolved two dimensional modelling of the electrical behaviour and the chemical yield of streamer induced discharge". 11<sup>th</sup> Int. Conf. on Gas Discharges and Their Applications, Tokyo, Japan, Vol.2, pp.484-487, September 11 to September 15, 1995
- [48] Loiseau, J.F.  
Grangé, F.  
Spyrou, N.  
Held, B. "Laser-Induced Space Charge Initiating a Corona Discharge: Numerical Simulation and Comparison with Experiment". 11<sup>th</sup> Int. Conf. on Gas Discharges and Their Applications, Tokyo, Japan, Vol.2, pp.492-295, September 11 to September 15, 1995
- [49] Held, B. "Coronas and Their Applications". 11<sup>th</sup> Int. Conf. on Gas Discharges and Their Applications, Tokyo, Japan, Vol.2, pp.514-526, September 11 to September 15, 1995
- [50] Babaeva, N. Yu.  
Naidis, G.V. "Two-Dimensional Modelling of Positive Streamer Dynamics in Non-Uniform Electric Fields in Air". Journal of Physics D: Applied Physics, Vol.29, pp.2423-2431, 1996
- [51] Ebert, U.  
Saarloos, W.  
Caroli, C. "Streamer Propagation as a Pattern Formation Problem: Planar Fronts". Physical Review Letters, Vol.77, No.20, pp.4178-4181, 1996
- [52] Ebert, U.  
Saarloos, W.  
Caroli, C. "Propagation and Structure of Planar Streamer Fronts". Physical Review E, Vol.55, No.2, pp.1530-1549, 1997
- [53] Morrow, R.  
Lowke, J.J. "Streamer Propagation in Air". Journal of Physics D: Applied Physics, Vol.30, pp.614-627, 1997
- [54] Kulikovski, A.A. "The Mechanism of Positive Streamer Acceleration and Expansion in Air in a Strong External Field". Journal of Physics D: Applied Physics, Vol.30, pp.1515-1522, 1997

- [55] Engel, K. "Bewertung von Teilentladungen in Spaltförmigen Isolierstoffdefekten". Dissertation, Universität Dortmund, Dortmund, Germany, 1998
- [56] Meek, J.M.  
Craggs, J.D. "Electrical Breakdown of Gases". John Wiley & Sons, New York, U.S.A., 1978
- [57] Kuffel, E.  
Zaengl, W.S. "High Voltage Engineering". Pergamon Press, New York, U.S.A., 1984
- [58] Petcheraks, K. "Applicability of the Streamer Breakdown Criterion to Inhomogeneous Gas Gaps". Ph.D. thesis, Swiss Federal Institute of Technology, Zürich, Switzerland, 1995
- [59] Townsend, J.S. "The Theory of Ionization of Gases by Collision". Constable & Co. Ltd., London, U.K., 1910
- [60] Raether, H. "Die Entwicklung der Elektronenlawine in den Funkenkanal." Zeitschrift für Physik, Vol.112, pp.464-489, 1939
- [61] Loeb, L.B.  
Meek, J.M. "The Mechanism of Spark Discharge in Air at Atmospheric Pressure. I II" Journal of Applied Physics, Vol.11, pp.438-447 459-474, 1940
- [62] Loeb, L.B. "Basic Processes of Gaseous Electronics". University of California Press, Berkeley, U.S.A., 1955
- [63] Raether, H. "Electron Avalanches and Breakdown in Gases". Butterworths, London, U.K., sections 2.1 and 5.2.1, 1964
- [64] Rees, J.A. "Electrical Breakdown in Gases". Macmillan, London, U.K., 1973
- [65] Penning, F.M. "De elementaire Processen bij de Doorslag van Gassen tusschen Vlakke Evenwijdige Platen". Nederlands Tijdschrift voor Natuurkunde, Vol.5, No.33, pp.33-56, 1938
- [66] Llewellyn Jones, F. "Ionization and Breakdown of Gases". Methuen, London, 1966
- [67] Nasser, E. "Ionization and Plasma Electronics". Chapter 9, Sections 9.2-9.4, Wiley, New York, U.S.A., 1971
- [68] Penney, G.W.  
Hummert, G.T. "Photoionization Measurements in Air, Oxygen and Nitrogen". Journal of Applied Physics, Vol.41, No.2, pp.572-577, 1970

- [69] Badaloni, S.                    "Basic Data of Air Discharges".  
Gallimberti, I.                    Upee-72/05, Universitea Padova, Padova, Italy, 1972
- [70] Dutton, J.                        "A Survey of Electron Swarm Data".  
Journal of Physical Chemical Reference Data, Vol.4, No.3, pp.577-856, 1975
- [71] Bruce, F.M.                      "Calibration of Uniform-Field Spark Gaps for High Voltage Measurements  
at Power Frequencies".  
Journal IEE, Vol.94, Part II, pp.138, 1947
- [72] Shockley, W.                     "Currents to Conductors Induced by a Moving Point Charge".  
Journal of Applied Physics, Vol.9, pp.635-636, 1938
- [73] Ramo, S.                         "Currents Induced by Electron Motion".  
Proceedings IRE, Vol.27, pp.584-585, 1939
- [74] Wetzer, J.                        "Prebreakdown Currents. Basic Interpretation and Time-Resolved  
Laan, P. v.d.                        Measurements".  
IEEE Trans. on El. Ins., Vol.24, No.2, pp.297-308, 1989
- [75] Wetzer, J.M.                      "Bandwidth Limitations of Gap Current Measurements"  
Wen, C.                              1988 IEEE International Symposium on Electrical Insulation, Boston,  
Laan, P.C.T. v.d.                    U.S.A., pp.355-358, June 1988
- [76] Patel, B.S.                        "Compact High-Power TEA N<sub>2</sub> Laser".  
Review of Scientific Instruments, Vol.49, No.9, pp.1361-1363, 1978
- [77] Greinacher, H.                    "Erzeugung einer Gleichspannung vom vielfachen Betrage einer  
Wechselspannung ohne Transformator".  
Bull. SEV, Vol.11, pp.59-66, 1920
- [78] Schäfer, K.                      "Eigenschaften der Material in ihren Aggregatzuständen".  
Zahlenwerte und Functionen aus Physik, Chemie, Astronomie, Bd.2,  
Springer Verlag, Berlin, Germany, 1959
- [79] Trichel, G.W.                    "The Mechanism of the Positive Point-to-Plane Corona in Air at  
Atmospheric Pressure".  
Physical Review, Vol.55, pp.382-390, 1939
- [80] Gravendeel, B.                    "Negative Corona Discharges; a Fundamental Study".  
Ph.D. thesis, Eindhoven Univ. of Techn., The Netherlands, pp.9-20,  
pp.143-145, 1987

- [81] Pfeiffer, W.  
Schön, D.  
Zender, C. "Dielectric Characteristics of SF<sub>6</sub> - N<sub>2</sub> Mixtures for Very Fast Transient Voltages".  
8<sup>th</sup> International Symposium on Gaseous Dielectrics, Virginia Beach, Virginia, U.S.A., June 2<sup>nd</sup> to June 5<sup>th</sup>, 1998  
In: "Gaseous Dielectrics VIII", Editors: L.G. Christophorou and J.K. Olthoff, Plenum Press, 1999
- [82] Kennedy, J.T.  
Wetzer, J.M. "Air Breakdown in Under-Volted Gaps Time-Resolved Electrical & Optical Experiments".  
9<sup>th</sup> International Symposium on High Voltage Engineering, Graz, Austria, Vol.2, Paper No.2153, pp.1-4, August 28<sup>th</sup> to September 1<sup>st</sup>, 1995
- [83] Koppitz, J. "Image Converter and Intensifier Investigations on Luminous Fronts (Ionizing Waves) in Nitrogen Discharges in a Homogeneous Field".  
Zeitschrift für Naturforschung, Vol.26a, pp.700-706, 1971
- [84] Saxe, R.F. Uniform Field Breakdown in Air".  
British Journal of Applied Physics, Vol.7, pp.336-340, 1956
- [85] Tholl, H. "Der Einfluß der Eigenraumladung auf die Trägervermehrung einer Lawine in N<sub>2</sub>, CH<sub>4</sub> und N<sub>2</sub> + CH<sub>4</sub>".  
Zeitschrift für Physik, Vol.172, pp.536-555, 1963
- [86] Allen, K.R.  
Phillips, K. "A Study of the Light Emitted from the Initial Stages of a Spark Discharge".  
Proceedings of the Royal Society of London, Vol.278, pp.168-187, 1964
- [87] Wagner, K.H. "Die Entwicklung der Elektronenlawine in den Plasmakanal, untersucht mit Bildverstärker und Wischverschluß".  
Zeitschrift für Physik, Vol.189, pp.465-515, 1966
- [88] Wagner, K.H. "Vorstadium des Funkens, untersucht mit dem Bildverstärker".  
Zeitschrift für Physik, Vol.204, pp.177-197, 1967
- [89] Koppitz, J. "Die Radiale und Axiale Entwicklung des Leuchtens im Funkenkanal, untersuchung mit einer Wischkamera".  
Zeitschrift für Naturforschung, Vol.22a, No., pp.1089-1097, 1967
- [90] Doran, A.A. "The Development of a Townsend Discharge in N<sub>2</sub> up to Breakdown Investigated by Image Converter, Intensifier and Photomultiplier Techniques".  
Zeitschrift für Physik, Vol.208, pp.427-440, 1968
- [91] Haydon, S.C. "Spark Channels".  
Proceedings 8<sup>th</sup> International Conference on Phenomena in Ionized Gases, Vienna, Invited Papers, pp.495-518, 1967

- [92] Cavenor, M.C.  
Meyer, J. "The Development of Spark Discharges in Hydrogen".  
Australian Journal of Physics, Vol.22, pp.155-167, 1969
- [93] Tholl, H. "Thermalisierung und zeitlich Entwicklung der Elektronendichte und  
Temperatur von Funkenkanälen in Wasserstoff".  
Zeitschrift für Naturforschung, Vol.25a, pp.420-429, 1970
- [94] Chalmers, I.D.  
Duffy, H.  
Tedford, D.J. "The Mechanism of Spark Breakdown in Nitrogen, Oxygen and Sulphur  
Hexafluoride".  
Proceedings of the Royal Society of London A, Vol.329, pp.171-191, 1972
- [95] Bayle, M.  
Bayle, P.  
Crokaert, M. "The Development of Breakdown in a Homogeneous Field at High  
Overvoltages in Helium-Neon Mixtures and Nitrogen".  
Journal of Applied Physics, Vol.8, pp.2181-2189, 1975
- [96] Fletcher, R.C. "Impulse Breakdown in the  $10^{-9}$ -Sec. Range of Air at Atmospheric Pressure".  
Physics Review, Vol.76, No.10, pp.1501-1511, 1949
- [97] Legler, W. "Anregung von UV-Strahlung in Stickstoff und Wasserstoff durch einen  
Elektronenschwarm".  
Zeitschrift für Physik, Vol.173, pp.169-183, 1963
- [98] Teich, T.H.  
Braunlich, R. "UV and other Radiation from Discharges in Artificial Air and its  
Constituents".  
Proceedings of the Eighth International Conference on Gas Discharges and  
Their Applications, Oxford, U.K., pp.441-444, September 16<sup>th</sup> - 20<sup>th</sup>, 1985
- [99] Teich, T.H. "Electrons and Ions in Sulphur Hexafluoride".  
Proceedings of the Second International Swarm Seminar, Oak Ridge,  
Tennessee, U.S.A., July 22<sup>nd</sup> - 23<sup>rd</sup>, 1981  
In: "Electron and Ion Swarms". Editor: L.G. Christophorou, pp.241-250,  
Pergamon Press, New York, U.S.A., 1981
- [100] Enloe, C.L. "Ultraviolet-Induced Flashover of Highly-Angled Polymeric Insulators in  
Vacuum".  
Ph.D. thesis, University of Michigan, U.S.A., 1988
- [101] Wetzer, J.M. "Vacuum Insulator Flashover; Mechanisms, Diagnostics and Design  
Implications".  
IEEE Trans. on Dielectrics and Electrical Insulation, Vol.4, No.4,  
pp.349-357, 1997

- [102] Lepoint, T. "Sonoluminescence: An alternative "electrohydrodynamic" hypothesis".  
Pauw, D. de  
Lepoint-Mullie, F.  
Goldmann, M.  
Goldmann, A.  
Journal of Acoust. Soc. Am., Vol.101, No.4, pp.2012-2029, 1997
- [103] Pedersen, A. "Formulation of the Streamer Breakdown Criterion and Its Application to  
McAllister, I.W. Strongly Electronegative Gases and Gas Mixtures".  
Crichton, G.C. Archiv für Elektrotechnik, Vol.67, pp.395-402, 1984

## List of symbols

$\alpha$ :	Townsend's first ionization coefficient [ $cm^{-1}$ ]
$A$ :	illuminated cathode area [ $cm^2$ ]
$c$ :	velocity of light ( $2.998 \cdot 10^8$ m/s)
$C$ :	capacitance [ $C$ ]
$C_c$ :	coupling capacitance [ $C$ ]
$C_r$ :	capacitance of the test object [ $C$ ]
$C_s$ :	stray capacitance between the measurement electrode and grounded ring [ $C$ ]
$\delta_m$ :	excitation coefficient for excitation to the $m^{\text{th}}$ electronic level
$d$ :	electrode gap spacing, gap width [ $cm$ ]
$D_{z,e}$ :	electron diffusion in axial direction [ $cm^2$ ]
$D_e$ :	electron diffusion tensor
$D_L$ :	longitudinal electron diffusion coefficient [ $cm^2$ ]
$D_T$ :	transverse electron diffusion coefficient [ $cm^2$ ]
$\epsilon_r$ :	dielectric constant ( $8.85 \cdot 10^{-12}$ A s/V m)
$\epsilon_{pe,pi}$ :	electron - positive ion and positive ion - negative ion recombination coefficients [ $cm^3 \cdot s^{-1}$ ]
$e^-$ :	electron
$E$ :	electrical field [ $V/m$ ]
$E_0$ :	electrical Laplacian field [ $V/m$ ]
$E_{min}$ :	minimum electrical field for gas-breakdown [ $V/m$ ]
$E_p$ :	potential energy of the gas molecules or atoms [ $J$ ]
$E_k$ :	kinetic energy of the gas molecules or atoms [ $J$ ]
$E/p$ :	pressure reduced electrical field [ $V/m \cdot Pa$ ]
$f_{max}$ :	maximum frequency bandwidth [ $Hz$ ]
$\Gamma_e$ :	electron flux [ $electrons/cm^2$ ]
$\Gamma_{photon}$ :	photon flux [ $photons/cm^2$ ]
$h$ :	planck constant ( $6.626 \cdot 10^{-34}$ Js)
$h\nu$ :	photon energy [ $eV$ ]
$i$ :	electrical discharge current [ $A$ ]
$J$ :	electrical current density [ $A/cm^2$ ]
$\varphi$ :	phase angle in a cylindrical coordinate system [ $rad$ ]
$\Psi$ :	photoionization coefficient [ $number\ of\ photoionizations\ at\ r' / (number\ of\ ionizing\ collisions\ at\ r) \cdot sr \cdot cm \cdot torr$ ]
$k_{sd,ud}$ :	stable and unstable negative ion electron detachment frequency
$k_c$ :	ion conversion charge exchange frequency
$K$ :	streamer constant in the streamer breakdown criterion
$\lambda$ :	wavelength [ $nm$ ]
$\eta_m$ :	photoionization efficiency for $m^{\text{th}}$ electronic level
$\eta_{s,u}$ :	stable and unstable negative ion electron attachment coefficients [ $cm^{-1}$ ]
$N_{e,p,sn,un}$ :	electron, positive ion, stable negative ion, unstable negative ion densities [ $cm^{-3}$ ]
$N_m$ :	excited species ( $m^{\text{th}}$ electronic level) density [ $cm^{-3}$ ]
$N_{0,min}$ :	minimum critical electron number for gas-breakdown [ $electrons$ ]

$N_{q,net}$ :	total net number of charge carriers
$p$ :	gas pressure [Pa] ( $1.013 \cdot 10^5$ Pa = 760 torr)
$p_q$ :	quenching pressure [Pa]
$q$ :	electronic charge ( $1.609 \cdot 10^{-19}$ C)
$q_{app}$ :	apparent charge [C]
$q_m$ :	measured charge (time integral of the measured current) [C]
$Q$ :	quantum efficiency [number of electrons per number of photons]
$\rho$ :	resistivity [ $\Omega m$ ]
$\rho$ :	charge density [ $C/cm^3$ ]
$\rho$ :	radial coordinate in a cylindrical coordinate system
$r_m$ :	radius of the measuring electrode [cm]
$r$ :	radius of the high voltage electrode [cm]
$r=(z,\rho,\varphi)$ :	position in a cylindrical coordinate system
$r'=(z',\rho',\varphi')$ :	position in a cylindrical coordinate system
$R_d$ :	large damping resistor, so no charge flows through this damping resistor during the prebreakdown phase [ $\Omega$ ]
$R$ :	50 $\Omega$ resistance consisting of four 200 $\Omega$ parallel resistors in (low inductance) star configuration
$R$ :	simulation radius (0.6 cm)
$\sigma$ :	conductivity [S/m]
$S_{ph}$ :	gas phase photoionization process source term
$\tau$ :	RC-time constant [s]
$\tau_m$ :	deexcitation time constant for the excited species [ns]
$t_{bd}$ :	time to breakdown [ns]
$T_c$ :	electron transit time in a uniform field [ns]
$\mu_m$ :	photon absorption coefficient for m <sup>th</sup> electronic level [ $cm^{-1}$ ]
$v_{z(e,p,sn,un)}$ :	electron, positive ion, stable negative ion, unstable negative ion drift velocities in axial direction [m/s]
$v_{ADS,CDS}$ :	anode respectively cathode directed streamer ionization front velocity [m/s]
$v_{ADF,CDF}$ :	anode respectively cathode directed ionization front velocity [m/s]
$V$ :	applied voltage [V]
$\omega$ :	radial frequency [rad/s]
$\omega_m$ :	photon production efficiency for m <sup>th</sup> electronic level
$x$ :	distance [cm]
$X,Y,Z$ :	gas molecules or atoms
$X^+$ :	positive ion
$X^-$ :	negative ion
$\gamma_{photon}$ :	secondary electron yield [number of secondary electrons emitted per number of ionizing collisions]
$z$ :	axial coordinate in a cylindrical coordinate system
$Z_0$ :	characteristic impedance of the coaxial cable and terminating impedance of the oscilloscope [ $\Omega$ ]

## *Acknowledgement*

The work that forms the basis of this dissertation was done at the High Voltage & EMC Group, Power Engineering Division, Department of Electrical Engineering, Eindhoven University of Technology. I especially like to thank my copromotor and coach Jos Wetzer for his enthusiastic support and guidance, my first promotor Piet van der Laan for his support and second promotor Frits de Hoog, and all three of them for their review, comments and discussion. Very important to the work in this project has been Toon Aldenhoven's contribution. He had the knowledge and skills to support and enable the technical realisation of my goals. I like to thank student Ronald Gruntjes and IAESTE student Marietta Vella for their contributions. Furthermore, I like to thank all my colleagues and other people who made working at Eindhoven University of Technology an enjoyable experience.



## *Curriculum Vitae*

Henk Gaxiola was born on May 19<sup>th</sup>, 1969 in Villa Obregón (Mexico).

In June 1988 he graduated from "Het Wagenings Lyceum" (V.W.O. (Athenaeum)), Wageningen. In September 1988 he started studying Electrical Engineering at Eindhoven University of Technology and in August 1994 received his M.Sc.-degree at Eindhoven University of Technology on a "Study of Physical Processes Governing Void Discharges; Time Resolved Measurements and Modelling of Partial Discharges". From November 1994 to March 1999 he worked on a Ph.D. research project in the field of "Insulating Dielectrics and Electrical Discharges" at the High Voltage & EMC Group, Power Engineering Division, Department of Electrical Engineering, Eindhoven University of Technology. During this project he attended several conferences and published many papers on this subject. This research-project has led to this dissertation.

